EUROPEAN ORGANIZATION FOR NUCLEAR RESEARCH (CERN)

ALMA MATER STUDIORUM - UNIVERSITY OF BOLOGNA

FACOLTÀ DI INGEGNERIA
CORSO DI LAUREA MAGISTRALE IN INGEGNERIA ENERGETICA

Multiphysics Modelling of the LHC Individually Powered Quadrupole Superconducting Circuits

Candidate:
Federica MURGIA

Coordinator:
Prof. Ing. Marco BRESCHI
Advisors:
Dr. Emmanuele RAVAIOLI

A.A. 2019/2020
I° Session

Acknowledgement

First of all I would like to thank Prof.Marco Breschi! Without him all this would not have happened. Thanks for this incredible opportunity.

Thanks also to all the STEAM team who have always helped me during my thesis work with suggestions and comments which have increased my knowledge and allowed me to complete the job successfully!
In particular, I would like to thank Emmanule Ravaioli for believing in me. Thank you for your patience, trust, and advice during all these incredible months.

Volevo anche ringraziare le persone che fanno parte della mia vita al di fuori dalla sfera lavorativa. Piccole e grandi famiglie trovate durante il percorso...
Il primo grazie va a colui che ha stoicamente sopportato tutte le crisi isteriche, i viaggi necessari per poter finire di dare gli esami e i continui momenti di smarrimento.
Grazie per aver sempre creduto in quello che stiamo costruendo. Ti amo!
Un grazie gigantesco va alla mia famiglia, che ha sempre appoggiato tutte le mie scelte sostenendomi in ogni momento.
Grazie per essere tutti così meravigliosi...
Grazie alla mia famiglia bolognese che mi ha ospitato, nutrito e soprattutto sopportato facendomi sentire sempre a casa.
Ed infine grazie alla mia famiglia adottiva che vive al di là delle Alpi per questi anni di compagnia indimenticabile e agli amici di sempre che vivono sull'isola ma che sono sempre presenti.

Contents

List of Figures

List of Tables

1 Introduction

The Large Hadron Collider (LHC) is a particle accelerator built by the European Organization for Nuclear Research (CERN) between 1998 and 2008. It contains 1572 superconducting circuits, distributed along eighth sectors of the LHC. The scope of this thesis is to develop, validate, and characterized the models of the individually powered quadrupole (IPQ) circuits of the LHC.

The study of the complex behaviour of the magnet was modeled using STEAM [1] (Simulation of Transient Effects in Accelerator Magnets) framework, which was developed in the Performance Evaluation (TE-MPE-PE) section at CERN.

1.1 Conseil Européen pour la Recherche Nucléaire

Established in 1954, located in Geneva, Switzerland, nowadays it is the largest particle physics laboratory ever built. It counts 23 members and co-operations with almost every state in the world. Birthplace of the World Wide Web, it has accomplished many scientific achievements, last of them the discovery of the Higgs boson (Nobel prize in 2013) and the penta-quarks (2015). CERN is not only one of the most important research center of the world, but it also represents the joint of different cultures and languages, the hard work and the passion over the differences. A virtuous and peaceful example of international collaboration with an unique aim: Science [2].
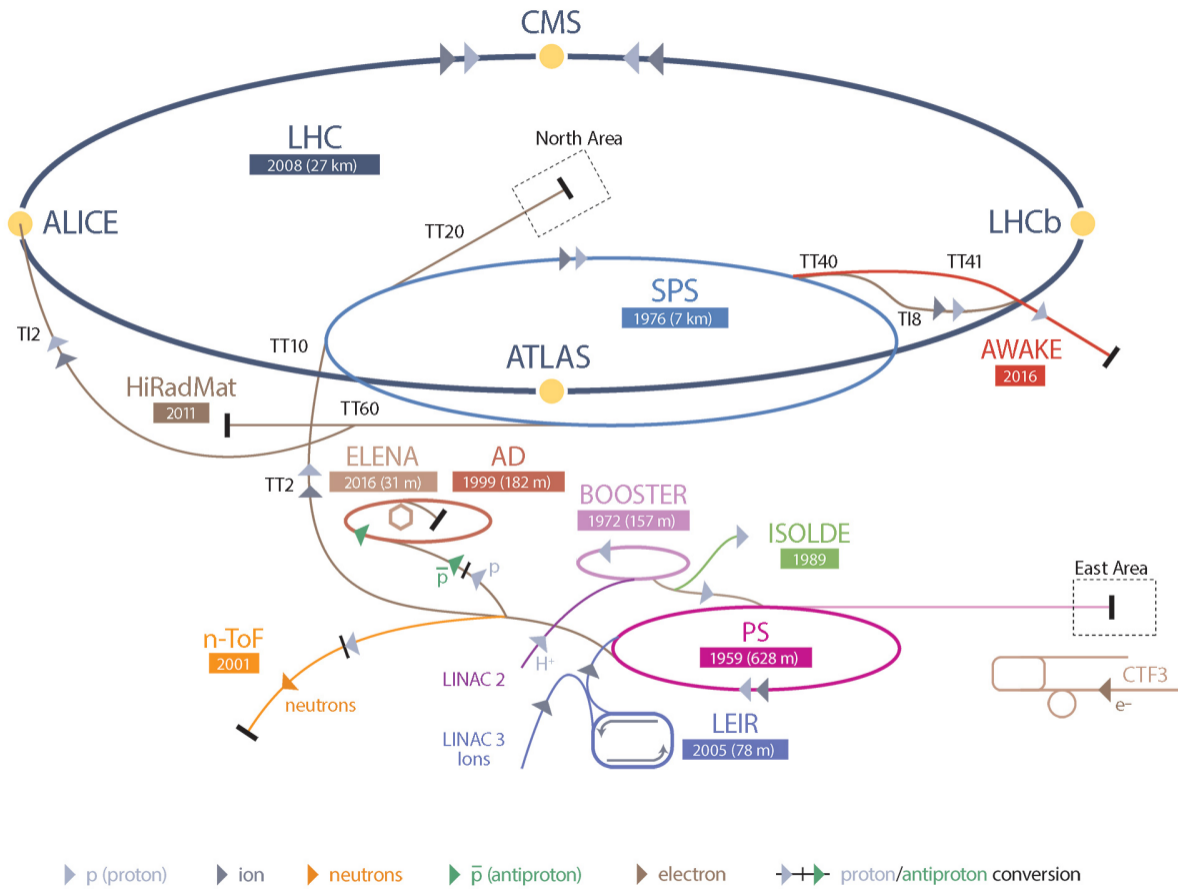
FIGURE 1.1: CERN accelerator complex.

1.2 Large Hadron Collider-LHC

The Large Hadron Collider (LHC) is the largest particle accelerator ever built. It first started up on 10 September 2008, and remains the latest addition to CERN's accelerator complex.

The LHC is a ring tunnel 27 km long, where superconducting and resistive magnet circuits are located in accelerating structures to boost the energy of the particles along the way. The entire complex system of accelerators is shown in Fig. 1.1. To understand the challenges of accelerating particle beams in circular accelerators, it is possible to follow the process of acceleration from the source to the high energy.

Hydrogen atoms are taken from a bottle containing hydrogen gas whose electrons are stripped out. The protons are then accelerated in the Linac2 to the kinetic energy of 50 MeV. The beam is extracted from Linac2 and injected in the PS (Proton Synchrotron) Booster, a piled-ring accelerator built-in 1972, to accelerate the beam up to 1.4 GeV. Particles are then injected in the SPS (Super Protron Synchrotron) where a further acceleration bring them to 450 GeV. The beam is then transferred in the two beam pipes of the LHC through the transfer lines TI2 (clockwise) or TI8

(anti-clockwise). The particles travel inside the pipes, in opposite directions, with a velocity equal to the 99.999991% of the speed of the light. The energies are so high that the collision between the two beams can attempt to reproduce the conditions during the first instants of the universe after the Big Bang.

Through the complex system of accelerator, the particle beams can reach the maximum energy of 6.5 TeV per beam. The two beams are brought into collision inside four detectors ALICE, ATLAS, CMS and LHCb, where the total energy at the collision point is equal to 13 TeV [3].

To drive the beams inside the LHC tunnel, three main elements are required:

- Radio Frequency (RF) cavities. They increase the particle energy at every turn, based on an alternating electrical potential which acts on the particles as an accelerating field.
- Dipole Magnets (MB). They generate the magnetic field able to bend the particle beams, maintaining them in the reference trajectory.
- Quadrupole Magnets (MQ). They focus the particles into the reference orbit, preventing them from diverging from the center of the beam pipe.

To modify the velocity and the trajectory of the particles, the electric and the magnetic fields have to be used. The Lorentz force equation combines both. The deflection force is given by the equation 1.1, where **F** is the force acting on a particle, *q* is the charge of the particle, **E** is the electric field, **v** is the velocity of the particle, and **B** is the magnetic field.

$$\mathbf{F} = q(\mathbf{E} + \mathbf{v} \cdot \mathbf{B}) \tag{1.1}$$

The dipole on the LHC are electromagnets, and they use a current of 11080 A to produce the field to provide the magnetic fields necessary to the bending and the confinement of the beam. About 6000 superconducting magnets are installed on the LHC tunnel, and over 95 tonnes of liquid Helium are needed to maintain the system at the operating temperature of 1.9 K (-273.15 °C). The superconducting coil allows the high currents to flow without losing any energy to electrical resistance.

1.3   Brief history of superconductivity

On the 10th of July 1908, Heike Kamerlingh Onnes, professor at the Leiden University, produced for the first time liquefied helium, reaching the temperature of 4.2 K (-269°C). After three years he noted: *"Kwik nageon nul" (Quick [silver] near-enough null)*. Analyzing the behaviour of the electrical resistance at the cryogenic temperature, he noted that:*"Mercury has passed into a new state, which on account of its extraordinary electrical proprieties, may be called the superconducting state"* [4] characterized by a not measurable value of electrical resistance, as shown in Fig. 1.2. This transition occurs under a critical temperature Tc, different for each material.
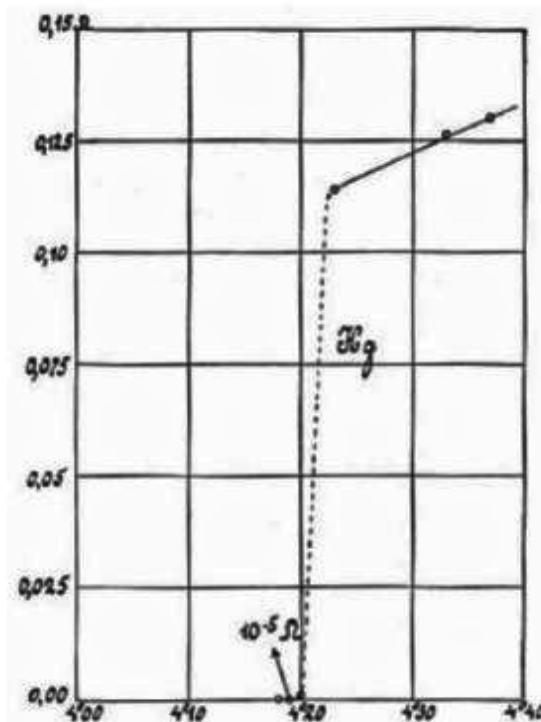
FIGURE 1.2: Historic plot of resistance versus temperature of the mercury material. From the 1922 Onnes experiment, shows the superconducting transition at 4.20 K [7].

The next milestone occurred in 1933 when Meissner and Ochsenfeld discovered that a material in superconducting state expels the magnetic field, becoming a perfect diamagnetic material [5]. The first phenomenological theory of superconductivity able to explain the Meissner effect was developed by the London brothers in 1935, through the formulation of the well-known London's equations [6].

A quantum explanation was proposed in 1957 by Bardeen, Cooper, and Schrieffer: the so-called BCS theory [8]. In 1962, the first commercial superconducting wire, a niobium-titanium alloy, was developed by researchers at Westinghouse, allowing the construction of the first practical superconducting magnet. In 1986 the superconductivity in a lanthanum-based cuprate perovskite material was discovered, with a transition temperature of 35 K [9]. Just a year later, replacing the lanthanum with yttrium (*YBCO*), the critical temperature of 92 K was reached [10]. In 2001 these particular properties have been discovered in magnesium diboride (*MgB$_2$*), that has a critical temperature of 40 K [11].

1.4 Superconducting properties

Superconductivity is a remarkable phenomenon whereby certain materials, cooled at very low temperatures, become excellent conductors of electricity. The superconducting state appears quite abruptly at the critical temperature Tc [K], which is a characteristic parameter of the specific material. Below this temperature the resistance is not just very small, it is absolutely equal to zero. The vanishing resistance is not enough to define a material as a superconductor because every conductor, at a temperature close to the absolute zero, tends towards a null value of resistance. Superconductors exhibit a perfect diamagnetism below the critical temperature Tc, ejecting external applied magnetic field by means of superficial super-currents, until the limit value of the critical magnetic field Bc [T]. This phenomenon is called Meissner-Ochsenfeld effect and it is shown in Fig. 1.3.

The classical model of superconductivity, developed by the London brothers in 1935, can explain these two basic characteristics of the superconductors through the following equations:

$$\mathbf{E} = \mu_0 \lambda^2 \frac{\partial \mathbf{J}}{\partial t} \quad \rightarrow \quad \text{null resistivity}$$
$$\mu_0 \lambda^2 \nabla \times \mathbf{J} = -\mathbf{B} \quad \rightarrow \quad \text{Meissner-Ochsenfeld effect}$$

$$(1.2)$$

Where $\mathbf{J}$ is the current density, $\mathbf{B}$ and $\mathbf{E}$ are respectively the magnetic and electric fields. While μ_0 is the vacuum permeability, and λ is know as London penetration depth and it estimated around 10^{-7} m But this model does not take into account the quantum phenomena and the existence of the fluxons.

Critical temperature, magnetic field, and current are three not intrinsic characteristics of the material. They depend on the thermal and mechanical treatment induced in the superconducting cable. These three properties are related to each other by the critical surface in *T,B,J* space (see Fig. 1.4). This surface is characteristic of each
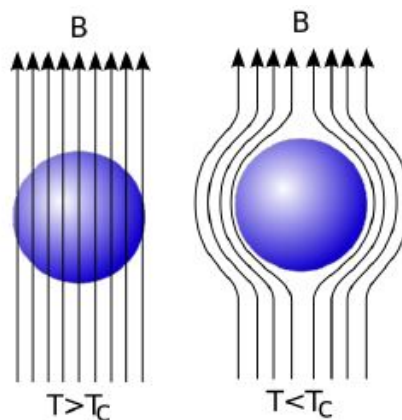
FIGURE 1.3: Diagram of the Meissner-Ochsenfeld effect. Magnetic field lines, represented as arrows, are excluded from a superconductor when it is below its critical temperature [12].
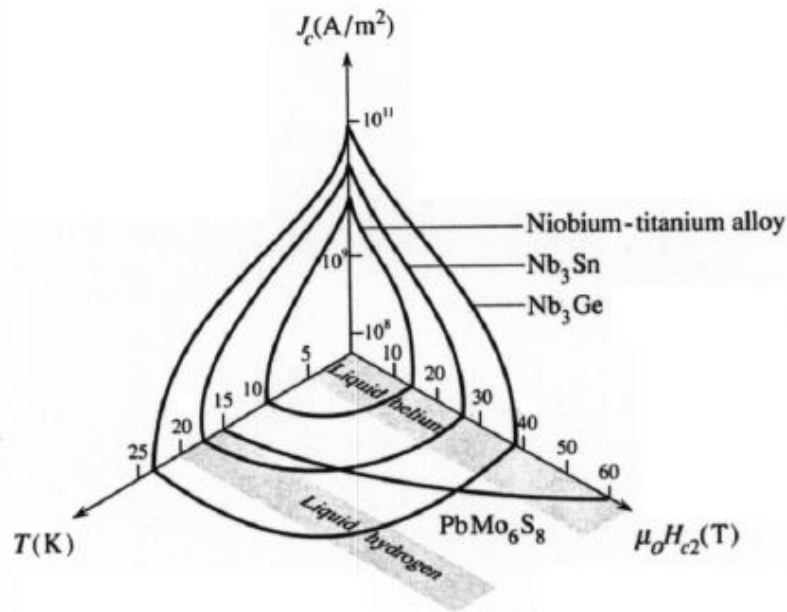
FIGURE 1.4: Critical surface of Nb-Ti, Nb$_3$Sn and Nb$_3$Ge in the T,B,J space [13].

superconducting material. Superconductivity prevails everywhere below this surface.

Superconductors are classified into two categories: type-I and type-II. Type-I superconductors exhibit the properties explained above, while type-II superconductors are typically alloys and compounds, and they present a gradual transition to the normal state across a region of *mixed state* behaviour. Type-I and type-II superconductor are shown in Fig. 1.5. Over the lower critical magnetic field H_{c1}, magnetic vortexes penetrate inside the material, inducing a local transition to the normal state. The quantum mechanics imposes that each vortex carries a quantum of magnetic flux, called fluxon. The vortex density increases with increasing field strength until the upper critical magnetic field H_{c2}, where the complete transition to the normal state occurs.

The critical magnetic field of the type-I superconductors has an extremely low value, hence this kind of material does not have any practical applications, while the critical field H_{c2} (type-II superconductors) can reach interesting values. Concerning technical operations, superconductors always work in the mixed state, in absence of perfect diamagnetism, characterized by the existence of quantized magnetic flux vortex inside the material. The presence and relative motion of these vortexes, by means of the Lorentz's forces, induce dissipation and losses.

A different kind of superconductor classification can be done, based on this intrinsic feature:Low Temperature Superconductors (LTS) (metallic materials with a critical temperature value below 30-40 K) whose properties can be explained through the BCS theory [8], and High Temperature Superconductors (HTS), materials with a critical temperature value below 90-100 K. The HTS opens the doors to new applications of superconductivity, restricted until that moment by very low temperature and cooling.
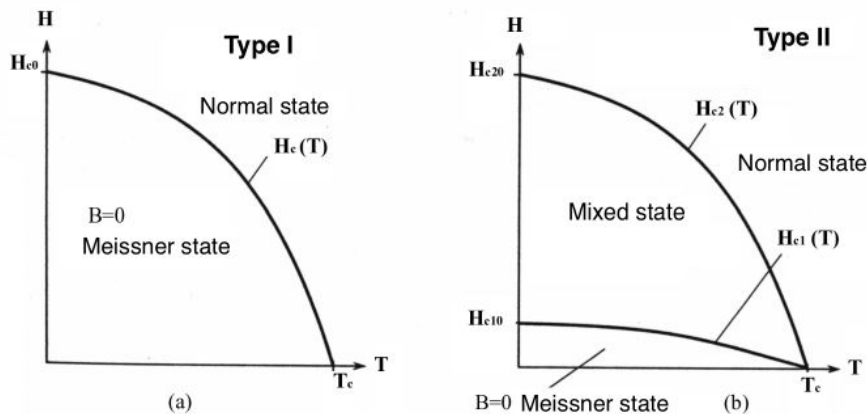
FIGURE 1.5: Comparison between the H-T diagram of type-I (a) and type-II (b) superconductor [14].

HTS superconductors like $Bi_2Sr_2CaCu_2O_8$ (first generation) and $YBa_2Cu_3O_7$ (second generation) are characterized by complex manufacturing and substantial costs.
The analyses carried out in this thesis are focused on Nb-Ti material. It is a type-II LTS superconductor operating at the temperature of super-fluid liquid Helium of 1.9 K or the temperature of liquid Helium of 4.5 K. On this demanding condition, every heat perturbation and unwanted temperature oscillation can change the stability of the system. Unexpected transition to the normal state occurs several times in the life of a magnet. It is essential to understand how heat perturbations can affect the superconducting coils and especially how they react in terms of temperature and currents.

1.5   Superconducting magnets

All the superconducting magnets used in the LHC, are Nb-Ti magnets operating a temperature between 1.9 K and 4.5 K. For the High Luminosity LHC upgrade it is planned to install new Nb-Ti and Nb_3Sn magnets in the machine.

The main motivation to use superconductive technology is due to the vanishing electrical resistance and capacity to generate a high magnetic field. The maximum magnet field reachable at 4.2 K and high current is around 9 T for Nb-Ti and 18 T for the Nb_3Sn, avoiding to increase the system dimension [15].

When the superconducting material changes the state from the superconductive state to the normal one, it grows the electrical resistivity about three orders of magnitude, as the electrical conductors at room temperature. For this reason, the superconductor is normally embedded in a matrix of low-resistivity material. The stabilizer, usually copper, that embeds the thin filaments (few micrometers in diameters), has to be provided to reduce the ohmic loss per unit length of conductor [16]. The cross-sections of two wires of different materials, are shown in Fig. 1.6.

Some LHC magnets are composed using Rutherford cables, shown in Fig. 1.7. Each superconducting filament in a copper matrix can carry a current of about 25 mA to 50 mA, then each wire can transport 250 A to 500 A. As a consequence, it is necessary to use 20 to 40 wires connected in parallel in a superconducting cable to reach the nominal current of a superconductor magnet [16].

During the operation, the superconducting magnets are subject to a magnetic-field transitory that introduce losses. The two main losses taken into account during this thesis are the Inter-Filament Coupling Loss (IFCL) and the Inter-Strand Coupling Loss. The IFCL are generated in the wired matrix between the superconducting filaments of a strand. To reduce the coupling losses the superconducting filaments are twisted [19]. The ISCL are generated at the contact points between superconducting
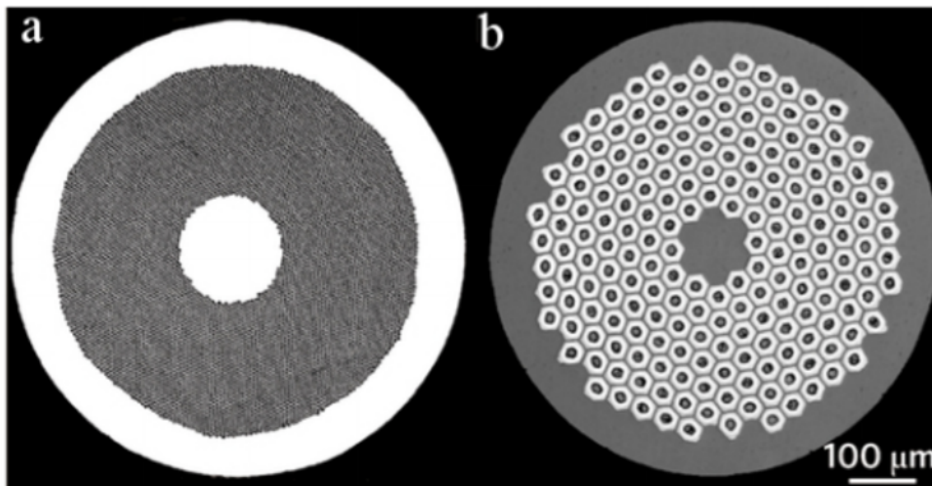
FIGURE 1.6: Wires with superconducting filaments.(a) Wire made of Nb-Ti filaments embedded in a copper matrix. (b) Wire made of Nb_3Sn filaments [17].

strands of a cable due to coupling currents between strands [15]. As for the IFCL, also the cables are twisted in order to reduce the coupling losses. Other types of losses are the mechanical loss, the eddy current loss, and the ferromagnetic loss.

1.5.1 Quench

The therm *quench* is used to describe the irreversible transition of the material from a superconducting state to the normal state. A quench occurs when the local condition in terms of temperature, magnetic field, or current density does not allow to continue the superconducting state [16].

When a superconducting magnet quenches, the normal conductive zone propagates and this causes the dissipation of the stored energy in the magnet increasing the resistance that forces the magnet current to decay. The normal conductive zone has to grow fast to minimize peak temperature and peak voltage. In most accelerator magnets natural resistance growth is insufficient to avoid excessive temperature and voltage to ground, so is it necessary to include a protection system. Control and prevention of the transition from superconducting state to the normal state is one of the most important problem concerning this technology. The superconducting magnet is always subject to a series of energy inputs of very different natures, time-scales, and magnitudes, the so-called disturbance spectrum. The disturbance spectrum of the energy perturbations is shown in Fig. 1.8 [20].

At cryogenic temperatures almost all the materials have a small heat capacity, and the difference between the operating temperature *Top* and the temperature at which current sharing starts *Tcs* must be kept small. Therefore even a small energy perturbation is sufficient to take the superconducting material above the critical conditions, inducing a normal zone propagation and Joule heating generation. The energy perturbations can be generated by phenomena such as mechanical events, flux jump, eddy losses,and heat leaks [16].
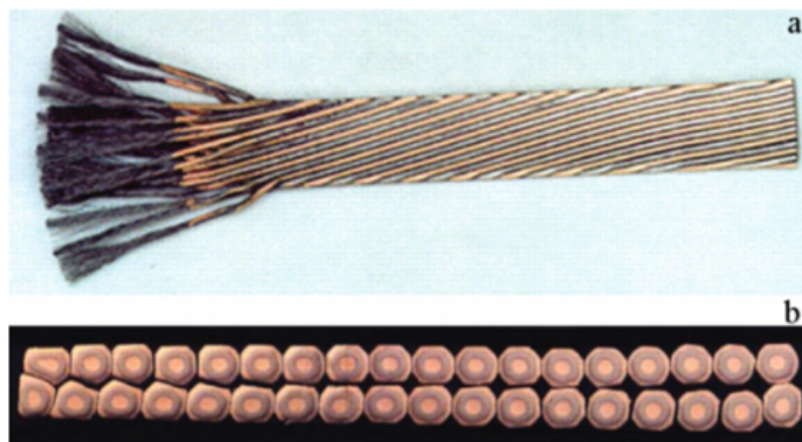
FIGURE 1.7: Example of a Nb-Ti Rutherford cable used in the LHC main dipole magnets [18]. (a) View from the top. (b) View at the cross-section.

If not prevented, the temperature in the quench zone increases and the normal front propagates, inducing an irreversible thermal runaway process that lead the loss of superconductivity in part of the magnet. The diagram shown in Fig. 1.9, summarizes the main effects of a quench. The consequences of a quench are to be carefully considered during the magnet design.
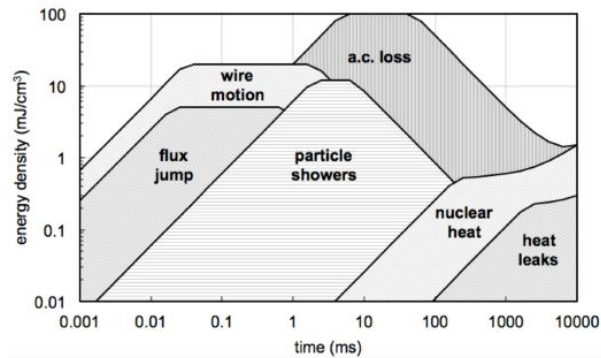
FIGURE 1.8: Spectrum of energy perturbations as a function of the characteristic time of energy deposition [20].
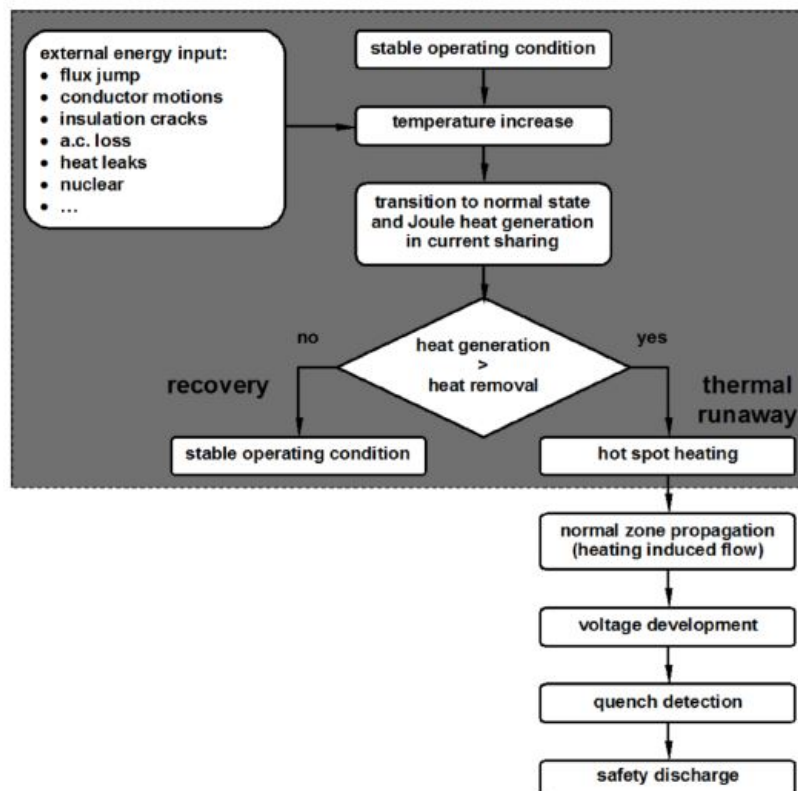
FIGURE 1.9: An event tree following an external energy input, and leading from stable operating conditions back to stable operation or to a magnet quench. The stability design and analysis are concentrated on the shaded area in the event tree [20].

1.6 Magnet protection

Superconducting magnets operate at high magnetic field and can store high magnetic energy, thus the damage potential by overheating is significant. It is possible to avoid the damage, by-passing the quenched magnet thanks to the by-pass elements. In the LHC machine these by-pass elements are silicon diodes situated inside the cryostat, called cold diodes.

The high energy stored in the superconducting magnets makes necessary to detect the quench very quickly, to switch off the power source in the circuit, extract part of the magnet stored energy, and/or spread the quench quickly through a large volume of the magnet.

To detect the quench in a magnet, there are many different methods mainly based on current and voltage measurements. The most used in the LHC circuits is based on the comparison between the voltages across the two halves of the magnet [21].

There are many techniques developed to protect the magnets, some of them are passive and the others are active. The passive protection is the simplest and least expensive magnet protection method, but usually, it is insufficient to protect magnet with high stored energy. Once the quench appears in the magnet, the passive protection starts to protect it thanks to the transition from the superconducting state to the normal conducting state. When the transition to the normal state occurs, the local ohmic heat generated in the normal zone propagates to the other sections of the coil. The electrical resistance developed in the normal zone can cause the discharge of the magnet transport current before that the temperature exceeds safe limits. While the active protections systems require an external trigger to be activated, such as an electronic signal generated after the detection of a quench. After the quench detection, a switch-off of the power source is needed and the discharge of the energy is forced. The total time required to activate the protection system can be summarized as the sum of the times required to detect a quench, validate the detection, and trigger the protection system, as shown in Fig. 1.10.

During this thesis work three active protection systems are taken into account. They will be described in the following sections.

1.6.1 Quench heaters

The Quench Heaters (QH), shown in Fig. 1.11, are the most common active protection system on the LHC superconducting magnets. They consist in one or two 0.025 mm-tick resistive strips, usually in stainless steel, bonded between two layers of electrical insulation foil, and attached to the insulation layer of the coil to protect [22]. The terminals of each quench-heater strip are connected to a capacitor bank. Upon quench detection, the energy stored in the capacitor bank is discharged in the strips, which transfer the energy to the coil through thermal diffusion across the thin insulation layer. To protect the magnet, it is sufficient to heat up only some sections (heating stations) of the coils, for this reason, the strips are partially plated

with copper. Once the superconductor in correspondence to the heating stations is transferred to the normal state, the local ohmic loss causes heat propagation and thus the propagation of the normal zone in the direction of the transport current up to the next heating station.
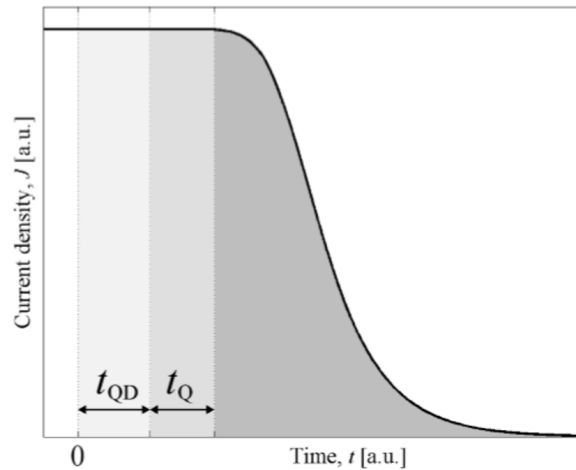
FIGURE 1.10: Coil protection phases. The quench starts in t=0. The quench is detected, validated and the protection system is triggered in the time window t_{QD}. The entire coil is transferred to the normal state by the protection system during the time t=t_{QD}+t_Q [15].

FIGURE 1.11: Quench Heaters strips of the 11T dipole [23].

The two main limitations of this protection are the delicate electrical design and the difficulty to transfer the entire winding pack to the normal state in a sufficiently short time; for coils based on Nb-Ti the values of this time margin are in the range of 50-200 ms [24]; if the quench heater strips do not touch all coil turns, the normal zones have to propagate to the adjacent turns through thermal diffusion across insulation layers, with a typical delay of about 10 ms per turn [24].

1.6.2 CLIQ

The CLIQ (Coupling-Loss Induced Quench) [15, 25] is an active protection system based on the generation of high coupling loss. The electrical scheme of a protection system based on the CLIQ method is shown in Fig. 1.12 [15].
The CLIQ unit is connected to the magnet by two additional resistive current leads C_{L1} and C_{L2}. Once the CLIQ protection system is activated, upon quench detection via the thyristor, an oscillating current is introduced into the coils by the capacitor bank C. Part of this current flows through the coil section L_A and L_B, respectively, but in opposite directions. The presence of the reverse diode allows continuous oscillations, thus maintaining a variable magnetic field in the superconductor coils. The variable magnetic field introduces transitory loss that permits a heat generation in the superconductor in the first tens of milliseconds after the CLIQ triggers.
This protection method is faster than conventional quench heaters. A CLIQ protection system can turn to the normal state the entire winding pack of a full-scale high magnetic field magnet in 10 to 40 ms [15]. The other advantages of the CLIQ protection are due to the easy and robust electrical design and the position of the terminals, that are usually situated at the coil ends where is relatively easy to access.

1.6.3 Energy-extraction

The last active protection analyzed is the energy-extraction (EE) system. The energy extraction is a conventional system used to reduce quickly the current in the magnet. During this thesis, the EE will be always coupled with another protection system (QH or CLIQ). The electrical circuit of this protection system is visible in Fig. 1.13. It is composed of a resistor, R_{EE} [Ω], where the magnet current is diverted once a quench is detected in the magnet. Usually, the resistance R_{EE} is assumed larger than the resistance of the normal conducting zone of the magnet coil. During the discharge, the coil self-inductance and the energy-extraction resistance can be considered constant, for this reason, it is possible to assume that the magnet transport current decays exponentially.
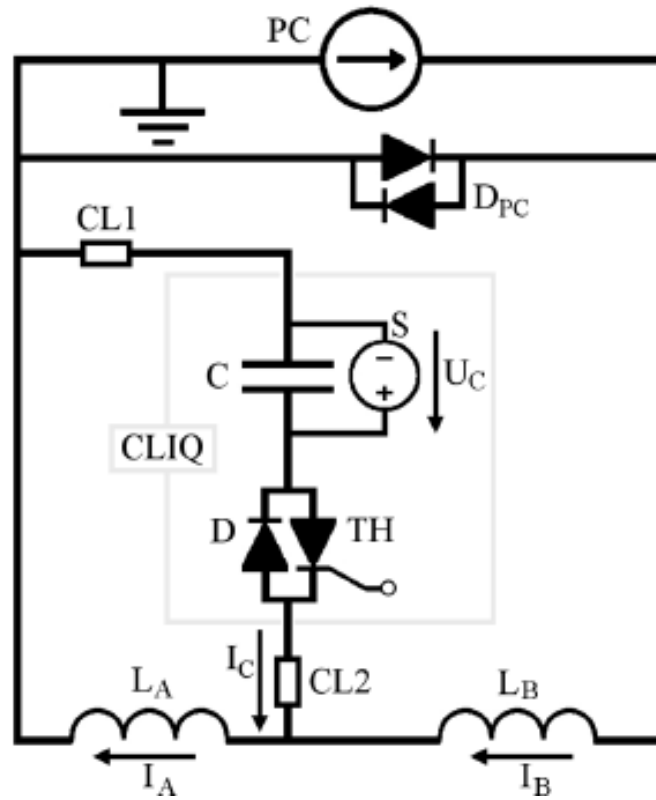
FIGURE 1.12: Electrical scheme of a CLIQ unit connection [15].
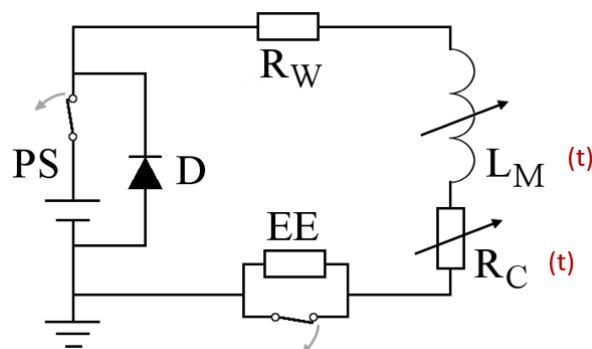
FIGURE 1.13: Simplified magnet circuit with schematic parameter of the
energy-extraction protection system [15].

2 LHC superconducting matching section circuits

A total of 1612 electrical circuits are distributed along the eight sectors of the LHC.
In the LHC there are 131 different types of circuits connecting main bending magnets, magnets for beam focusing, dipole field correctors, or higher-order correctors [26].
The two particle beams that rotate in different directions in the LHC require opposite magnetic fields in both apertures. The LHC contains 1232 superconducting main dipole magnets (MB) and 392 superconducting main quadrupole magnets (MQ), including 86 MQM (matching) and 26 MQY (wide aperture) [27]. All these magnets contain two apertures, each connected with an electrical circuit, or in separate electrical circuits, depending on the use of the circuit [26].
The layout of the LHC (shown in Fig. 2.1) is divided in eight main insertions (IR):

- High luminosity insertion, IR1 and IR5.
- Medium luminosity insertion, IR2 and IR8
- Beam cleaning insertion, IR3 and IR7
- Radio Frequency insertion, IR4
- Beam abort insertion, IR6

High and medium luminosity insertions regions are dedicated to experiments (CMS, ATLAS, ALICE, LHC-B), the others are used for major collider systems.
The magnets used in the eight insertions are super- or normal- conducting. All the superconducting magnets of the LHC, are based on the Nb-Ti technology, cooled by superfluid helium.
In this thesis the superconducting magnets dedicated to the matching section of the LHC will be analyzed.
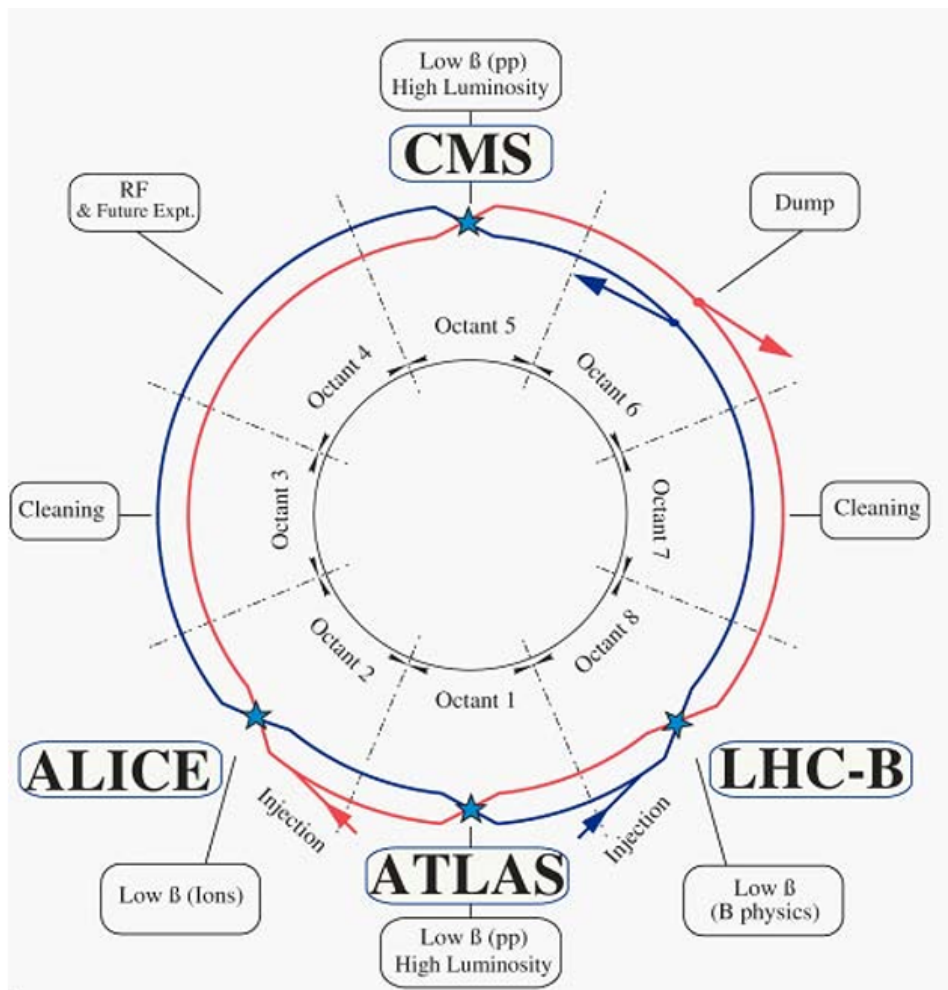
FIGURE 2.1: Schematic layout of the LHC. [28]

2.1 Superconduting magnets in the matching individually-powered quadrupole circuits

The LHC insertions require 50 specific superconducting quadrupoles in the matching sections, operating either in 1.9 K superfluid helium or in liquid helium at 4.5 K [29]. The number of magnets used in the matching sections are different in each insertion, for example in the high luminosity insertion (IR1 and IR5) the MS and the DS consist of twin-bore magnets with separate beam pipes for each ring. In insertion IR5 there are four matching quadrupole magnets. The first quadrupole magnets are operated at a cryogenic temperature of 4.5 K and a nominal gradient of 160 T/m. The last three quadrupole magnets are operated at 1.9 K with a nominal gradient of 200 T/m [26].
In the matching section a non-symmetric magnet layout is required to compensate the shift of the collision point before the beam returns to the DS sections.
The LHC matching sections are built with individually powered superconducting Nb-Ti quadrupole magnets of the types MQM and MQY cooled at 1.9 K and 4.5 K. No additional correctors are required when these types of magnets are used, but the
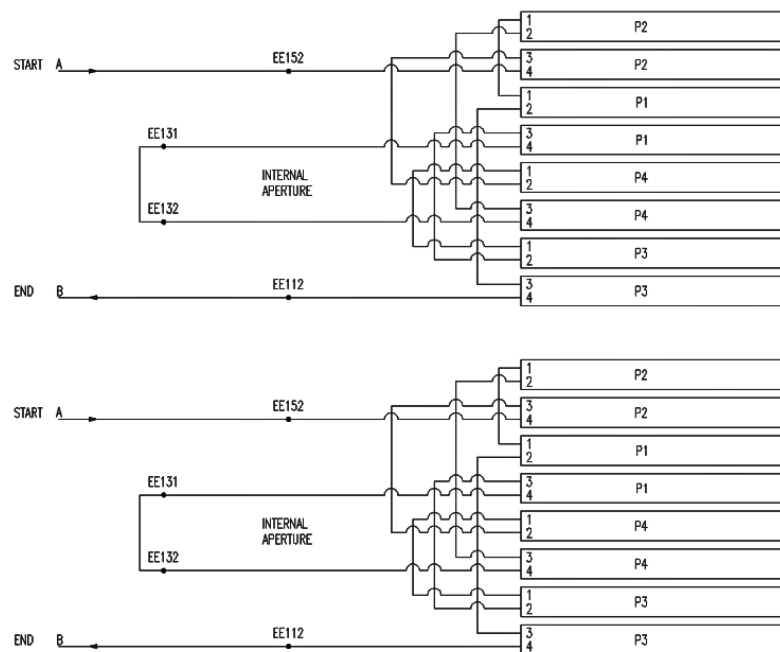
FIGURE 2.2: Electrical scheme of the two individually powered apertures of the MQY magnet [30].

number of magnets and their parameters are specific for each insertion.

MQY Magnet

In the LHC matching section, 24 MQY magnets are required. The MQY quadrupole magnet consist in two individually powered apertures (as show in Fig. 2.2), assembled in a yoke structure shown in Fig. 2.3 [26]. The coil aperture of the magnet is 70 mm and its magnetic length is 3.4 m. The main magnet and conductor parameter are summarized in Tab. 2.1. Each MQY coil is composed of four layers. The first and part of the second layer are wound using the inner conductor. The transition between the cables is made in an internal joint in the middle of the second layer. The winding of the third and fourth layers is completed with the outer conductor. The connections between the layers, as well as between the poles, are made in a connection box mounted on the endplate of the collared aperture.

The MQY coils are assembled in a collared aperture. The collar is 22 mm thick and need to be locked with eight full-length tapered keys to minimizing deformation. In this configuration the collars provide the necessary compressive stress to withstand the magnetic force.

In the MQY magnet, two different types of Rutherford Nb-Ti superconducting cables are used for winding the coils. They are both 8.3 mm wide but are made of two different types of strands. The strand diameters of the two cables are 0.735 mm and 0.475 mm, and the Cu/SC ratios are 1.25 and 1.75. Strand and cable parameters were chosen to have a similar margin to quench in both cable at the same current, so the
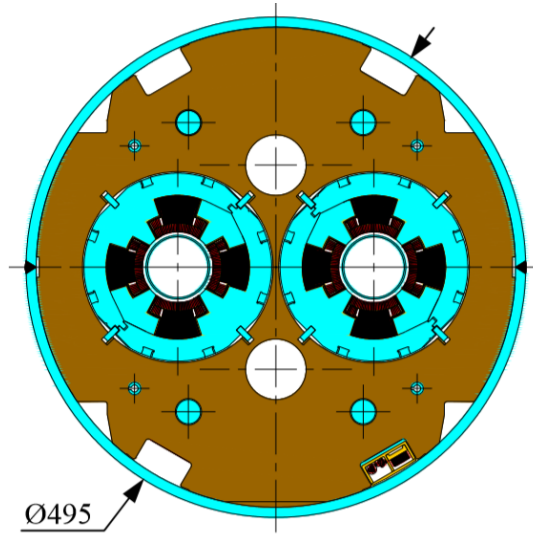
FIGURE 2.3: Cross-section of the MQY quadrupole [28].

TABLE 2.1: Main parameters of the MQY quadrupole magnet and conductors (Inner and Outer) [26].

Magnetic length	3.4 m
Operating temperature	4.5 K
Nominal gradient	160 T/m
Nominal current	3610 A
Coil inner diameter	70 mm
Cold bore diameter O/I	66.5/62.9 mm
Peak field in coil	6.1 T
Quench field	7.5 T
Stored energy at nominal current	479 kJ
Inductance at nominal current	73.8 mH
Cable width, cable I/O	8.3/8.3 mm
Mid-thickness, cable I/O	1.285/0.845 mm
Keystone angle, cable I/O	2.16/1.05 mm
Number of strands, cable I/O	22/34
Strand diameter, cable I/O	0.735/0.475 mm
Cu/SC ratio, cable I/O	1.25/1.75
Filament diameter, cable I/O	6/6 μm
Filament twist peach, cable I/O	15/15 mm
Strand twist peach, cable I/O	66/66 mm
RRR, cable I/O	150/150
Insulation thickness, cable I/O	79.8/79.8 μm
Jc, cable 1/2, (4.2 K and 5 T)	2670/2800 A/mm^2
Mass	4400 kg

current density in one cable is 1.5 times higher than the one in the other cable, at the same current. As in the MQM magnet, the Rutherford cables are insulated using three layers of polyimide film.
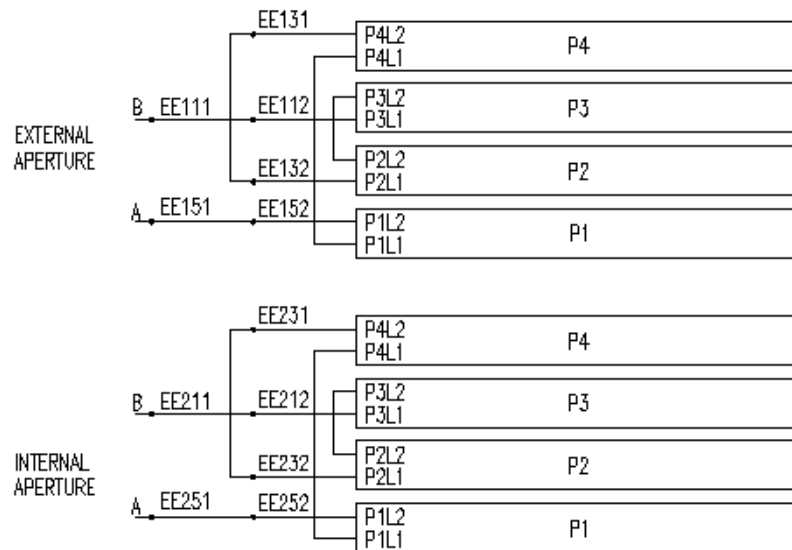
FIGURE 2.4: Electrical scheme of the two individually powered apertures
of the MQM magnet [30].

The protection of the MQY magnets in assured by sixteen quench heaters strips of two different widths. Half of the strips are located on the outer surface of the fourth layer. The others eighth strips are located between the second and the third layers. This high number of heaters is required to limit the voltage during quench in case of failure of some of the heaters. For redundancy, inner and outer heaters are connected in two circuits powered by independent power supplies.

MQM Magnet

A total of 84 MQM magnets are required in the dispersion suppressor and matching sections. They are produced in three different versions, with different magnetic length: 2.4 m, 3.4 m, and 4.8 m [28].
The two apertures of the MQM magnet, individually powered (as shown in the electrical scheme in Fig. 2.4), are assembled in a two-in-one yoke structure, as it is shown in Fig. 2.5. The main magnet and conductor parameters of the MQM magnet are summarized in Tab. 2.2. The coils of the MQM magnet are composed of two layers assembled into a collared aperture. The collars are locked with four keys that provide the necessary compressive stress to withstand the magnetic forces generating during the operation. The collared apertures are assembled in the iron yoke. The yokes of the magnets are compressed and locked with elastic pins to center the apertures. The longitudinal rigidity of the magnet is provided by four tie-rods.
The superconducting cables used for the MQM quadrupole are Nb-Ti Rutherford cables. The diameter of the filament is 6 μm, and it was chosen in order to minimize the effect of the persistent currents at low fields. Each Rutherford cable is composed of 36 strands with a strand diameter of 0.475 mm, and they are insulated with three
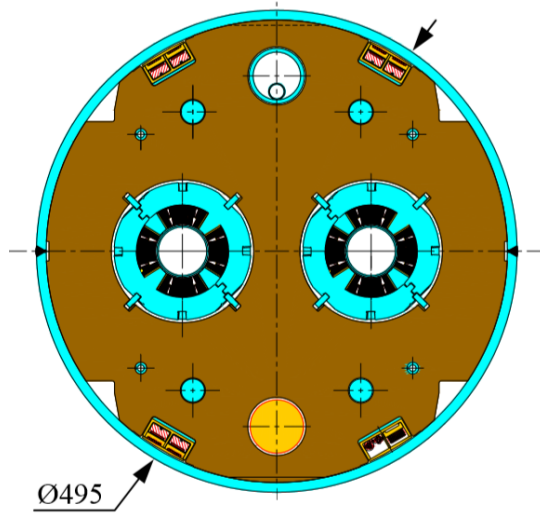
FIGURE 2.5: Cross-section of the MQM quadrupole [28].

TABLE 2.2: Main parameters of the MQM quadrupole magnets and conductors [26].

Magnetic length	2.4/3.4/4.8 m
Operating temperature	1.9/4.5 K
Nominal gradient	200/160 T/m
Nominal current	5390/4310 A
Coil inner diameter	56 mm
Cold bore diameter OD/ID	53/50 mm
Peak field in coil	6.3 T
Quench field	7.8 T
Stored energy at nominal current	64.3 kJ/m
Inductance per aperture	4.44 mH
Cable width	8.8 mm
Mid-thickness	0.84 mm
Keystone angle	0.91 deg
Number of strands	36
Strand diameter	0.475 mm
Cu/SC ratio	1.75
Filament diameter	6 μm
Filament twist peach	15 mm
Jc (4.2 K and 5 T)	2800 A/mm^2
Mass	3100/4300/6000 kg

layers of polyimide film. The first two layers are wrapped with the polyimide film 11 mm wide and 25 μm thick, with a second layer offset by half the tape width. The third insulation layer is a 9 mm wide and 50 μm thick polyimide film, with a 5 μm thick coating of adhesive which cures at 185 °C, wrapped with a 2 mm gap.

The protection system of the MQM magnets is assured by the quench heaters. The eight strips are located on the outer layer of each coil. For redundancy, the heaters are

TABLE 2.3: Overview of the IPQ circuits in the LHC machine.

Circuit	Location	PC	Magnets	Temperature [K]	Nominal current [A]
RQ4	IR 2,8	RPHH	2xMQY	4.5	3610
RQ5	IR 2,8	RPHH	2xMQY	4.5	3610
RQ6	IR 2,8	RPHGB	MQM+MQML	4.5	4310
RQ7	IR 1,2,5,8	RPHGA	2xMQM	1.9	5390
RQ9	IR 1,2,4,5,6,8	RPHGA	MQM+MQMC	1.9	5390
RQ4	IR 1,5,6	RPHH	MQY	4.5	3610
RQ5	IR 4,6	RPHH	MQY	4.5	3610
RQ6	IR 4	RPHGB	MQY	4.5	3610
RQ5	IR 1,5	RPHGB	MQML	4.5	4310
RQ6	IR 1,5	RPHGB	MQML	4.5	4310
RQ7	IR 4	RPHGA	MQM	1.9	5390
RQ8	IR 1,2,4,5,6,8	RPHGA	MQML	1.9	5390
RQ10	IR 1,2,4,5,6,8	RPHGA	MQML	1.9	5390

connected in two circuits, such that each circuit covers all four poles and is powered by independent power supplies.

The cold masses containing the MQM and MQY magnets are assembled in a helium vessel at CERN, in the Magnet Assembly Facility. The central elements of the assembly are two 10 mm thick half-shells made of AISI 304L steel which serve for alignment of the various magnetic elements, provide the rigidity, and serve as a helium pressure vessel. The vessel is closed with two end covers, which also support the required elements for interconnecting the string of LHC cryo-magnets. Several electrical circuits and their instrumentation are installed during assembly.

2.2 Superconduting electrical circuit in the matching section

The magnets of the LHC are powered in about 1700 different electrical circuits [31]. A total of 78 Individually Powered Quadrupole (IPQ) circuits are present in the LHC. The IPQ circuits are composed of different Power Converters (PC), different type and combination of the magnets, different operating temperature, and different nominal current, as summarized in Tab. 2.3. In the IPQ circuits the connections between the power converters and the individually powered magnets MQMs or MQYs, are made with a three-conductor. The central conductor carries only the difference of currents flowing in the two magnets that are connected with reversed polarity. The other two conductors carry the current of the two magnet apertures that are individually powered. In Fig. 2.6 and Fig. 2.7 are shown the schematic of the circuit in configuration 2in1 (one magnet i.e. two apertures) and 4in1 (two magnets i.e. four

FIGURE 2.6:   Schematic of the IPQ superconducting circuit, in one
magnet configuration (two apertures).

FIGURE 2.7:   Schematic of the IPQ superconducting circuit, in two
magnets configuration (four apertures).

apertures), respectively.

To connect the individual magnets to the others, superconducting bus-bars are used. Superconducting bus-bars consist of a superconducting cable, which is thermally and electrically coupled to a copper tube all along its length. The copper tube provides an alternative path for the magnet current in case of quenches. The copper cross-section area of a bus-bar pair is optimized for the current decay rate of the corresponding electrical circuit. For the quadrupole connection (420 A/s) the bus-bar has only 148 mm^2 of copper, while the bus-bar insulation has a breakdown voltage to ground of more 4 kV in helium gas under all conditions [32]. The quadrupole magnets in the IPQ circuits (MQM and MQY) are powered individually with a current of up to 6 kA. The two apertures of the magnets have different functions, for this reason they are

connected in different circuits. In case of a quench in one of these magnets, or to the superconducting components connected to it, quench heaters act on both apertures, leading to an energy extraction time of less 0.3 s at nominal current [26].

2.2.1 Powering and Protection of the IPQ circuit

The IPQ superconducting circuit is composed of the following components [32]:

- Power Converter (PC).
- Quadrupole magnets (MQY or MQM).
- Earthing circuit (EC).
- Warm resistances (WR).

In the simplified schematic of the IPQ circuit shown in Fig. 2.8, all the main parts of the circuit are highlighted. The power converters are marked in red, the apertures of the main quadrupole magnet in blue,the earthing circuit in grey, and the warm resistances of the circuit in black. Each warm resistance contains the resistance of current leads and others connections. The power converter, that is rated for 6 kA and +-8 V, can be seen as the main module which contains sub-modules. The three main parts of the Power Convert (High Precision Current Sensor, Power Part, and a Digital Controller) were designed and manufactured separately; finally they are integrated into a housing rack, as shown in Fig. 2.9. The power converter is normally assembled using a n+1 Power Bricks [+2 kA +08 V] (shown in Fig 2.10) to provide active redundancy in case of one sub-converter is lost. The power brick is a high-frequency current source (7-8kHz) controlled by a bandwidth voltage loop [32].
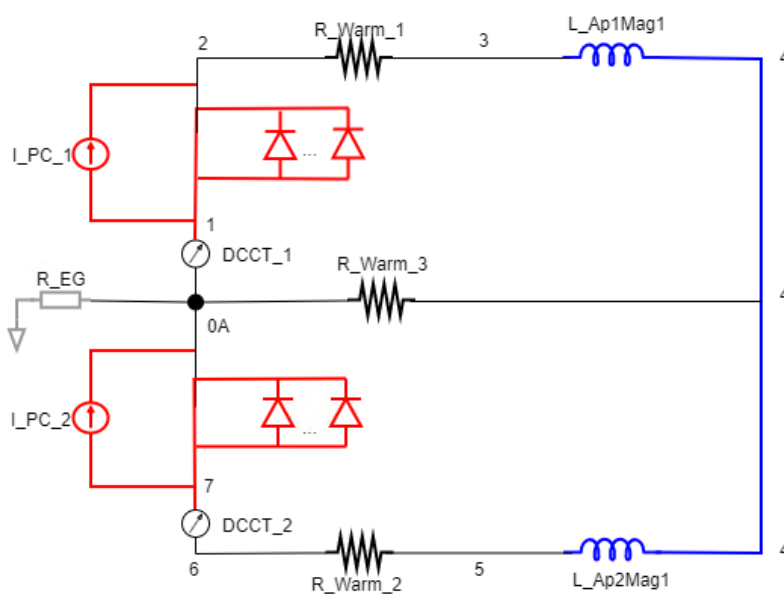
FIGURE 2.8: Simplified schematic of the IPQ for one magnet configuration.

The circuit power converter is also an important part of the magnet protection scheme, even if not directly fully responsible for the monitoring and diagnostic of the superconductive magnet status. The main tasks request from the power converter are: to stop powering the load in a safe way (this passive system is based on different paths using several free-wheeling diodes), to monitor the earth current of the circuit, and to ensure that the external protection system can stop the power converter through a safe signal called Fast Abort. The earthing circuit can be considered as part of the power converter. It provides a known and reliable connection of the circuit to ground. In addition, it allows the detection of earth faults and limits the current to ground in case of a failure.

FIGURE 2.9: LHC quadrupole power converter [32].
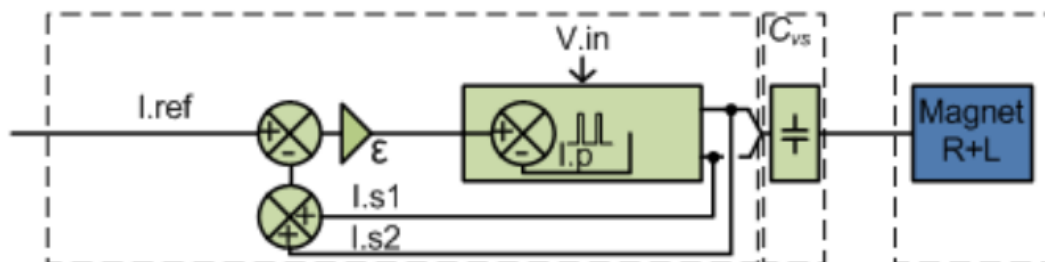
FIGURE 2.10: 2kA-8V Power Brick, high frequency. Marked in green, the current source, and in blue the load [32].

3 Modelling of the LHC superconducting circuit library

The superconducting circuits are composed of different elements, at different temperatures, in different materials, connected to each other in a multi-scale and multi-physics domain. The reason to generate and validate these models is driven by the necessity to realize an efficient and reliable multi-physics library of all the LHC superconducting circuits to simulate transients during normal operation of the machine, failure cases, and unexpected events.

To simulate this complex scenario, the STEAM (Simulation of Transient Effects in Accelerator Magnets) framework was developed in the Machine Protection and Electrical Integrity Group (MPE) at CERN. The main goal of STEAM is to simulate transients occurring in superconducting magnets and circuits using validated tools.

The models of the superconducting circuits and their magnets are developed using tools dedicated to the semi-automatic generation of netlist-based electrical circuit models, and electro-thermal models. Electro-magnetic, thermal, and mechanical transients are simulated with commercial tools or with tools generated within the STEAM team.

The use of automated model generation accelerates the building process of the models and allows easy, consistent model versioning. [1].

During this thesis, the main programs used are: PSpice$^{©}$ (a commercial tool used to generate the electrical circuit model), STEAM-LEDET (a STEAM in-house tool, used to model electro-thermal transients in superconducting magnets), and STEAM-COSIM (used to perform cooperative simulations combining both models, PSpice$^{©}$ and STEAM-LEDET).

3.1 Electrical model of the circuit using Cadence PSpice©

The electrical model of the IPQ circuits is developed with the Cadence suite (based on PSpice©). PSpice© is a program for generating and simulating electrical circuit models. During this thesis, the circuit models have been generated as netlists, without the graphical interface.

A netlist is a description of the connectivity between different electrical parts of the circuit and can contain electrical elements, like voltage or current sources, resistors, capacitors, inductors, and diodes.

The use of the netlists can bring some advantages such as:

- Fast correction of mistakes.
- Generation of circuits with many identical components thanks to the automatization.
- Change and adaption of circuits and circuit components can be achieved quickly.

But also some disadvantage as the missing graphical user interface.

3.1.1 Circuit parameters

The IPQ circuits in the LHC ring are 78 (the main parameters are summarized in Appendix A), in two different configuration: with one quadrupole magnet, i.e. with two apertures individually powered (see Fig. 2.6), and with two quadrupole magnets in series, i.e. four apertures individually powered (see Fig. 2.7). The main components of the circuit are: 2 power converters, 20 diodes in parallel to each power converter, 2 DCCT (Direct Current Current transformer) to measure the current with high accuracy, 3 warm current leads, 1 earth resistance, and 2 or 4 magnet apertures.

In the electrical circuit models, the quadrupole magnets are included as simple inductances with a constant assigned value. This assumption is reasonable during the generation and validation of the electrical circuit models, while during the co-simulations, the magnet parameters come from a specific tool STEAM-LEDET, used for the electro-thermal analysis [33].

The self and mutual inductance of the magnet apertures used on the electrical circuit model, are calculated using STEAM-SMIC (Self-Mutual Inductance Calculator) [34]. STEAM-SMIC is a ready-to-use program to calculate the self and mutual inductance per unit length between the turns of the magnet. To use in the electrical circuit model the self and mutual inductance per unit length obtained by SMIC is necessary to multiply them for f_L and the magnet length, where f_L is a current-dependent parameter that takes into account the effect of iron-yoke saturation on the differential inductance. It is possible to calculate f_L in function of the current with COMSOL©, Roxie [35], or other software that take care of the iron yoke saturation in the magnet.

The magnetic flux between the coils can be defined by the coupling coefficient $k_{ApMag12} = \frac{M_{12}}{\sqrt{L_{Ap1Mag} \cdot L_{Ap2Mag}}}$, where M_{12} is the mutual inductance between the two apertures of the magnet, and L_{Ap1Mag} and L_{Ap2Mag} are the self inductances of each coil. The warm resistances R_{warm_i} $[\Omega]$ in the electrical circuit model are three, one in each branch respectively.

An average value of R_{warm_1} and R_{warm_2} is given in the circuit database layout [36] for each IPQ circuit, but in order to have a better agreement with the experimental data during the validation of the electrical circuit model, the warm resistances have been re-calculated. To calculate the warm resistances of the circuit, two Slow Power Abort (SPA) tests have been used as a reference: one test with different currents in the two magnet apertures, and the other with the same value of current in both magnet apertures. The three circuit equations 3.1, in stationary regime, are used for the calculation of the warm resistances. The reference schematic for the equations 3.1 is shown in Fig. 2.6.

$$\begin{cases} V_{PC\_1} = R_{warm\_1}I_1 + L_1 \cdot \dot{I}_1 + M_{12} \cdot \dot{I}_2 - R_{warm\_3} \cdot I_3 \\ V_{PC\_2} = R_{warm\_2} \cdot I_2 + L_2 \cdot \dot{I}_2 + M_{12} \cdot \dot{I}_1 + R_{warm\_3} \cdot I_3 \\ I_1 + I_3 = I_2 \end{cases} \qquad (3.1)$$

Where R_{warm_i} is the warm resistance of the branch i, I_i is the current flowing in the branch i, L_i is the self inductance of the aperture i, and M_{12} is the mutual inductance between the magnet apertures.

To be faster in the warm resistance calculation, a SWAN (Service for Web based ANalysis) notebook (which will be better described in section 3.1.2) was generated. The goal of this notebook is to find the correct values of the warm resistances in a semi-automatic mode using the tests performed during the LHC Hardware Commissioning [37]. To collect the SPA necessary for the calculation of the warm resistances, the notebook uses the signal acquired with the LHC signal monitor [38], which represents an efficient way to access data from tests in LHC. The tests are selected based on the minimum current through the magnet apertures, a minimum stable length of the experiment, and a tolerance of the current variation in time. When the two tests are found (an example of the two tests is shown in Fig. 3.1), measured currents and voltages are used to calculate the R_{warm_i} values.

3.1.2   STEAM-SING Notebook

As mentioned in paragraph 3.1.1, the IPQ electrical circuits in the LHC are 78. To generate faster and in a semi-automatic mode the circuits netlists, a SWAN notebook was used. SWAN works in the CERN cloud space with an interface similar to the Jupyter notebook [39]. The notebook is a document that can contain code, text elements, links, figures, equations,etc. The notebooks are divided into cells where the user can type code, execute it, and see the results.

The SWAN notebooks are used to generate the models of different magnets/circuits, but it works also as a repository of data, queried to provide relevant information with
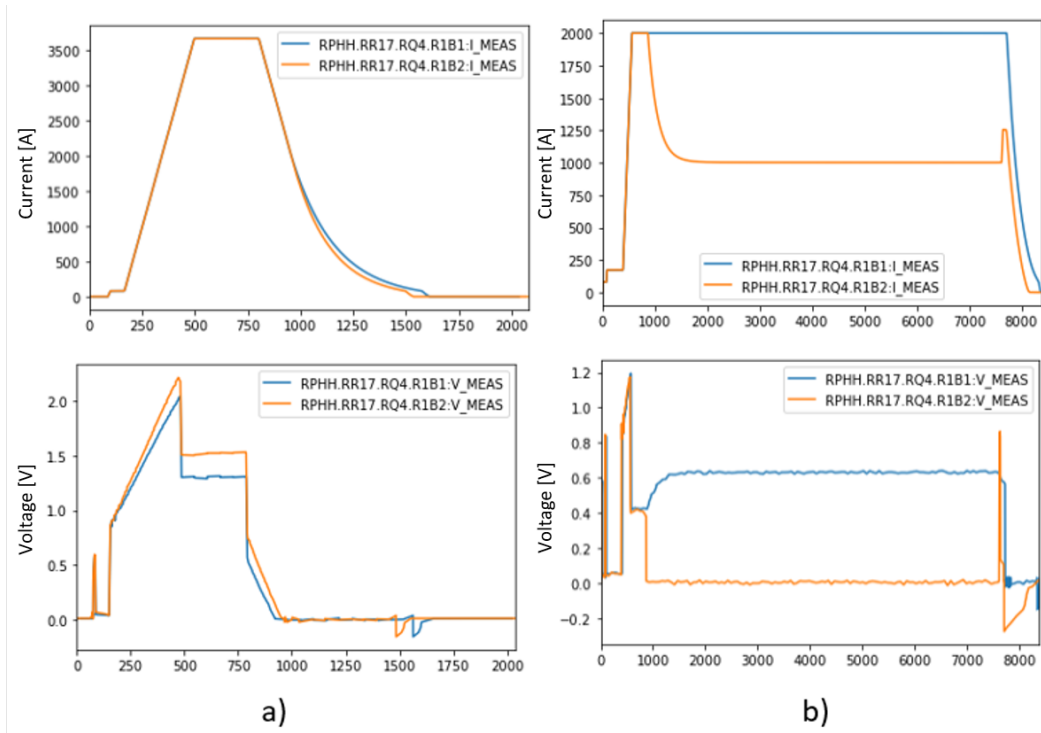
FIGURE 3.1: Tests found by the notebook. a) Current and voltage measures versus time in case of the same current value in both magnet apertures. b) Current and voltage measures versus time in case of different current values in the magnet apertures.

eventually rapidly update of the models in case of new features; furthermore the use of notebooks reduces the probability of mistakes thanks to the visualization of the parameters in the plots.

During this thesis two STEAM python packages are used on the notebooks. Steam-nb-api is used to parse ROXIE input files, generate magnet models, and write STEAM-LEDET input files, while the package steam-lhc-sm-api is used to acquire signals from LHC circuits. The package STEAM-SING [40], imported at the beginning of the SWAN PSpice© notebook [41], is a Java package to conveniently write PSpice© netlists. In Fig. 3.2 it is possible to see a cells overview of the SWAN notebook used to generate the PSpice© netlist for the electrical circuit models using STEAM-SING. The second cell of the netbook (*Import Java gateway and STEAM notebook API*) is used to call the packages necessary to generate the netlist using STEM-STING, read excel files, needed libraries, etc. The following cells are used to create the correct netlist template and set the path necessary to call the libraries containing the stimulus and the sub-tracks of the model. The only parameter that an external user must fill to generate different models for different IPQ circuits, is the *Circuit Name*. Once the *Circuit Name* has been entered the code sets automatically the global parameters. The IPQ global parameters are saved in an excel file that contains all the main information of the circuit: warm resistance values, number of magnets, self and mutual inductance of the magnet apertures, nominal current, name of the power converter, and operating temperature. Other components as the diodes, parasitic

components, and power converters will be read as sub-track of the circuit stored in a library of sub-components, which is maintained on Gitlab [42, 43]. Each sub-track is called according to the name of the circuit power converter.

In the remaining cells of the notebook, the connections of the components are defined. In case of single and constant component, as the earthing resistance, the value is assigned directly in the code ($R_{EG}= 1$ [GΩ]).

The last three cells of the notebook are dedicated to defining the simulation options, print the circuit netlist, and write them into a file.

FIGURE 3.2: General overview of the cells that make up the notebook used to generate the electrical circuit models.

3.2   Electro-thermal model of the magnet using STEAM-LEDET

To model the electro-thermal behaviour of the superconducting magnet a specific in-house tool of STEAM is used.

STEAM-LEDET is a tool that runs as a stand-alone executable and can reproduce the non-linear magnet behaviour [33]. LEDET (Lumped-Element-Dynamic-Electro-Thermal) approach consist in a network of non-linear lumped-elements to analyze the magnets [15]. Three sub-networks are used to reproduce the completed behaviour of the superconducting magnet during the simulation:

- Electrical sub-network: reproduce the electrical transient behaviour. It contains conventional electrical lumped-elements as voltage, current, inductance, etc.
- Thermal sub-network: reproduce the thermal transient behaviour in the cable cross-section. The thermal system can be represented as an electrical network where any current flowing in a branch of the circuit is equivalent to a heat flow and the potential of any node is equivalent to a temperature.
- Coupling currents sub-network: represents the electro-magnetic transient of the inter-filament (IFCC) and inter-strand coupling currents (ISCC) in the superconducting cable.

With the coupling currents sub-network, STEAM-LEDET includes non-linear dynamic effects such as the dependence of the magnet differential self-inductance to the presence of inter-filament and inter-strand coupling currents in the conductors. The same simulation environment can simultaneously model macroscopic electrical transients and phenomena at the level of the superconducting strands.

STEAM-LEDET is not just a useful tool for reproducing the magnet behaviour, but it is also a functional program to predict the performance of conventional quench protection systems based on energy extraction (EE), quench heaters (QH), and CLIQ (Coupling-Loss Induced Quench) protection system [33, 15].

At the end of each simulation STEAM-LEDET generates a report with the main information about the simulation. Figures, GIFs, and .mat and text files for the post-processing are also produce at the end of each simulation.

3.2.1   Interfilament and interstrand coupling losses

The losses in a superconducting cable can be divided into inter-filament coupling losses (IFCL) [19] and inter-strand coupling losses (ISCL) [19]. When a superconductor cable is subjected to a variable magnetic field dB_a/dt [Ts^{-1}], an induced magnetic field is generated in the opposite direction B_if [T].

The coupling currents generated by the magnetic field variation between filaments and strands flow through the stabilizer (copper in the Nb-Ti magnets) developing

ohmic losses. The power (per conductor volume [Wm^{-3}]) generated due to the magnetic field variation can be calculate using the equations 3.2 and 3.3 for IFCL and ISCL respectively [15].

$$P_{if}''' = \left(\frac{l_f}{2\pi}\right)^2 \frac{1}{\rho_{eff}\left(\frac{dB_t}{dt}\right)^2} = \frac{2}{\mu_0}\tau_{if}\left(\frac{dB_t}{dt}\right)^2 \tag{3.2}$$

$$P_{is}''' = \frac{2}{\mu_0}\tau_{is}\left(\frac{dB_{t\perp}}{dt}\right)^2 \tag{3.3}$$

The parameter τ_{if} [s] is a time constant that describes the development of the inter-filament coupling currents. It is possible describe this time constant with the equation 3.4 [19]. [15]:

$$\tau_{if} = \frac{\mu_0}{2}\left(\frac{L_f}{2\pi}\right)^2 \frac{1}{\rho_m f_{eff}} \tag{3.4}$$

Where L$_f$ [m] is the filament twist-pitch, ρ_m [Ωm] is the matrix resistivity, μ_0 [TmA^{-1}] is the magnet permeability in the vacuum, and f$_{eff}$ depend to the superconductor fraction in the matrix on the interface resistance between the filaments, the matrix, and the position of the filaments in the wire cross-section.

Once the ISCC are induced, the ISCC through the contact resistance between two crossing strands. In this case, the perpendicular component is taken into account and the time constant [s] (3.3) can be described as in equation 3.5 [19].

$$\tau_{is} = C\frac{L_s(N_s^2 - 4N_s)}{R_c} \tag{3.5}$$

Where R$_c$ [Ω] is the contact resistance between the strands, L$_s$ [m] is the strand twist-pitch, N$_s$ [-] is the number of the strands, and C [Ωm^{-1}] is a fitting constant that varies between 1.6·10^{-8} and 1.7·10^{-8}.

STEAM-LEDET can offer a quantitative estimation of the coupling-loss contribution to the discharge and provide realistic information to asses and optimize the protection systems.

3.2.2 Heat transfer in the magnet model

The temperature is a critical factor in a superconducting magnet, so it is important modelling the heat propagation precisely.

The superconducting cables are composed of different materials, so the specific heat capacity of each cable is calculated as the sum of the different heat capacities, multiplied for the fraction of the component. The different heat capacities taken into account by the model are: copper, superconductor, insulation, and internal and external voids. The specific heat capacity (per unit length [J/(mK)]) for each half-turns
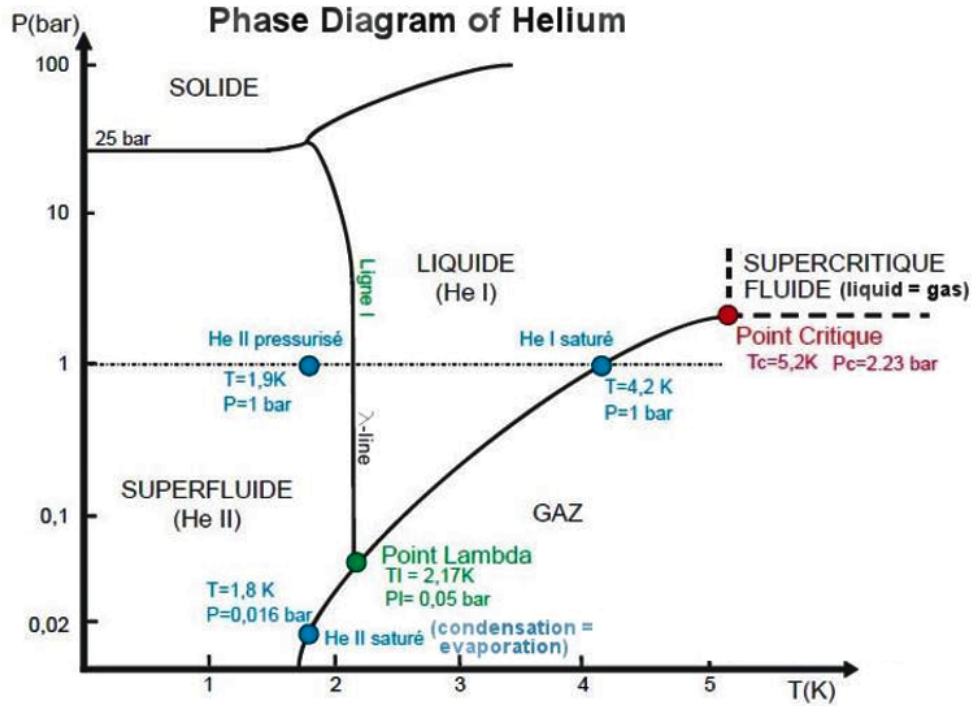
FIGURE 3.3: Phase diagram of the helium [44]

is described in equation 3.6.

$$C_{tot} = (f_{Cu}c_{v,Cu} + f_{SC}c_{v,SC} + f_{ins}c_{v,ins} + f_{inVoids}c_{v,inVoids} + f_{extVoids}c_{v,extVoids}) \quad (3.6)$$

Another important material involved with the heat transfer in the superconducting magnet is the helium. The helium (also called *quantum fluid* to emphasize the uniqueness of its properties) is the only substance in nature that does not solidify at atmospheric pressure even at 0 K. The phase diagram of the helium is shown in Fig.3.3; it is catheterized by three regions: vapor phase, liquid phase (divided in two zones: liquid (HeI) and superfluid (HeII)) and solid phase. Helium is the only element in which the fusion line and the saturation line never meet. At atmospheric pressure, the helium becomes liquid at 4.22 K while at 2.17 K there is a further phase transition between the liquid phase and the superfluid phase.

Estimating the correct volume of superfluid helium involved in the heat exchange with the magnet coils is a challenge, in particular on the magnet not impregnate. Some magnets are not fully impregnated with the epoxy, this implies the presence of the voids inside the cable cross-section. These voids can be filled by the superfluid helium, making cooling effect more relevant to the thermal evolution of the cable. To give an idea of the influence of the helium during the heat exchange, the heat capacity of different materials are shown in Fig. 3.4. For example, the volumetric heat capacity of the helium is $7 \cdot 10^5$ [J/m^3/K] instead of the heat capacity of the kapton that is $2 \cdot 10^2$ [J/m^3/K] at cryogenic temperature [45]. In particular, the heat capacity of the helium is highly non-linear between 1.9 K (the operational temperature) and
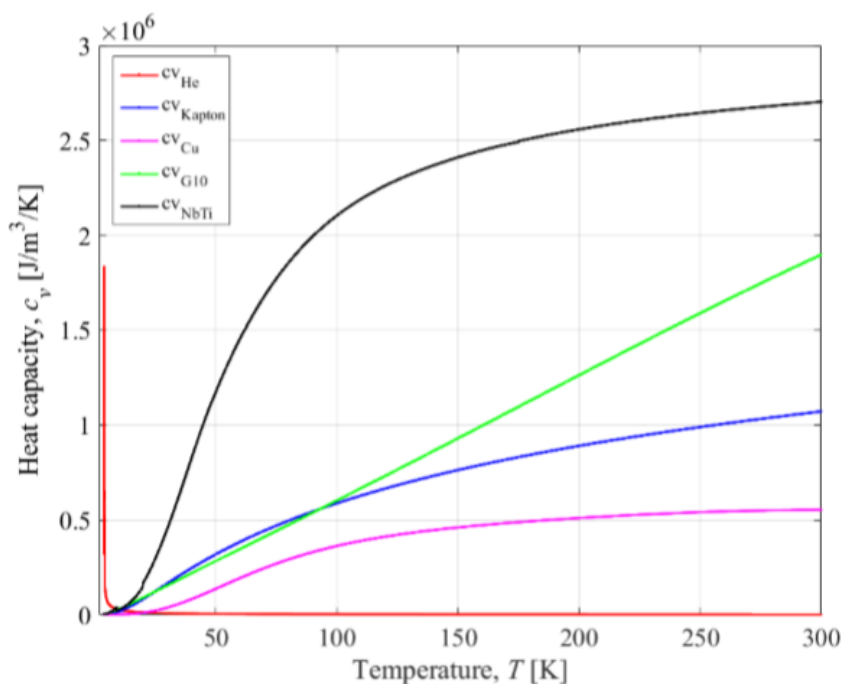
FIGURE 3.4: Heat capacity for different materials [46, 47].
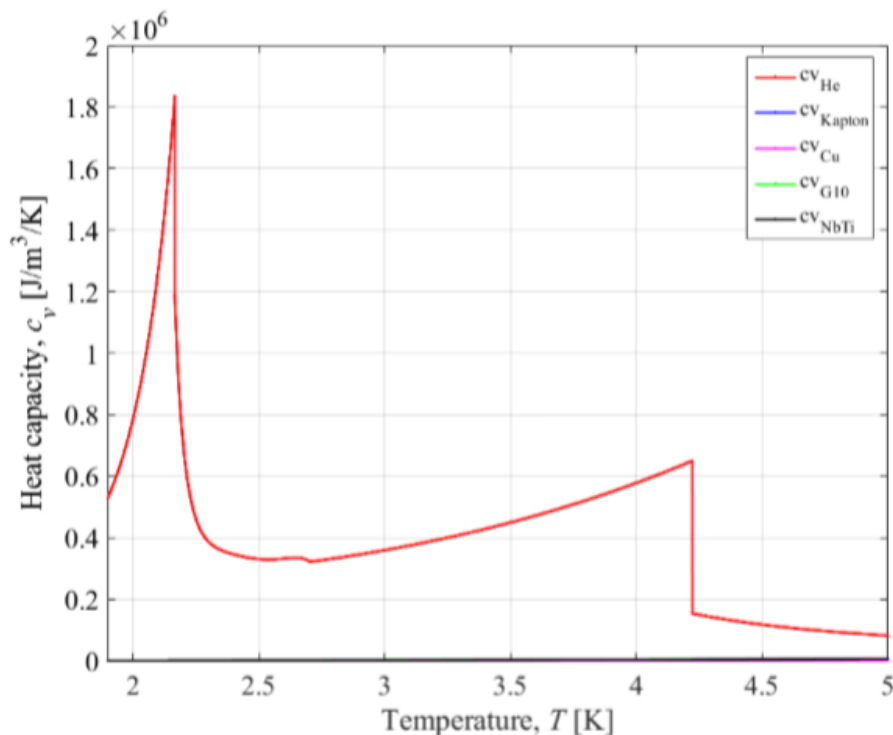
FIGURE 3.5: Heat capacity of the Helium [46, 47].

10 K as shown in Fig. 3.5. Above 10 K the volumetric heat capacity of the helium becomes negligible compared to that of copper.
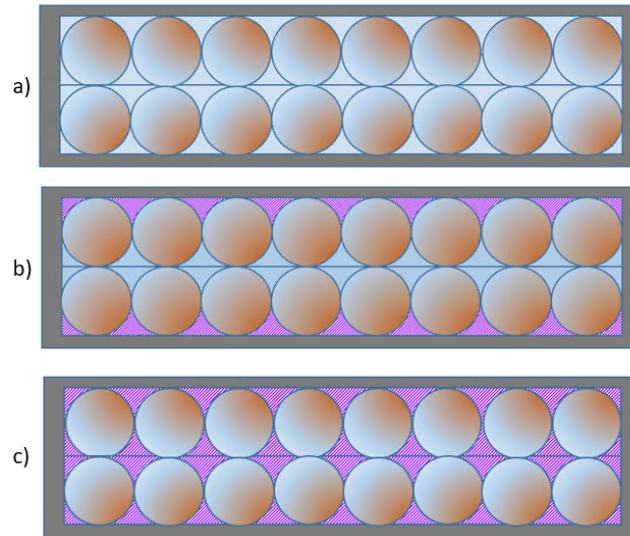
FIGURE 3.6: Quantity of helium inside the insulated cable-cross section: (a) All the voids are filled with helium. (b) Half of the voids are filled with the helium and the remaining part is filled with the insulation. (c) All the voids are filled with the insulation, the quantity of helium inside the cable cross section is zero.

The STEAM-LEDET tool gives the possibility to take into account the helium effect with two different features. The first feature allows to model the heat exchange between the coil turns and a thermal sink at a constant temperature equal to the helium bath temperature. The second feature, in case of not impregnated cable, takes care of the voids inside the insulated cable cross-section. These voids can be filled by the infiltrated helium (once the magnet is immersed in the helium bath), by the insulation deformed due to the Lorentz forces, or partially by both. A very simple schematic of the insulated cable cross-sections for these three different possibilities is shown in Fig. 3.6. In Fig. 3.6 (a) all the voids are filled with the helium (blue background inside the cable cross-section), in Fig. 3.6 (c) all the voids are filled with the insulation (purple background in the cable-cross section), and in Fig. 3.6 (b) the voids are filled half with the helium and half with the insulation (blue and purple background in the cable-cross section).

3.2.3   Quench propagation

During a quench the temperature starts to increase in a region of the coil. The resistance on this region grows due to the transition of the superconducting material in a normal conducting one. Furthermore the passage of the current on the cable copper matrix generates ohmic losses. Due to these effects, the quench can propagate in all the directions and to the neighboring cables.
A common way to represent the quench velocity propagation in a superconducting cable is: [16, 48]

$$v_{qp} = \frac{J}{c_v} \sqrt{\frac{\rho_{el} k}{T_s - T_0}} \frac{1 - 2y}{\sqrt{yz^2 + z + 1 - y}} \tag{3.7}$$

Where J [A/mm^2] is the operating current density in the conductor, ρ_{el} [Ωm] is the electrical resistivity, and k [W/(mK)] is the thermal conductivity. The temperatures T_0 [K] and T_s [K] are the initial operating temperature and the average between the current sharing temperature and the critical temperature, respectively [16]. All these parameters have already been introduced in chapter 1. The first two terms of equation 3.7 represent the adiabatic quench velocity propagation (which does not take into account the helium cooling) while the last part of the equation 3.7 represent the non-adiabatic behaviour. The terms z and y are the corrections to the adiabatic propagation velocity, arising from steady-state and transient heat-transfer, respectively.
STEAM-LEDET is a 2D software, therefore all the simulations consider a coil cross-section transverse to the direction of the transport current. Once a quench appears in the 2D magnet model, it spreads immediately to the entire length of the turns. To represent the quench propagation phenomena in a more realistic way, the resistance of each turn is scaled of a fraction related to the contact area between the heating stations and the magnet turns, changing the model from 2D to 2D+1D. This behaviour does not represent a complete 3D model of the magnet, but only a simplified combination. In the new model 2D+1D, at the moment of the quench, only the regions of the magnet in contact with the heating stations quench immediately. The rest of the magnet, in the longitudinal direction, starts to quench with a certain velocity propagation that introduces in the simulation a delay Δt, as is shown in Fig. 3.7. The quench velocity propagation depends on the magnetic field, the current density, and a scaling factor, that depends on the cooling effects in the magnet model [49].

3.2.4   Notebook

The STEAM-LEDET file contains all the parameters of the magnet. To generate this file in a semi-automatic way, a dedicated SWAN notebook [50] has been used. An introduction to SWAN was given in paragraph 3.1.2.
An overview of all the cells created to generate the STEAM-LEDET input file on the SWAN notebook is shown in Fig.3.8. The input data to use for starting the generation of the model using the notebook are the main parameters of the magnet
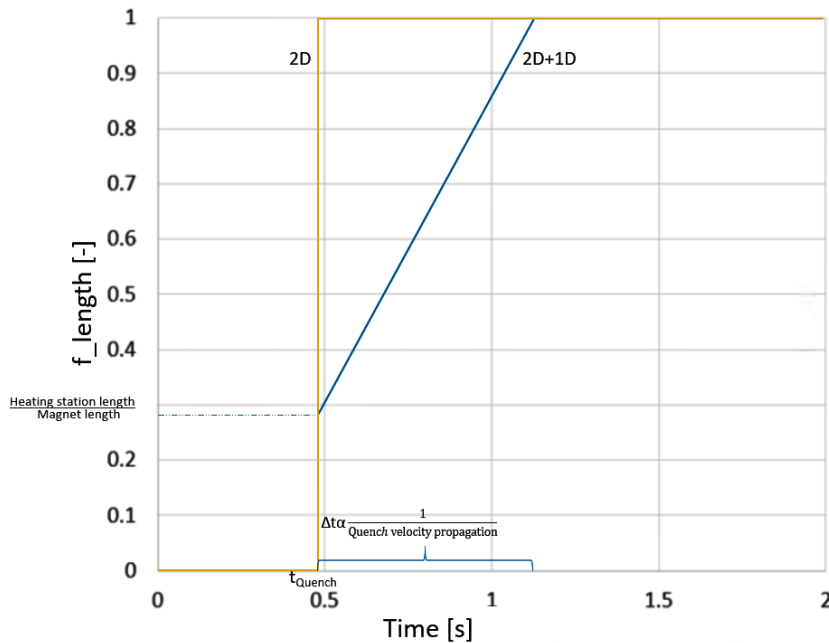
FIGURE 3.7: Longitudinal fraction of magnet turns quenched in time. The yellow curve represents the fraction of the magnet turn quenched in time on the 2D model. It quenches immediately the entire length of the turn. The blue curve represents the 2D+1D model. In this case, only the fraction of the turn in direct contact with the heating station quenches immediately.

and the magnetic field maps from ROXIE, a program developed at CERN for the electromagnetic simulation and optimization of accelerator magnets [35]. These data are used to realize the magnet geometry on the notebook, an example is shown in Fig. 3.9. The polarities, the electrical connections, the magnet and conductors parameters, and the simulation options will be defined into dedicated cells of the notebook.

Using the SWAN notebook to generates the LEDET input files allows generating the models with uniformity, among different magnets, and composing a repository of data queried to provide relevant information with eventually rapidly update of the models in case of new features; furthermore, the use of notebooks reduces the probability of mistakes thanks to the visualization of the parameters in plots. Examples of these plots, used to visualize and check the connections, are shown in Fig. 3.10 and Fig. 3.11.

In Fig. 3.11 the heat exchange connections between the adjacent half-turns can be observed. In the SWAN notebook it is also possible use a graphic method to check the thermal contact between the quench heaters strips and the magnet half-turns. For example, in Fig. 3.12 the half-turns in touch with the quench heater strips are highlighted. The last three cells of the notebook are dedicated to the generation of the LEDET input file, in the format of an excel file.

The excel file is composed by three sheets. The first one its called *Inputs*. It contains all the variables that define cable, strand, coil proprieties, the parameters to define
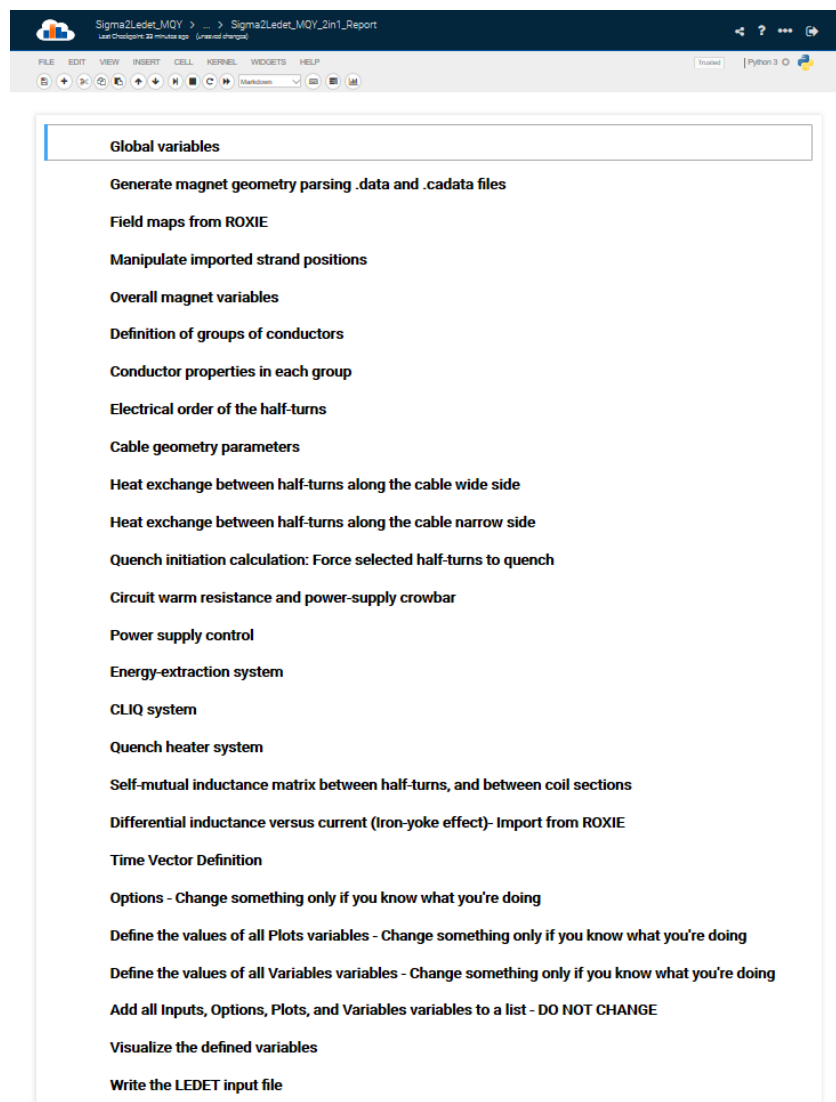
FIGURE 3.8: Complete overview of all the cells that compose the SWAN notebook.

the heat exchange, the electrical connection, and the quench protection systems. In the second sheet, *Options*, two sets of variables can be defined: the variables that affect either how the simulation runs, and the post-processing options. The last two sheets, *Plots* and *Variables*, are used to define the optional plots, which will be saved at the end of the simulations, and the variables to insert in a text file with the possibility to choose whether to save all their entire history or only their final state.
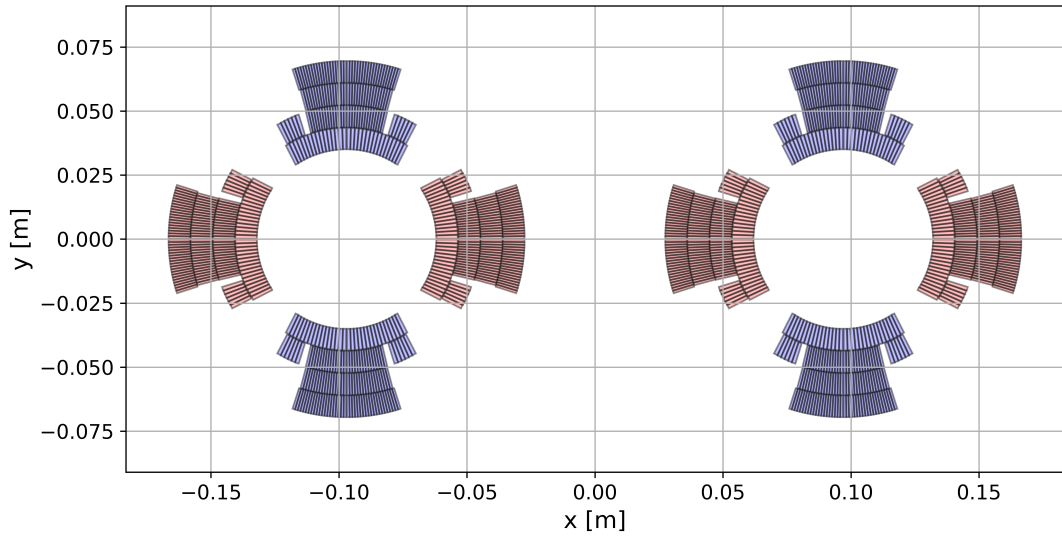
FIGURE 3.9:   MQY quadrupole magnet geometry generated by the
SWAN notebook.
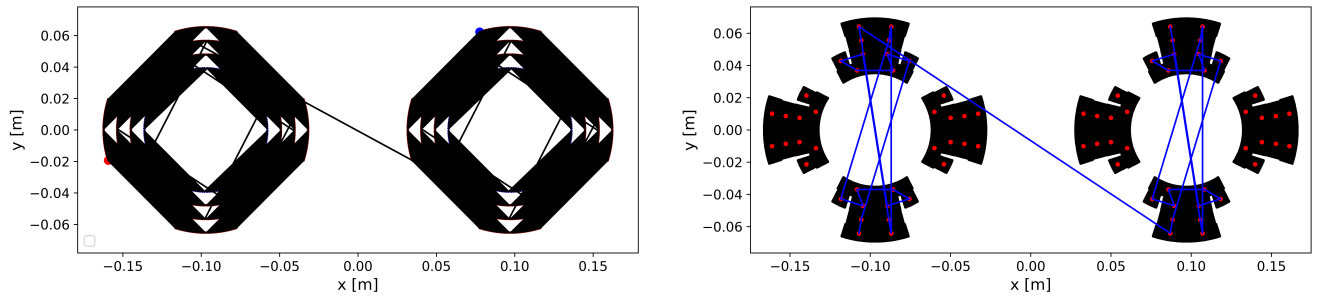
FIGURE 3.10: Electrical order of the half-turns (a) and groups (b) of the
MQY magnet generated by the SWAN notebook.

3.3   Co-simulation   of   the   circuit   model   using STEAM-COSIM

Once the magnet model and the circuit model are generated and validated, both are combined within a co-simulation to performed with the software STEAM-COSIM [51]. The necessity to combine models arises when a quench occurs in particular conditions that can not be reproduced in a stand-alone simulation, for example in case of different currents in the magnet apertures.

The coupled tools, combined by STEAM-COSIM during the validation of the IPQ circuits, are PSpice$^{©}$, for the electrical circuit model, and STEAM-LEDET, for the electro-thermal model.

STEAM-COSIM is a framework based on cooperative simulation developed at CERN. The core of the co-simulation is to exchange information between several models in order to obtain a consistent solution. The signals exchanged during the co-simulation are the heart of the co-simulation algorithm.
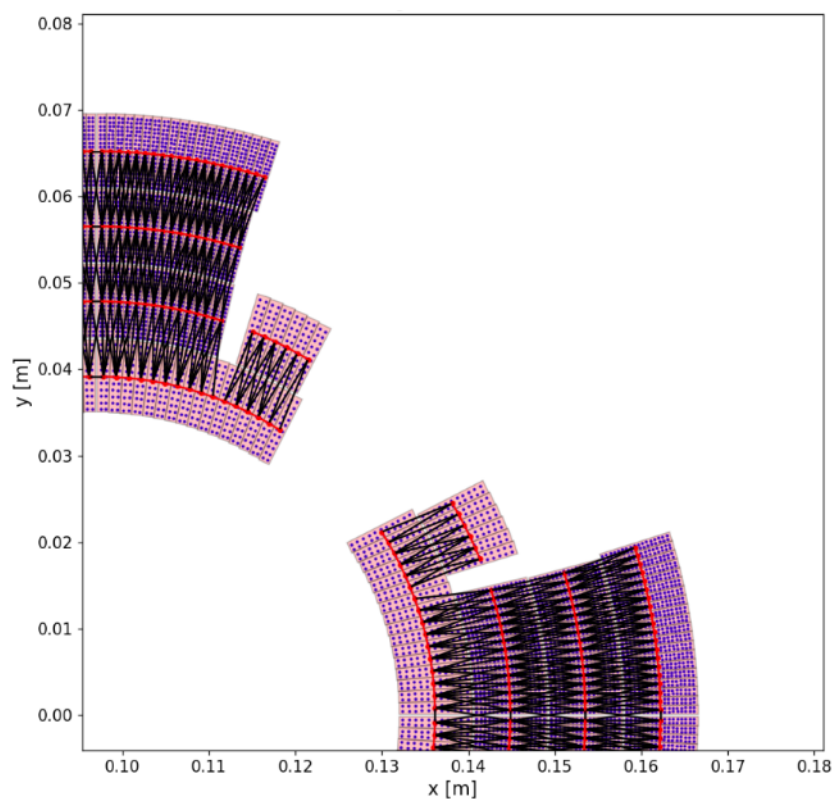
FIGURE 3.11: Heat exchange connections between the half-turns of the MQY magnet. The red lines represent the heat exchange along the cable wide side, while the black lines represent the heat exchange along the cable narrow side. The blue color on the figure are dots that represent the strands in each half-turn.
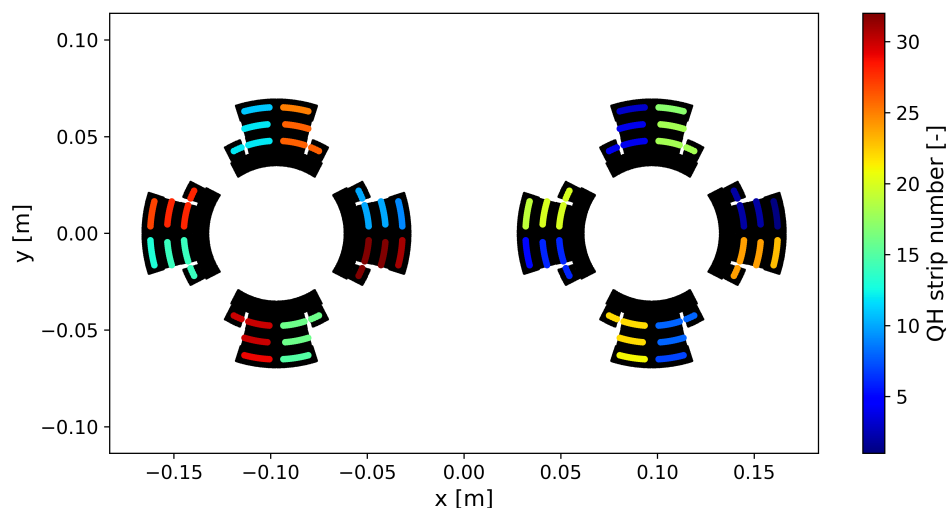
FIGURE 3.12: Heat exchange between half-turns and quench heaters generated by the SWAN notebook. The half-turns to which quench heater strips are attached are highlighted with colored points. The different colors follow the number of the quench heater strips assumed in the LEDET file.
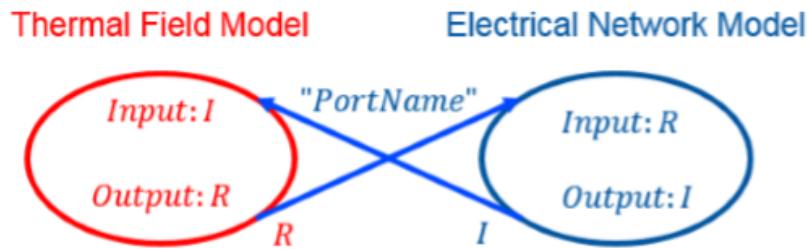
FIGURE 3.13: Representation of two ports, exchanging information [51]

The parameter exchange is based on the concept of ports, as is shown in Fig. 3.13. Each port is composed of a name and a component label (as input and/or output components).The number of the ports of the electrical circuit depends to the number on the magnet apertures in the circuit, while the magnet model has a number of ports equal to the number of the coil section of the magnet [51, 52]. The algorithm of the COSIM framework is based on the demand of input value for each port, then store the corresponding output signal in the port [51, 52].

STEAM-COSIM starts running from the PSpice[©] circuit model, for a defined time-window, with a defined time-step. After the first iteration, the electrical circuit model provides a calculated current to the magnet model. In the next step, STEAM-LEDET runs a simulation with the current value gives from PSpice[©], for the same time windows, and provides new resistances and inductive values to the electrical circuit model in PSpice[©]. An example of the signal exchange between the domains during the co-simulation is shown in Fig. 3.14. In Fig. 3.14 the cross-sections of the two magnet apertures (on the right side) represent the STEAM-LEDET magnet model, while the electrical circuit (on the left side) represent the PSpice[©] circuit model. I^kcircuit, U^{k-1}, and R^{k-1} are the values exchanged between the two models at each iteration.

Before starting with the co-simulation a pre-conditioner is needed to improve convergence. The pre-conditioner is used to introduce elements that act on the first order approximation [51]. The pre-conditioner contains the coupling parameters of both models, in this case: the circuit current (calculated by PSpice[©]), the inductive voltage (calculated by STEAM-LEDET), and the resistance of the quenched magnet (calculated by STEAM-LEDET). Even if the pre-conditioner is present, both models are solved individually.

The iteration, with the same time-window, will be repeated until the convergence level, in terms of the set relative and absolute error, is achieved. During the iteration steps, better and better approximations of the results are reproduced within the algorithm over the entire time interval [51].
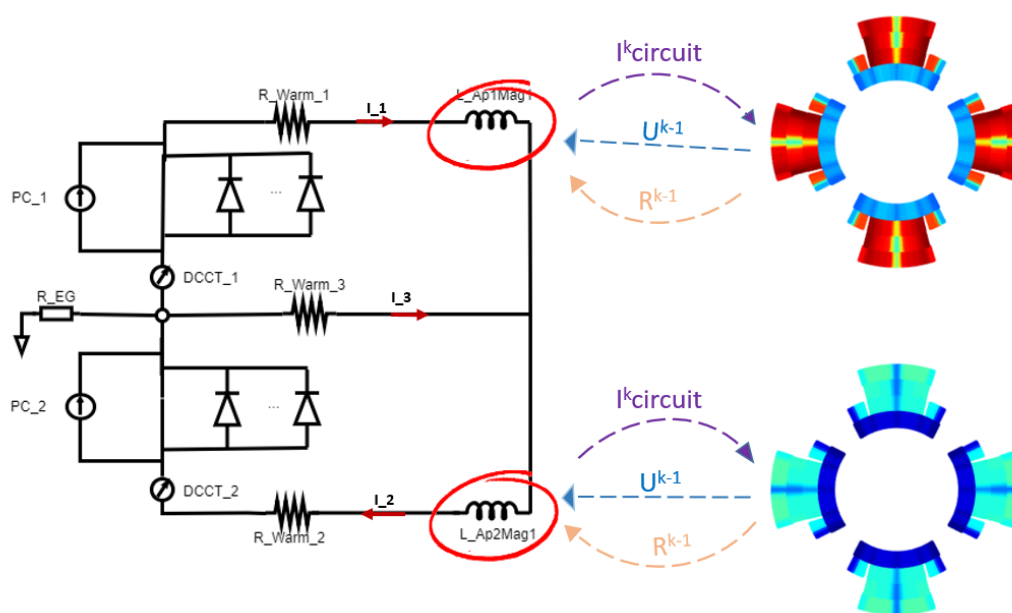
FIGURE 3.14: Working principle of the co-simulation on the LHC quadrupole circuit and the magnet.

3.3.1 Notebook

In order to be able to run a co-simulation using STEAM-COSIM, some modifications to the PSpice$^{©}$ circuit are needed.

Using a different SWAN notebook [41], an electrical circuit was created using STEAM-SMIC. This circuit model is very similar to the PSpice$^{©}$ one, described in paragraph 3.1. As mentioned before, the co-simulation needs to exchange information between two or more tools, so it is necessary introduce another library [53] in the circuit model (that contains all the magnet parameters) and others cells on the notebook that are used to generate the port and configuration files needed to the tool STEAM-COSIM. This permits to exchange data between PSpice$^{©}$ and STEAM-LEDET.

4 Simulation of electrical transients in IPQ circuits

As described in paragraph 3.1, the electrical circuit models of the IPQ are realized as a PSpice© netlist using STEAM-SING on the SWAN notebook.

Once all the electrical IPQ circuits models have been realized, it is necessary to validate them using experimental data, in particular Slow Power Abort (SPA).

The LHC is a complex machine, composed of many interconnected systems subject to deterioration. For this reason, to reduce the risk of accidents, there are several safety measures put in place, like the inspection of all superconducting circuits during the Hardware Commissioning (HWC) powering tests. The HWC tests consist of carrying out several powering cycles at different current levels for each superconducting circuit [54]. These tests are performed periodically to guarantee the functionality of the LHC machine by specialized teams and the signals are recorded in the LHC database.

There are several databases used for signal monitoring in the LHC [55].

- Post Mortem (PM): In the PM database, the data are stored in high resolution after a relevant event (e.g. a quench). The PM database contains transient data recorded by the different equipment systems of the LHC.
- CERN Accelerator Logging Service Data (CALS): The data extraction is performed using a Java API, and optionally a generic Graphical User Interface (GUI), called TIMBER, to visualize the data. It is persisted in Oracle RAC (Real Application Clusters) and stores approximately 2TB of data per week.
- Next CERN Accelerator Logging (NXCALS): is the new ideas based on Hadoop Big Data technologies using cluster computing power for the Data Analysis. Currently, NXCALS project is still under active development and the full operational swap from CALS to NXCALS is foreseen in the next future.

To collect the data from the LHC databases, a SWAN notebook, developed for the LHC signal monitoring project [38], was used. For the validation of the electrical circuits models different SPA tests performed between 2015 and 2018 were selected.

Before starting with the validation of the entire electrical circuit model, it is necessary to validate each component of the circuit. In the case of the IPQ circuits, the only components present, and a consequence to validate, are the diodes.

TABLE 4.1: PSpice© parameters adopted in the diode model.

```
          *Diode
      + IS=0.00171429
       + RS=0.00075
         + N=0.85
       + TT=1.00E-09
      + CJO=2.34E-08
     + VJ=0.390500001
     + M=0.257400508
        + EG=0.69
         + XTI=2
         + KF=0
         + AF=1
        + FC=0.5
        + BV=15
      + IBV=800E-03
          .ENDS
```

4.1   Diode validation

As mentioned before (in Section 3.1.1) the IPQ superconducting circuits include 20x2 diodes. As shown in Fig. 2.6, each stack of diodes is connected in parallel to the power converter. For the IPQ circuits, two different types of diode are used: the 245NQ015PbF [56] and the D4457N [57]. The 245NQ015PbF is used in all the power converters RPHH and some RPHGA, while for the power converters RPHGB and the rest RPHGA the D4457N is used.

In the PSpice© tool, some diode models are already embedded. These models are static and can not change during the simulation time, thus, to reproduce a specific behaviour, some parameters of the diode model have been changed. The PSpice© diode model can be described using Eq. 4.1. Where I_D is the current through the diode [A], I_s is the saturation current [A], V_D is the voltage across the diode [V], q is the charge of the electron [C], k is the Boltzmann's constant [J/K], and n is the ideality factor [-].

$$I_D = I_s \left(e^{\frac{qV_D}{nkT}} - 1 \right) \tag{4.1}$$

Both the simulated diodes in the circuits models are in good agreement with the experimental data using the parameters reported in Tab. 4.1. The diode parameters found during the validation of the component are saved in the IPQ sub-track on the GitLab steam-pspice-library [43]. This library is automatically called by PSpice© when the circuit is running.

The diode parameters chosen after the validation phase does not represent the diode behaviour given by the data-sheet [56] [57], as shown in Fig. 4.1.

However, this is not surprising because the working condition are different from the testing one. In Fig. 4.2 the forward current against the forward voltage in one diode is shown. The developed diode model has good agreement compared with the measurements during a real transient.
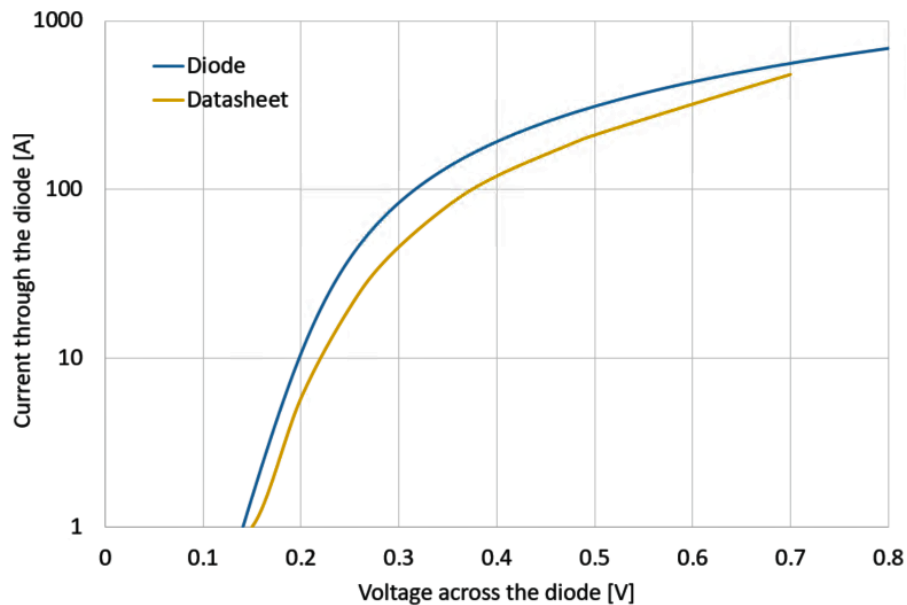
FIGURE 4.1: Diode forward characteristic curve, current versus voltage across the diode.Comparison between the data-sheet diode characteristic and the characteristic chosen during the validation of the diode.
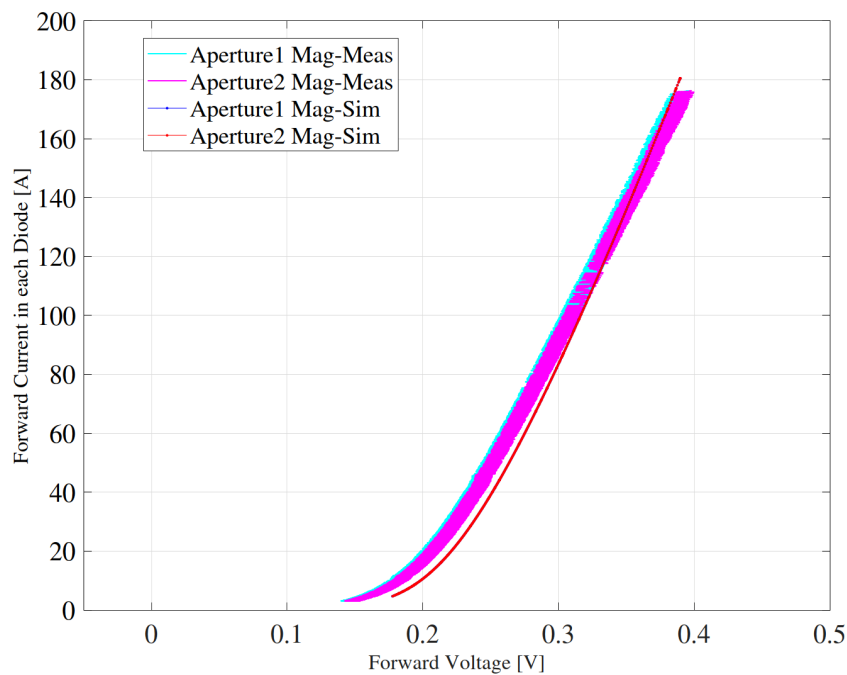
FIGURE 4.2: Forward Current vs Forward voltage. Comparison between simulated and the measured diode behaviour.

4.2 Parasitics components

Additional parasitic components are added in the electrical circuit model to increase its numerical robustness and improve convergence, as highlighted in Fig. 4.3. The values of these components are the same for all of the IPQ circuits and they help to reduce the high-frequency impedance of the diodes. The values of the parasitic components are summarized in Tab. 4.2.

TABLE 4.2: Values of the parasitic components in the IPQ circuit model.

Component Name	Value
C_C1	1 [pF]
C_C2	1 [pF]
R_R1	1 [Ω]
R_R2	1 [Ω]
R_R1_1	1 [kΩ]
R_R2_1	1 [kΩ]
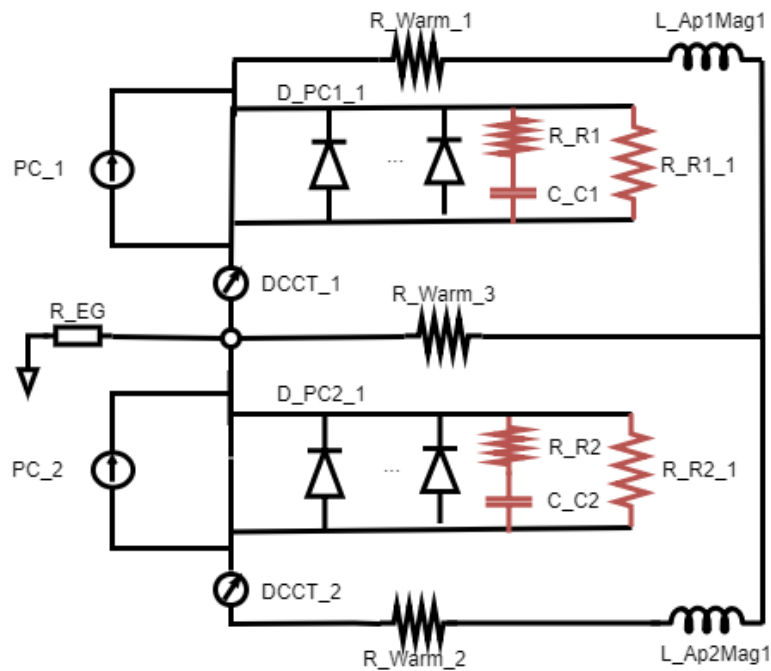
FIGURE 4.3: Schematic of the IPQ circuit with the highlighted parasitic components.

4.3 IPQ circuit model validation

Once all the model has been generated, simulations against tests were performed to demonstrate the correct behaviour of the circuits.

The goal of the validation procedure of the IPQ circuits models is to reproduce the electrical signals measured during the LHC HWC.

Each test performed in the circuit was executed following the *"Test procedure for the individually 4-6 kA quadrupole circuits"* [58]. The different powering cycles performed during the LHC HWC are shown in Fig. 4.4. For the validation of the pure electrical circuit, only the SPA tests were used. The SPAs are provoked to check the functionality of the power converter. During the SPA the power converters are switched-off, then the current in the circuit starts to decay slowly, in about 10 s.

To analyze the circuit model behaviour only the **"PNO"** tests were selected. It is possible to divide the PNO tests in two different categories: (i) **"PNO.C3"**, where the tests are performed at nominal current (or close) in both apertures of the magnet, and (ii) **"PNO.C4"**, where the tests are performed with two different currents in the two magnet apertures. During the tests, the protection of the magnet is guaranteed by the quench heaters in case of unexpected events.
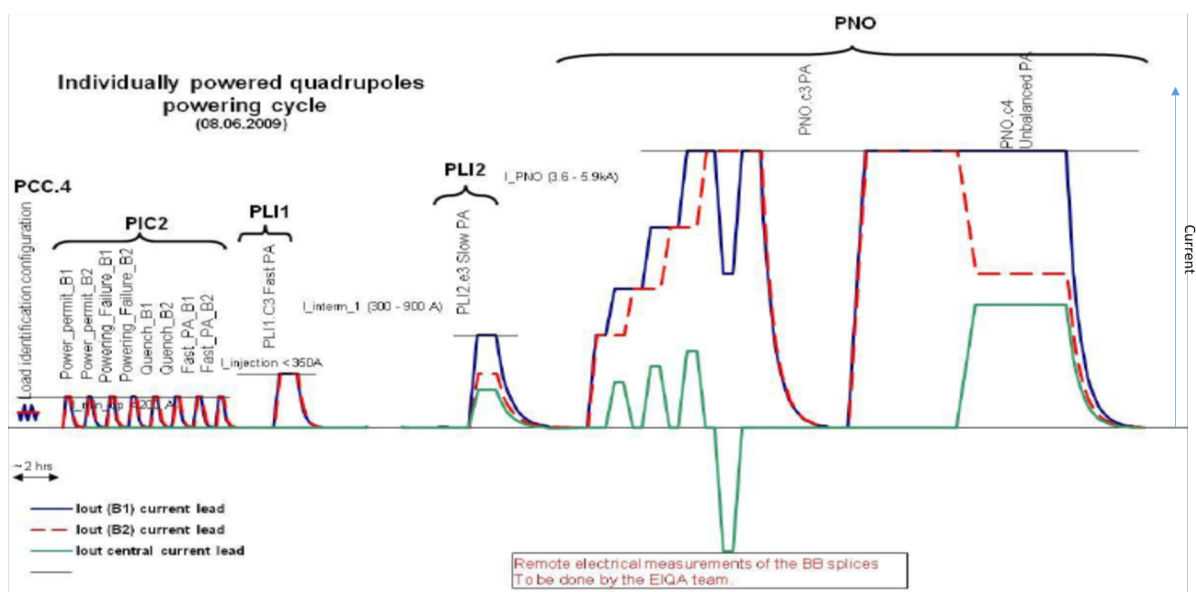
FIGURE 4.4: Powering cycles for the IPQ circuits [58].

In Fig. 4.5 the validation of four different IPQ circuits is shown; the current and the voltage on the left and right side, respectively. The model of the circuits has been proved at different conditions of nominal current, type of magnet, and temperature in order to cover all the cases. In the plots of the current versus time (i.e., left of Fig. 4.5), it is possible to observe the good agreement of the circuits during the current decay after the switch-off of the power converter, that arrives at 200 s and 800 s for RQ5.L8 (Fig. 4.5 a.), RQ8.L1 (Fig. 4.5 b.), RQ9.R2 (Fig. 4.5 d.), and RQ4.L1 (Fig. 4.5 c.), respectively. The good agreement between the circuit model and the experimental data implies a correct setting of the parameters in the circuit model, as well as the self inductances of the magnets. While, from the plots of the voltage versus time (i.e., right of Fig. 4.5) it is possible to appreciate the good agreement between the circuit model and the experimental data after the switch-off of the power converters. In conclusion, the electrical circuits model can be considered validated.
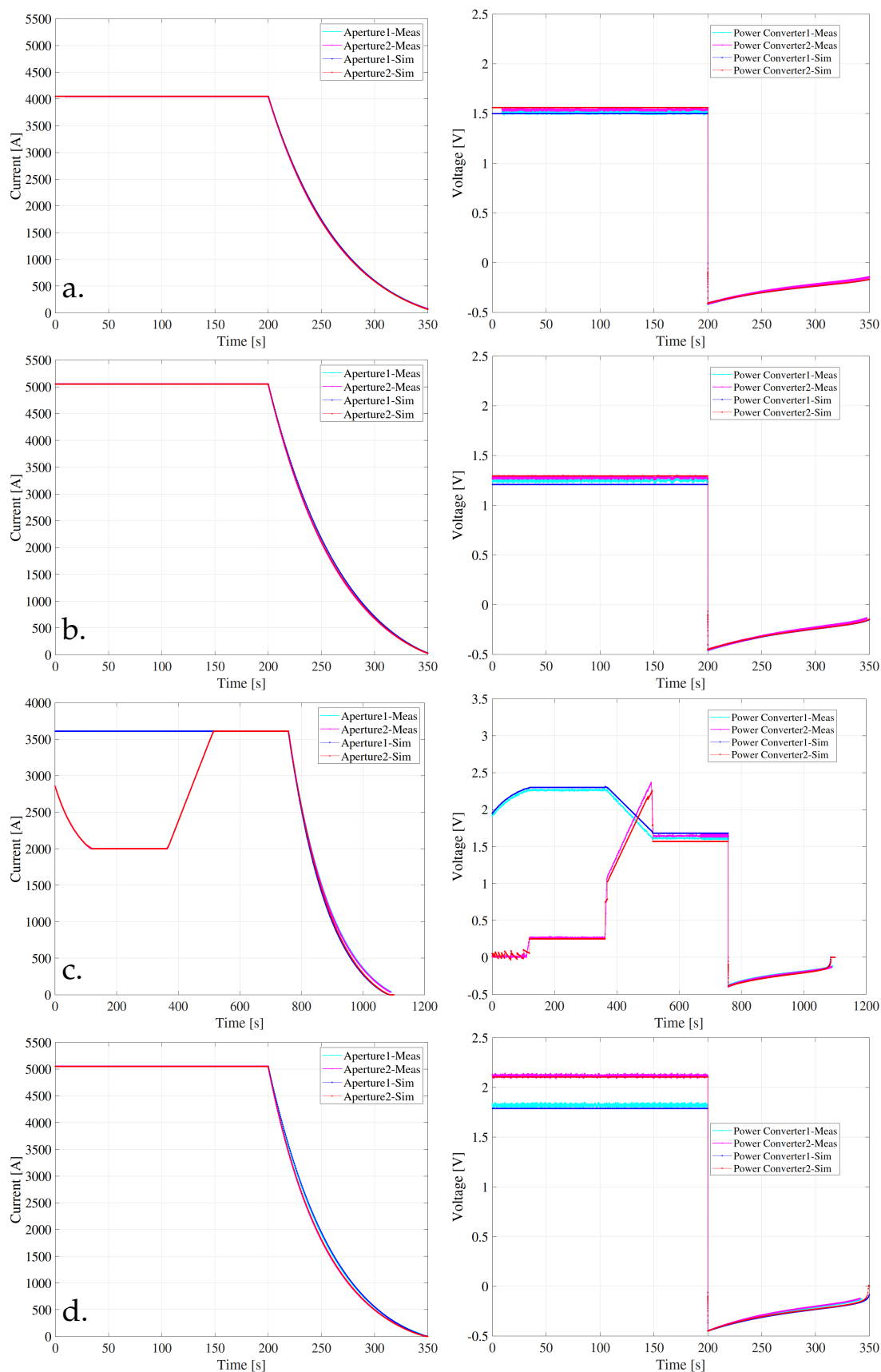
FIGURE 4.5: Validation of four different IPQ circuits. Measured and simulated DDCT current vs time and measured and simulated voltage across the power converter vs time. a. RQ5.L8 (2xMQM magnets at 4.5 K and 4.1 kA). b. RQ8.L1 (MQML magnet at 1.9 K and 5 kA). c. RQ4.L1 (MQY magnet at 4.5 K and 3.6 kA). d. RQ9.R2 (MQM+MQMC magnets at 1.9 K and 5 kA).

5 Simulation of electro-thermal transients in IPQ magnets

As described in chapter 2, in the matching section a non-symmetric magnet layout is required to compensate the shift of the collision point. The LHC matching sections are built with individually powered superconducting Nb-Ti quadrupole magnets, of the types MQM and MQY cooled at 1.9 K and 4.5 K. No additional correctors are required when these types of magnets are used, but the number of magnets and their parameters are specific for each insertion.
In the next paragraphs the generation and the validation of the MQM and MQY magnets will be described.

5.1 MQY Validation

The validation of the MQY magnet model was assessed comparing the simulations, performed with the STEAM-LEDET tool, and the experimental tests [59] carried out in 2015 at 1.9 K at the CERN magnet test facility (SM18) [60]. The experimental tests, shown in Tab. 5.1, were performed powering only one magnet aperture. During the tests three different protection systems were used: (i) Coupling-Loss Induced Quench (CLIQ), (ii) Quench Heater (QH), and Energy Extraction (EE) (detailed described in Section 1.6). The tests used to validated the model were accomplished with the aim of better understanding the effect of each protection, on a full-scale magnet, under different operating conditions [59]. During the tests, the trigger of the protections systems is $t = 0 \ s$ (t_0), but the CLIQ and the QHs start with a delay, 0.5 ms and 4 ms, respectively. Such delays are caused by the triggering time of the systems. Furthermore, the EE system is triggered with a delay that depends on the operating current, which was selected to guarantee the magnet protection even in case of malfunctioning of one of the other systems.
When a superconducting magnet quenches, the normal conductive zone propagates, increasing the resistance that forces the magnet current to decay, dissipating the stored energy. To reduce hot-spot temperature and peak voltages most of the coil needs to be quickly transferred to the normal conductive state. An example of a quench starting in one of the turns of the MQY magnet is shown in Fig. 5.1. The plot shows the effects

of an unprotected quench forced in the magnet and the consequent thermal diffusion between the closer turns. This case is unexpected on the LHC machine also in case of failure of the protection, because the redundancy of the protection systems is in place.
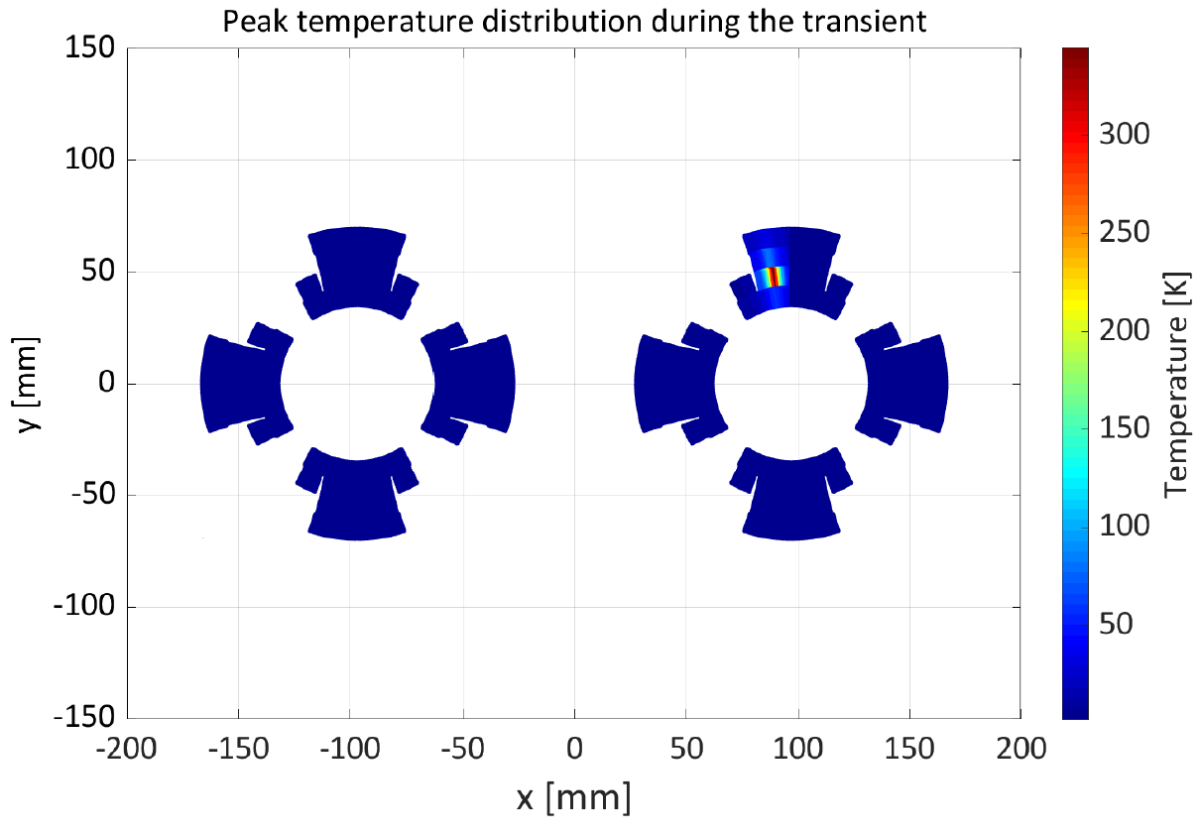
FIGURE 5.1: Temperature distribution in case of a forced quench in an unprotected MQY magnet.

TABLE 5.1: Overview of the test parameters used during the test campaign in SM18.

Test	Current [A]	R_{EE} [mΩ]	EE Delay [s]	C_{CLIQ} [mF]	V_{CLIQ} [V]	CLIQ Delay [s]	C_{QH} [mF]	V_{QH} [V]	QH Delay [s]
					SM18 tests overview				
				Delayed Energy Extraction Only					
1	1000	160	0.50	-	-	-	-	-	-
				Quench Heaters and delayed Energy Extraction					
2	3000	160	0.05	-	-	-	51.2	990	0
3	2000	160	0.25	-	-	-	51.2	990	0
4	1500	160	0.50	-	-	-	51.2	990	0
5	1000	160	0.50	-	-	-	51.2	990	0
				CLIQ and delayed Energy Extraction					
6	3000	160	0.05	8.8	650	0	-	-	-
7	2000	160	0.25	8.8	650	0	-	-	-
8	1500	160	0.50	8.8	650	0	-	-	-
9	1000	160	0.50	8.8	650	0	-	-	-
10	1500	160	0.50	56.4	500	0	-	-	-
11	1000	160	0.50	56.4	500	0	-	-	-
12	1000	160	0.50	8.8	500	0	-	-	-
13	1000	160	0.50	8.8	400	0	-	-	-

5.1.1 Delayed Energy Extraction

The first test category, composed only by one test, *Test 1*, is characterized by the presence of only the EE protection system. *Test 1* is executed at 1.9 K to evaluate the magnet discharge at low current (1 kA). The EE system is activated at 0.50 s to ensure the protection. During the validation, this test was used to calculate the electrical circuit parameters of the magnet model. Using the measured magnet current and the voltage at its terminals, it is possible to evaluate the total voltage drop across the magnet as: $V_{mag} = I_{mag}(R_{circuit} + R_{crowbar}) + V_{crowbar}$, where $R_{crowbar}$ and $V_{crowbar}$ are related to the power-supply crowbar and $R_{circuit}$ is the resistance of the warm part of the circuit. The estimated values are $R_{circuit} + R_{crowbar} = 0.0023 \ \Omega$ and $V_{crowbar} = 0.7$ V. The corresponding STEAM-LEDET simulation is shown in Fig. 5.2. The measurement and the simulation are in good agreement (with a relative error less then 0.7 %), hence $R_{circuit}$, $R_{crowbar}$, and $V_{crowbar}$ are exploit for the next simulations.

5.1.2 Quench Heaters and Delayed Energy Extraction

During the test campaigns at SM18, four tests, with QHs and delayed EE, were performed at different currents levels.
As mentioned in chapter 2.1, the design protections for the MQY quadrupole is guaranteed by 8 quench heaters strips in series per aperture. The terminals of each strip are connected to a capacitor bank charged with a certain voltage. The charging voltage and the capacitance of the quench heaters during the test campaign were 990 [V] and 51.2 [mF], respectively. The capacitance and charging voltage refers to the SM18 equipment, while during the normal operation in the LHC machine the charging voltage and the capacitance are 900 [V] and 56.4 [mF], respectively.
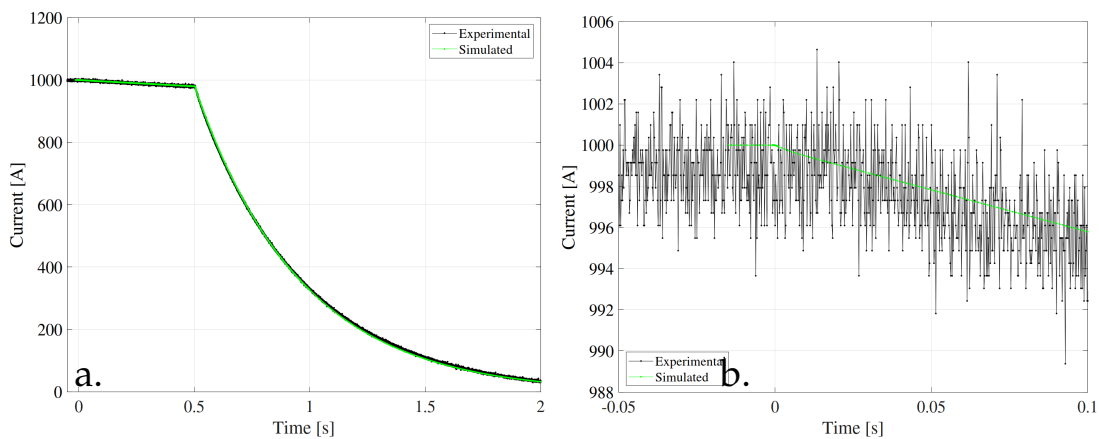
FIGURE 5.2: Delayed energy extraction only (Test 1, see Tab. 5.1). a. Measured and simulated magnet current versus time. b. Current zoom after the quench protection system starts.

Test 2

Test 2 is executed at 3 kA with QHs and delayed EE (see Table 5.1).
The first effect analyzed during the validation of the magnet model was the heat exchange between the magnet turns and the thermal sink a constant temperature equal to the helium bath temperature. STEAM-LEDET features an option for simulating the conductor cooling towards a thermal sink. In the STEAM-LEDET input file, on the *Option* sheet, it is possible to set the flag of the heat exchange to three different values.

- *flag_HeCooling*=0. The heat exchange condition is adiabatic.
- *flag_HeCooling*=1. The helium cooling is included in the simulation but only with conductive heat transfer.
- *flag_HeCooling*=2. The helium cooling include conductive and simplified convective heat transfer.

The effects of these three different options are shown in Fig. 5.3. In Fig. 5.3 is possible to see the comparison between simulated and experimental resistance. The coil resistance is not measured directly, but it is calculated from the measured voltage and current.

$$R = \frac{U_{mag} - L\frac{dI_{mag}}{dt}}{I_{mag}} \tag{5.1}$$

where U_{mag} [V] is the voltage measured across the magnet, I_{mag} [A] is the measured current in the magnet, and L [H] is the magnet self-inductance (dependent on the current). Voltage and current measurements introduce peaks in the resistance plots caused by the noise in the measurements.
The effects of the different cooling conditions are more visible in Fig. 5.3 c after the first 20 ms, while the effects are negligible on the current discharge. The *flag_HeCooling*= 2, i.e. for conductive and simplified convective helium heat transfer, is maintained for all the simulations.

A second parameter that can influence the thermal transient in a superconducting magnet is the quantity of helium inside the insulated cable cross-section. The MQY magnet has a Nb-Ti not impregnated cables, therefore, when the magnet is immersed in liquid helium, a quantity of it can permeates the cable cross-section filling the voids between the strands. Different quantities of helium inside the cable cross-section can influence the quench time due to the different volumetric heat capacity of the materials at 1.9 [K], $7\cdot10^5$ [J/Km^3] and $2\cdot10^2$ [J/Km^3] for helium and kapton, respectively [45].
Knowing all the parameters of the bare cable (reported in Fig. 5.4) and the diameter of the strands (0.48 mm and 0.73 mm for the outer and the inner cable, respectively), it is possible to obtain the area of the voids inside the insulated cable cross-section. For the MQY magnet the 9.8% of the cable cross-section area is empty. The remaining area is occupied by the strands (72.7%) and by the insulation (17.5%). The voids of the cable-cross section can be filled by the infiltrated helium, by the insulation deformed due to the Lorentz forces, or partially by both, as introduced in section 3.2.2. The effect
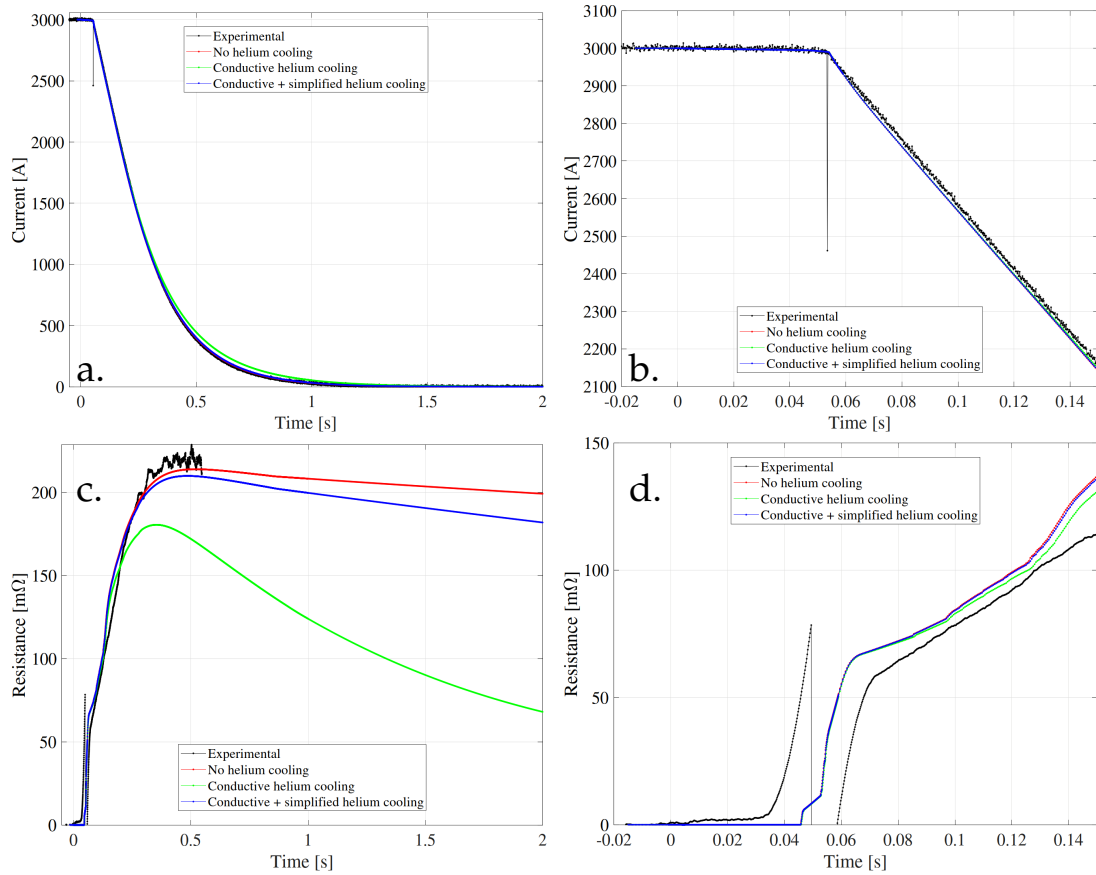
FIGURE 5.3: Simulation and measurement for different settings of the
LEDET helium cooling assumptions. a. Magnet current versus time.
b. Zoom in the magnet current.   c. Magnet resistance versus time.
d. Zoom in the magnet resistance.

of different fraction of helium inside the cable cross-section is shown in Fig. 5.5. More
details about the absolute and relative error between simulations and measurements
are summarized in Tab. 5.2. Where RMSE is the Root Mean Square Error, |E| is the
absolute error, and E_r is the relative error. E_r is calculated as I*sim*-I*meas*/I*meas*, where
I*sim* is the simulated magnet current and I*meas* the measured current.

The best agreement between simulation and measurement is achieves with the 7%
of the cable cross-section filled by the helium (5/7 of the voids). For the other two
cases (5% of helium and no helium inside the cable cross-section) the quench is
induced sooner than the experiment, (10 ms, and 30 ms respectively), while, in the
case where all the voids are filled by the helium the quench arrive few milliseconds
after the measurement. Moreover, the simulation with 7% of helium inside the cable
cross-section is to be considered better than the other because the absolute error
(Fig. 5.5 a) is lower in the first part of the current discharge.

Another parameter related with the heat exchange during the quench transient is
the *fScaleContactAreaQH*. It introduces the possibility to set the contact area between
the QH strips and the conductors in order to simulate the diffusion of the heat along
the longitudinal axis. Once the QHs are triggered, the heat does not propagate
homogeneously, but it start to spread from the heating stations (introduced in
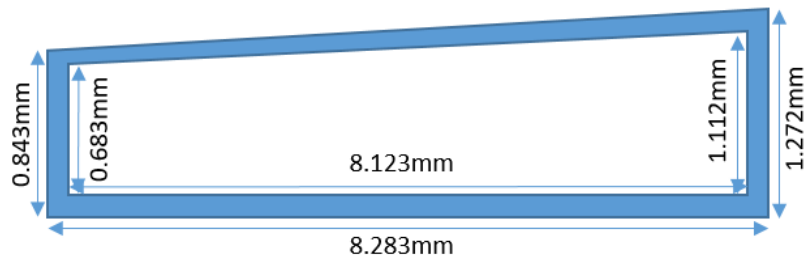
FIGURE 5.4: Schematic design and size of the MQY cable bare.
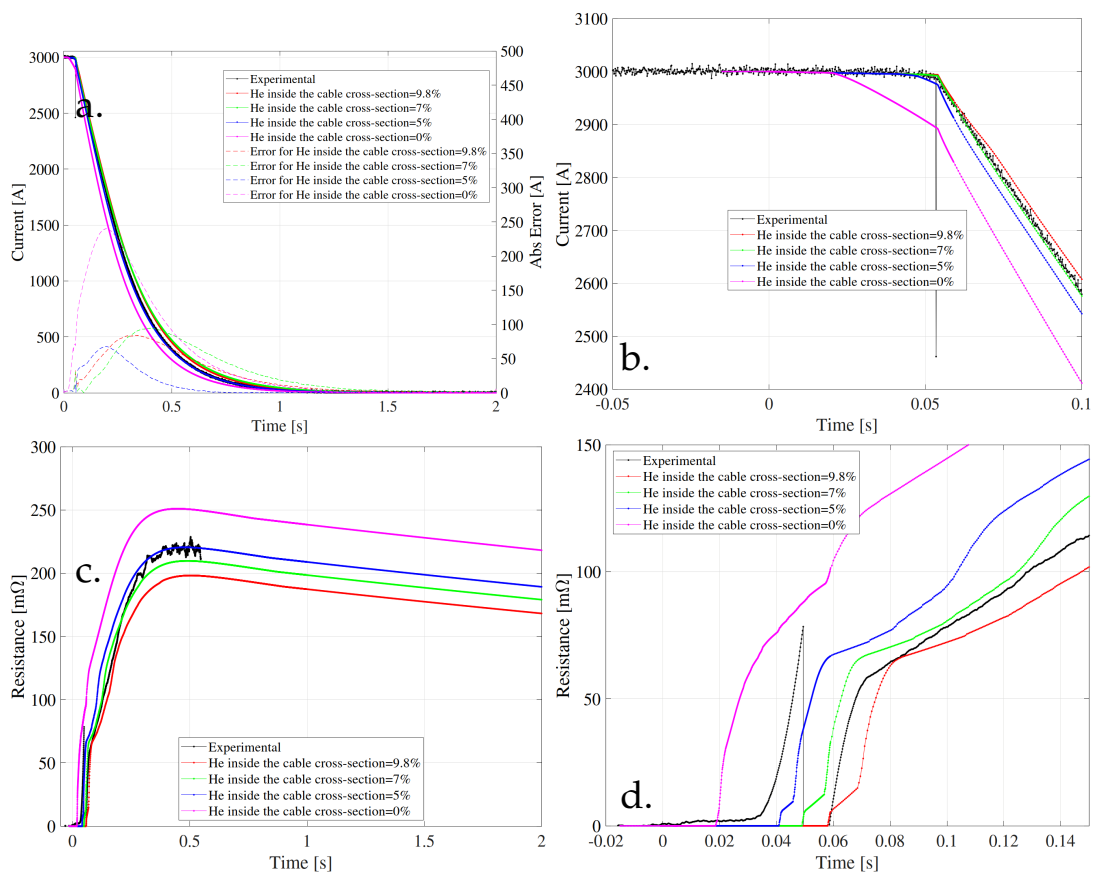
FIGURE 5.5: Simulations and measurement for different fractions of helium inside the insulated cable cross-section. a. Magnet current versus time. b. Zoom in the magnet current. c. Magnet resistance versus time. d. Zoom in the magnet resistance.

TABLE 5.2: Absolute and relative error on the magnet current for the simulations with different quantity of helium inside the cable cross-section.

	RMSE [A]	Max $|E|$ [A]	$<E_r>$ [%]	Max E_r [%]
He=9.8%	47.7	84.1	6.4	12.1
He=7%	13.8	30.5	0.9	3.8
He=5%	21.4	67.8	2.8	4.3
He=0%	107.4	240.0	12.1	21.0
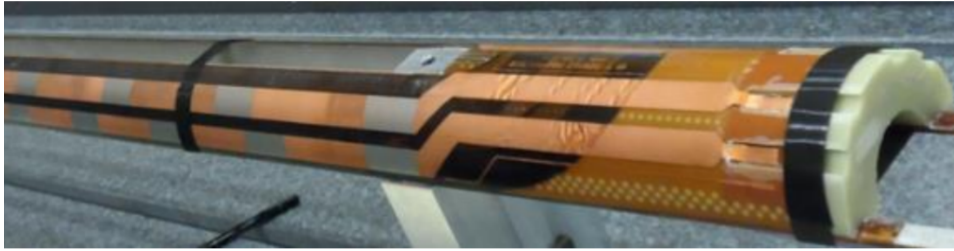
FIGURE 5.6: Photo of the HL-LHC quench heaters. The fractions of stainless steel (heating station) and copper are well identifiable [61].
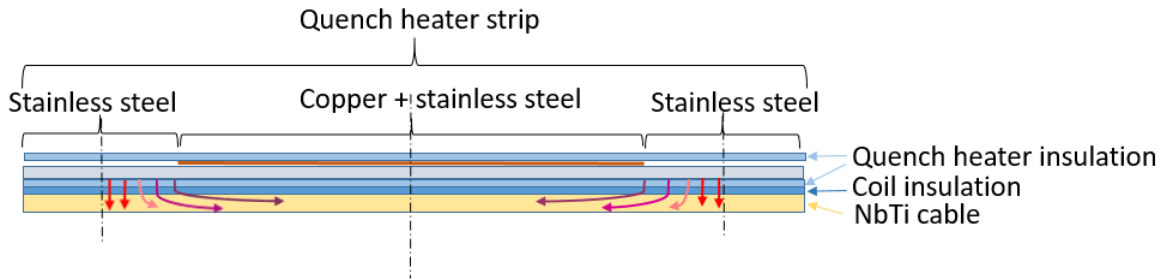
FIGURE 5.7: Simplified representation of the thermal layout along the length of the conductor. The heat flux flow from the quench heater heating stations to the conductors. Different colors of the arrows represent different cases of heat propagation.

section 1.6 and shown in Fig. 5.6). Once the strip starts to heat up, the heat flux moves from the QHs to the conductors flowing by the heating stations, as shown in Fig. 5.7. The different colors of the arrows in Fig. 5.7, represent different cases of heat propagation, which is strongly related to the temperature and the magnet current [62, 48].

To understand the impact of the *fScaleContactAreaQH* parameter on the simulations, four different values of it are taken into account (they are summarized in Tab. 5.3 where *fScaleContactAreaQH IN* and *fScaleContactAreaQH OUT* represent the fraction of the stainless steel in the QHs strips on the inner and outer layers, respectively):

- Case 1 (Min): In this case the heat propagation from the QH strips to the conductors is supposed very quick and there is not heat propagation along the cable between the two closer heating stations. It represents the minimum value

Scaling factor of the contact Area of the QH		
	fScaleContactAreaQH IN	fScaleContactAreaQH OUT
Min	0.40	0.28
Av between Av and Min	(0.4+Av)/2	(0.28+Av)/2
Average	(0.4+1)/2	(0.28+1)/2
Max	1	1

TABLE 5.3: Different values of *fScaleContactAreaQH* used for the validation during the simulations.

TABLE 5.4: Absolute and relative error on the magnet current for the simulations with different scaling factor of the contact area between the QHs and the conductors.

	RMSE [A]	Max |E| [A]	$<E_r>$ [%]	Max E_r [%]
fScQH=Min	8.1	32.6	0.3	1.1
fScQH=Av betw Av and Min	5.9	30.3	0.2	1.0
fScQH=Av	7.2	27.9	0.3	1.1
fScQH=Max	12.0	51.3	0.4	1.8

of heat propagation in the cable. Case 1 is represented by the red arrows in Fig. 5.7.

- Case 2 (Average between the Average and the Minimum): The scaling factor of the contact area was taken as the average between the average (between max and min) and the minimum value (case 1). This is a reasonable assumption because the heat flux, that through to the heating stations, is in function of the temperature and the external current [62], therefore, it can spread around the heating station to the closer ones. Case 2 is represented by the red and pink arrows in Fig. 5.7, and it presented the best agreement between simulations and measurements (see Tab. 5.4), i.e. these values of *fScaleContactAreaQH IN* and *fScaleContactAreaQH OUT* are used in the whole validation process.
- Case 3 (Average): Is the average between the minimum value of the scaling factor (case 1) and the maximum one (case 4). Case 3 is represented by the red, pink and soft purple arrows in Fig. 5.7.
- Case 4 (Max): Represent the maximum value of the scaling factor. In this case is supposed that the heat spread slowly in the cable, so it has the time to expand along the longitudinal length between two closer heating stations. Case 4 is represented by all the arrows in Fig. 5.7.

The simulations with different values of the *fScaleContactAreaQH* are shown in Fig. 5.8.

The last parameter to set up for the validation of the MQY model at 3 kA is the Residual Resistivity Ratio (RRR). The range of RRR chosen for the model validation goes from 170 to 220 (according to the magnet description, section 2.1). Different RRR values can affect the transient of the resistance after the quench as shown in Fig. 5.9. Due to the small errors (reported in Tab. 5.5), and to be consistent with the validation
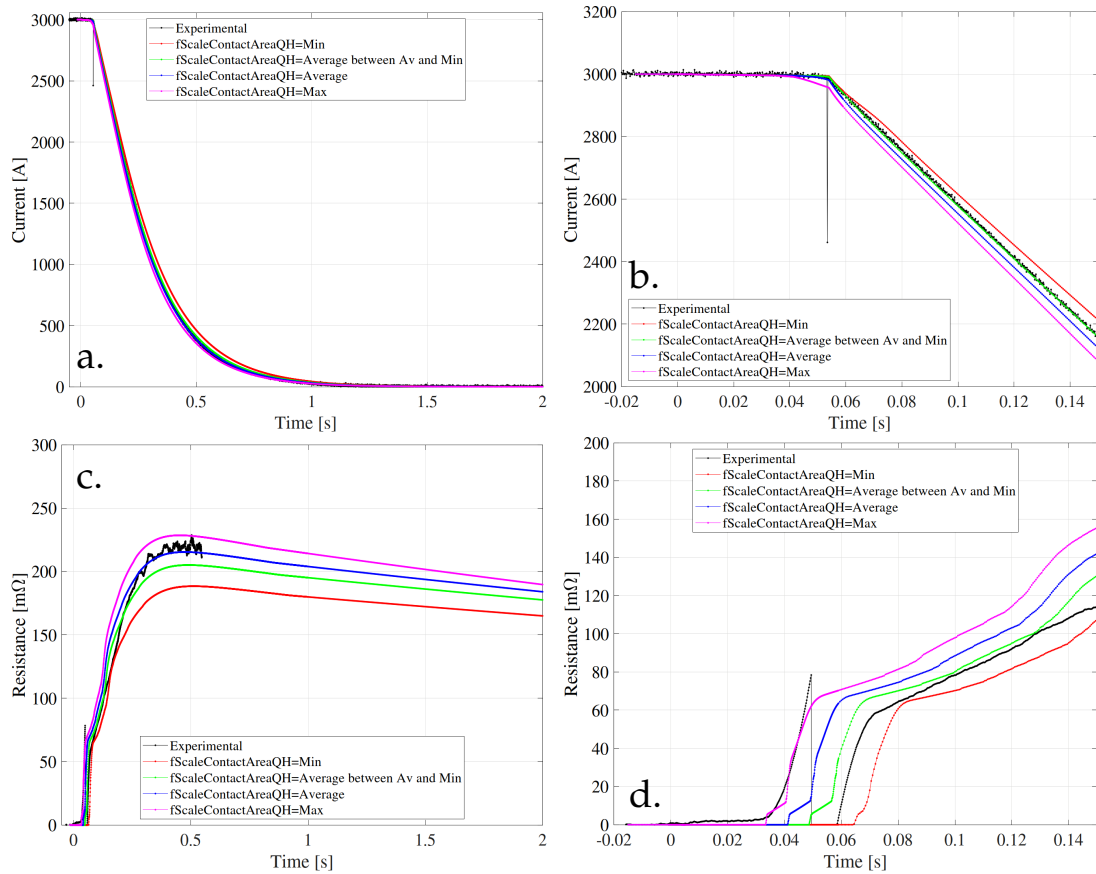
FIGURE 5.8: Simulations and measurements for different *fScaleContactAreaQH*. *fScaleContactAreaQH=Min*, represents the minimum spread of the heat flux on the cables (case1).
fScaleContactAreaQH=Average between the Average and the Min, represents an average of the scaling factor of the QH strip contact area between the minimum and the average value (case2).
fScaleContactAreaQH=Average, represents the mathematical average between the maximum and minimum values of the scaling factor of the contact area of the QH strip (case3).
fScaleContactAreaQH=Max, represents the maximum spread of the heat flux on the cables (case4).
a. Magnet current versus time. b. Zoom in the magnet current. c. Magnet resistance versus time. d. Zoom in the magnet resistance.
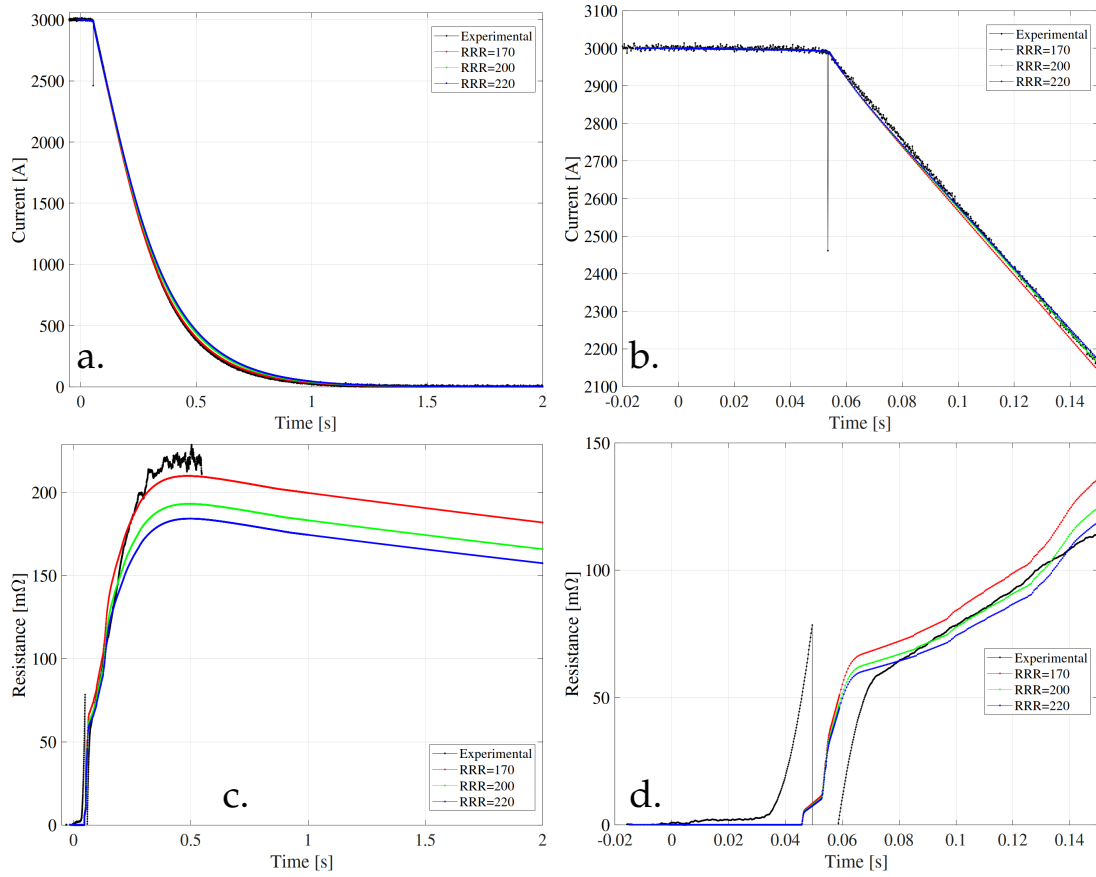
FIGURE 5.9: Simulations and measurement for different Residual Resistivity Ratio. a. Magnet current versus time. b. Zoom in the magnet current. c. Magnet resistance versus time. d. Zoom in the magnet resistance.

TABLE 5.5: Absolute and relative error on the magnet current for the simulations with different RRR.

	RMSE [A]	Max |E| [A]	$<E_r>$ [%]	Max E_r [%]
RRR=170	12.1	28.2	0.7	1.8
RRR=200	30.0	55.3	2.1	8.3
RRR=220	43.4	78.4	3.2	12.0

at different current levels, a value of RRR=170 was chosen for the validation and it has been used for all the next simulations.

The validation of *Test 2*, with all the parameters found until now, is shown in Fig. 5.10.
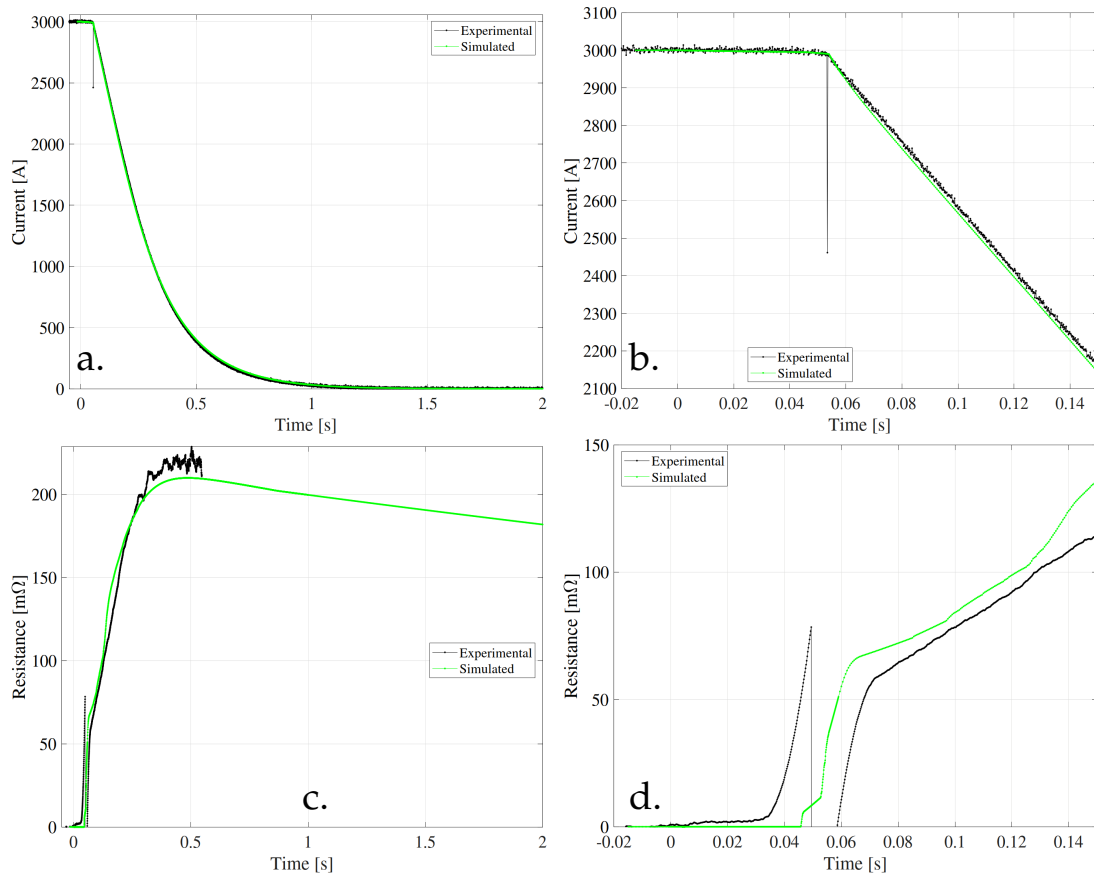
FIGURE 5.10: Quench Heaters and Delayed Energy Extraction (Test 2, see
Tab. 5.1). a. Magnet current versus time. b. Zoom in the magnet current.
c. Magnet resistance versus time. d. Zoom in the magnet resistance.

Test 3

Test 3 is at 2 kA with QHs and delayed EE (see Tab. 5.1). The current of *Test 3* is
lower than the nominal one. Therefore, during the transient, the heat does not spread
immediately for the entire magnetic length, but it move between the turns due to
thermal diffusion across the insulation layers between turns.
Once the QHs are triggered in the 2D model, the heat starts to spread radially from the
heating stations to the turns. While, with the updated model, from 2D to 2D+1D (see
section 3.2.3), also the longitudinally heat diffusion through the copper of the strands
has been approximated. The initial longitudinal length of the quenched conductor,
in a MQY magnet, is equal to 0.97 m; this corresponds to the length covered by the
QHs heating stations. From them the heat spreads in the longitudinal direction with
a certain quench velocity propagation that introduces in the simulation a Δt.
The quench velocity propagation is a parameter influenced by different factors, as
the current level, the magnetic field, the magnet temperature, etc [49]. An additional
scaling factor is needed at low current because the effect of helium cooling is more
significant and the adiabatic approximation is less accurate. To better analyze the
effect of the scaling factor, simulations with different scaling factors on the quench

TABLE 5.6: Absolute and relative error for the simulations with different scaling factor of the quench velocity propagation.

	RMSE [A]	Max $|E|$ [A]	$<E_r>$ [%]	Max E_r [%]
sF=1	22.8	68.8	3.7	7.5
sF=0.9	22.5	66.8	3.6	7.5
sF=0.8	22.3	65.6	3.5	7.5
sF=0.7	22.1	64.0	3.4	7.4
sF=0.5	12.6	42.4	2.7	7.1
sF=0.3	19.8	48.6	2.7	7.0
sF=0.25	19.0	47.3	2.0	6.7
sF=0.2	17.7	45.9	2.0	6.6
sF=0.15	15.8	43.3	1.0	4.1
sF=0.1	16.0	45.4	1.5	5.4
sF=0.05	22.0	92.8	4.1	8.0
sF=0.0	85.2	208.9	10.1	30.3

velocity propagation are shown in Fig. 5.11. Once the scaling factor is equal to zero, the quench velocity propagation is zero, i.e. the heat don't spread around remaining on the quenched fraction of the turns in contact with the heating stations. On the contrary, if the scaling factor is equal to 1 it is possible to observe that the current is discharged too quickly respect to the experiment; in both cases, the simulations are not in agreement with the measurements. The simulation with the better agreement (see Tab. 5.6) is the one with a scaling factor equal to 0.15 and it is shown in Fig. 5.12.
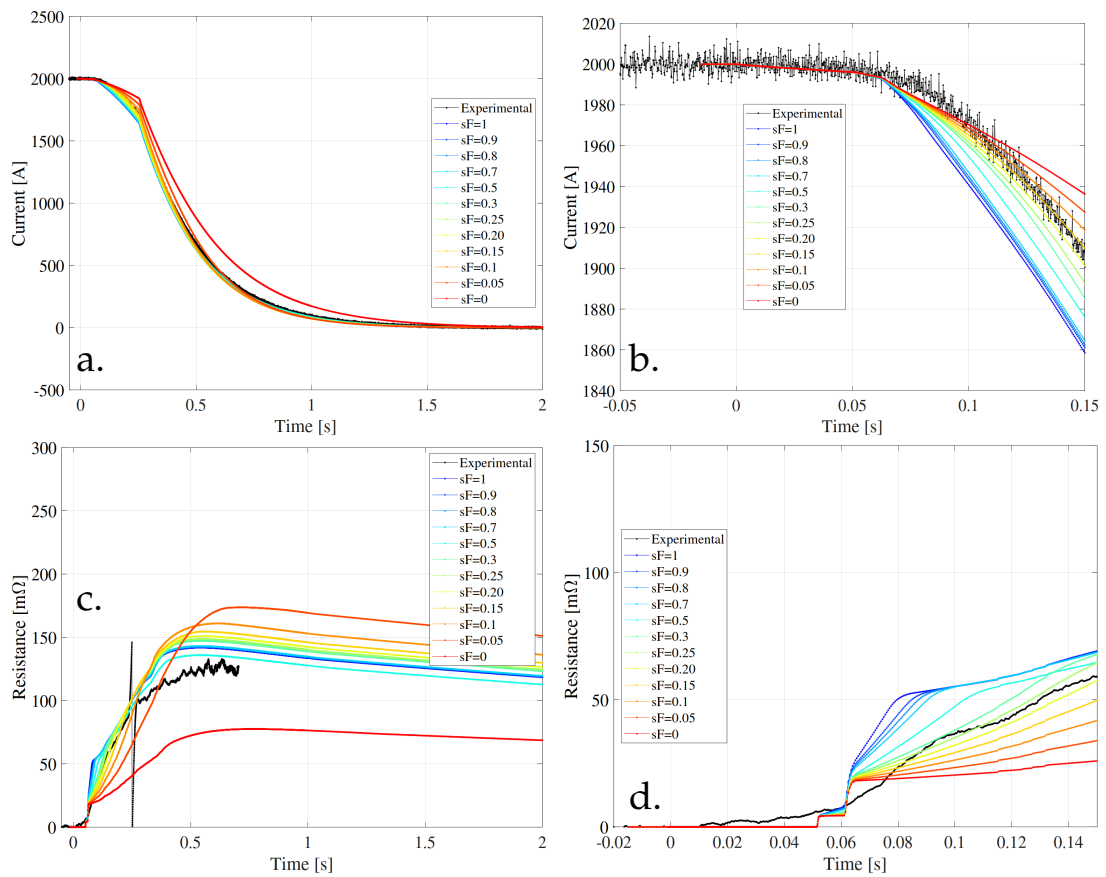
FIGURE 5.11: Experimental curve and simulations for different scaling factor values. a. Magnet current versus time. b. Zoom in the magnet current. c. Magnet resistance versus time. d. Zoom in magnet resistance.
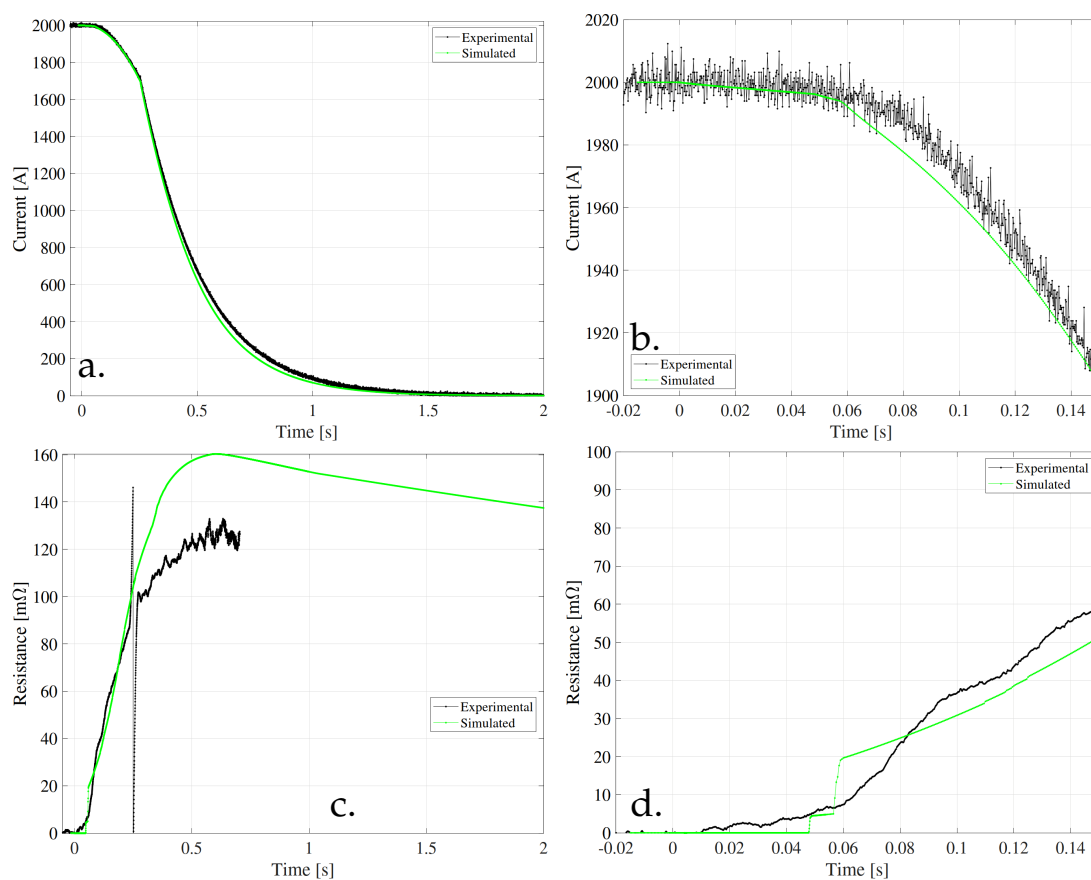
FIGURE 5.12: Quench Heaters and Delayed Energy Extraction (Test 3, see Tab. 5.1). a. Magnet current versus time. b. Zoom in the magnet current. c. Magnet resistance versus time. d. Zoom in magnet resistance.

Test 4 and Test 5

The validation of *Test 4* and *Test 5*, was done with the parameter found until now during the MQY validation. The scaling factor of the quench velocity propagation was change due to the current level (1.5 kA and 1 kA for *Test 4* and *Test 5*, respectively, see Tab. 5.1). The scaling factors that best approximate the experimental curves are 0.1 and 0.07 for *Test 4* and *Test 5*, respectively. The simulations of the two tests, are shown in Fig. 5.13 (*Test 4*), and Fig. 5.14 (*Test 5*), while the errors are summarized in Tab. 5.7.
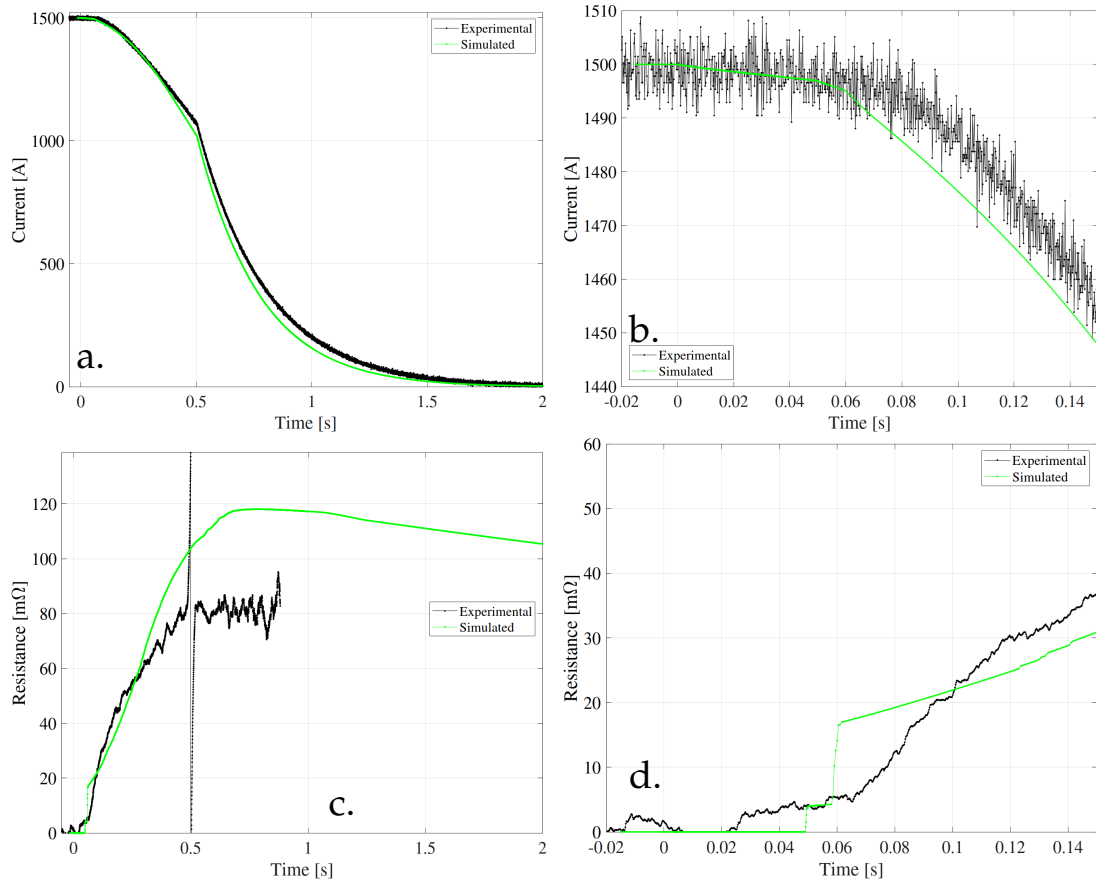
FIGURE 5.13: Quench Heaters and Delayed Energy Extraction (Test 4, see Tab. 5.1). a. Magnet current versus time. b. Zoom in the magnet current. c. Magnet resistance versus time. d. Zoom in magnet resistance.

TABLE 5.7: Absolute and relative error on the magnet current for test 4 and test 5.

	RMSE [A]	Max |E| [A]	$<E_r>$ [%]	Max E_r [%]
Test 4	30.0	60.0	0.4	1.9
Test 5	7.1	35.7	0.5	0.9
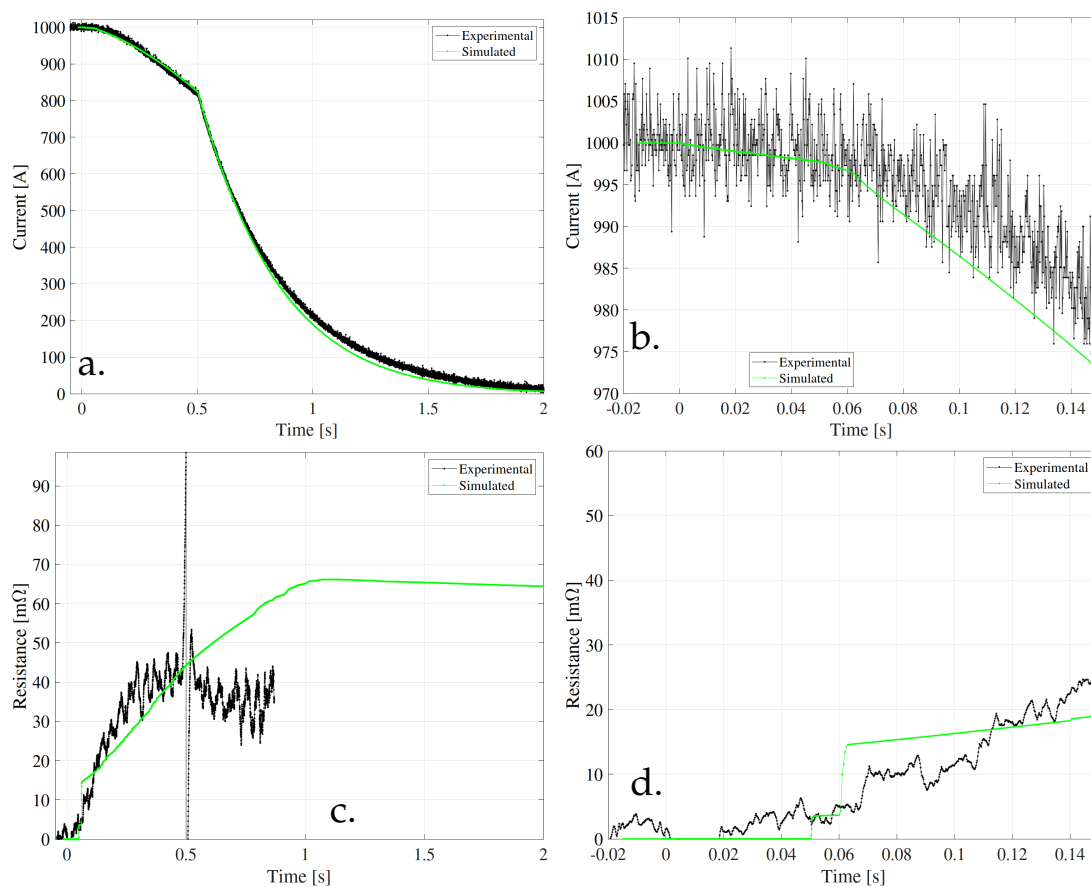
FIGURE 5.14: Quench Heaters and Delayed Energy Extraction (Test 5, see Tab. 5.1). a. Magnet current versus time. b. Zoom in the magnet current. c. Magnet resistance versus time. d. Zoom in magnet resistance.

The different scaling factors chosen at different current levels are shown in Fig. 5.15. The effect of the scaling factor is negligible at nominal current, while it has a significant impact at low currents regime (from 2000 A).
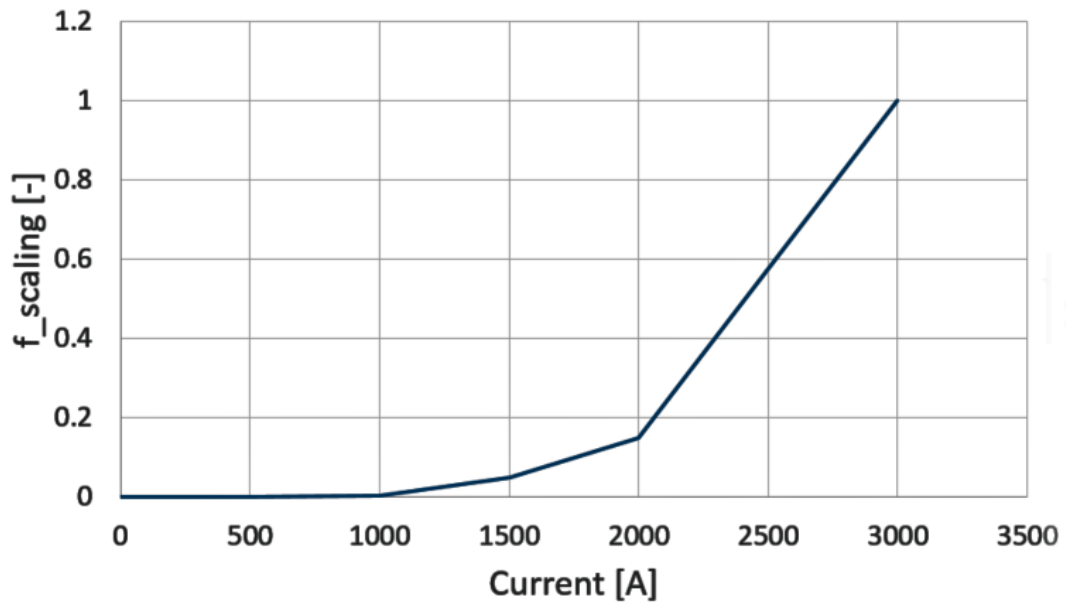
FIGURE 5.15: Trend of the scaling factor. At 3 kA the effect of the scaling factor is negligible, while it have a big impact at low currents.

5.1.3 CLIQ and Delayed Energy Extraction

As specified in section 2.1, the MQY quench protection relies on QHs. During the test campaign at SM18 in 2015, CLIQ units and EE have been added to test the protection in a full-scale magnet.

Two different CLIQ units were used during the tests. They were characterized by different capacitance, charging voltage of the capacitor banks, and hence stored energy, as summarized in Tab. 5.8.

The electrical scheme of the MQY magnet with the CLIQ protection is shown in Fig. 5.16 [59]. The CLIQ unit is connected between one side of one aperture and its middle point. All the tests were performed powering only one aperture of the magnet. Test 6, Test 7, Test 8, and Test 9 are executed with the unit CLIQ-1 at different current levels.

TABLE 5.8: Main parameters of the CLIQ units

Name	Capacitance [mF]	Charging Voltage [V]	Energy [kJ]
CLIQ-1	8.8	650	1.86
CLIQ-2	56.40	500	7.05
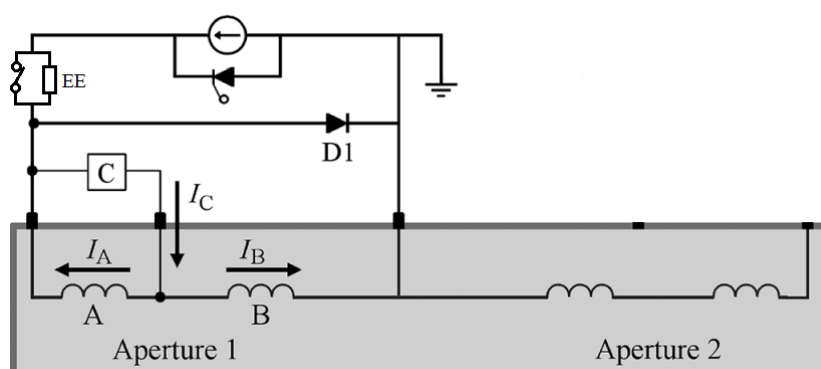
FIGURE 5.16: Schematic of the magnet test circuit including the CLIQ system protection in one aperture [59].

Test 6

The transient generated by the CLIQ protection, caused in the SC coil a varying magnetic field that introduces transient currents between the superconducting filaments of a strand, and then ohmic losses generated by the closed paths across the normal conducting matrix. Due to the multiple strands, also coupling currents through strand contact resistances are developed during the transient [19].

During the MQY validation, only the Inter-Filament Coupling Currents (IFCC) have been taken in to account. The coupling losses generated in the conductor increase its temperature and can cause the transition to the normal state during the discharge. STEAM-LEDET can offer a quantitative estimation of the coupling-loss contribution to the discharge and provide realistic information to assess and optimize the protection systems.

To better understand the effect of the IFCC on the magnet model, the effective transverse resistivity parameter f_{eff} (introduced in section 3.2.1) has been changed in a wide range. The inter-filament coupling loss generated during the transient are uniformly along the longitudinal direction. In Fig. 5.17 several simulations with different value of f_{eff} are shown. The simulation with f_{eff}=3.5, shown in Fig. 5.18, is the one with the best agreement with the measurement (see Tab. 5.9).

The parameters selected for validate the MQY magnet model during a transient with CLIQ and delayed EE are:

- Residual Resistivity Ratio = 170
- Fraction of helium inside the insulated cable cross-section = 7 %
- Effective transverse resistivity parameter = 3.5

TABLE 5.9: Absolute and relative error on the magnet current for simulations with different values of effective transverse resistivity.

	RMSE [A]	Max |E| [A]	$<E_r>$ [%]	Max E_r [%]
f_{eff}=0.5	151.9	687.3	5.8	26.1
f_{eff}=1	126.8	572.3	4.9	21.4
f_{eff}=2	74.9	371.5	2.9	14.4
f_{eff}=3	61.5	262.0	2.4	10.1
f_{eff}=3.5	54.5	192.7	2.0	7.2
f_{eff}=4	54.8	193.6	2.1	7.6
f_{eff}=5	61.8	156.0	2.3	7.6
f_{eff}=6	69.9	174.5	2.7	7.3
f_{eff}=7	77.5	191.0	3.0	7.8
f_{eff}=8	85.7	205.6	3.3	7.8
f_{eff}=9	93.9	218.9	3.6	8.2
f_{eff}=10	101.3	230.4	3.9	8.2
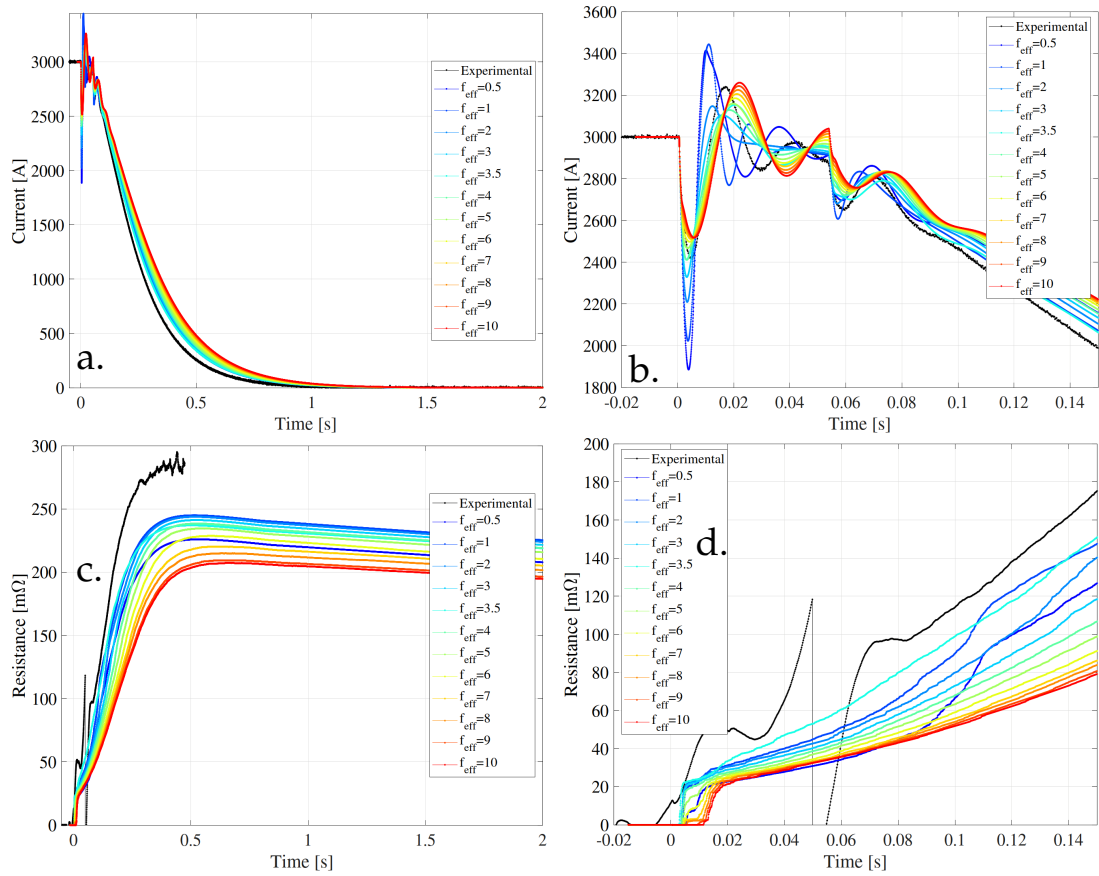
FIGURE 5.17: Experimental curve and simulations for different f_{eff} values. a. Magnet current versus time. b. Zoom in the magnet current. c. Magnet resistance versus time. d. Zoom in magnet resistance.
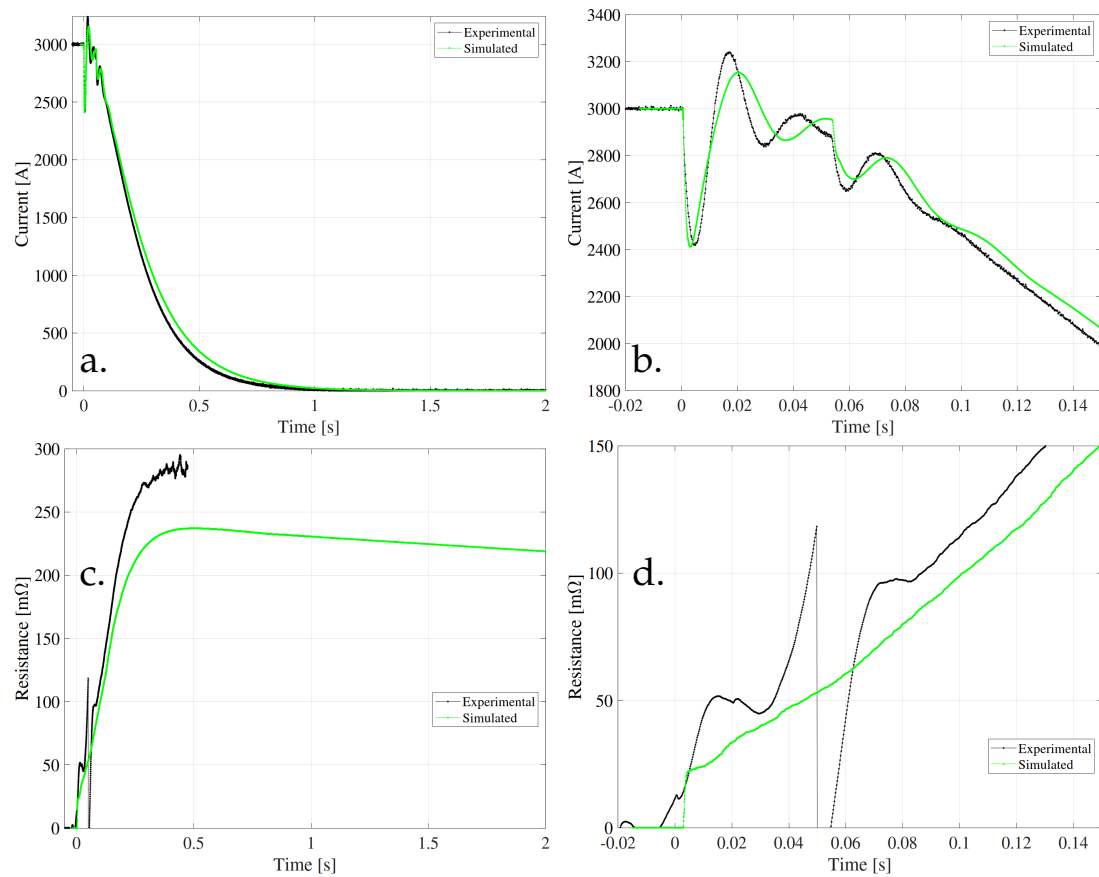
FIGURE 5.18: CLIQ and Delayed Energy Extraction (Test 6, see Tab. 5.1).
a. Magnet current versus time. b. Zoom in the magnet current. c. Magnet
resistance versus time. d. Zoom in magnet resistance.

Test 7, Test 8, and Test 9

The simulations of *Test 7*, *Test 8*, and *Test 9* (see Tab.5.1) have been done using the parameters selected until now (RRR, quantity of helium inside the insulated cable cross-section, and f_{eff}). The simulations of *Test 7*, *Test 8*, and *Test 9* are shown in Fig. 5.19, Fig. 5.20, and Fig. 5.21, respectively, while the absolute and relative error are summarized in Tab. 5.10. In all of these simulations the quench occurs slightly sooner with respect to the experiment (0.5-1 ms).
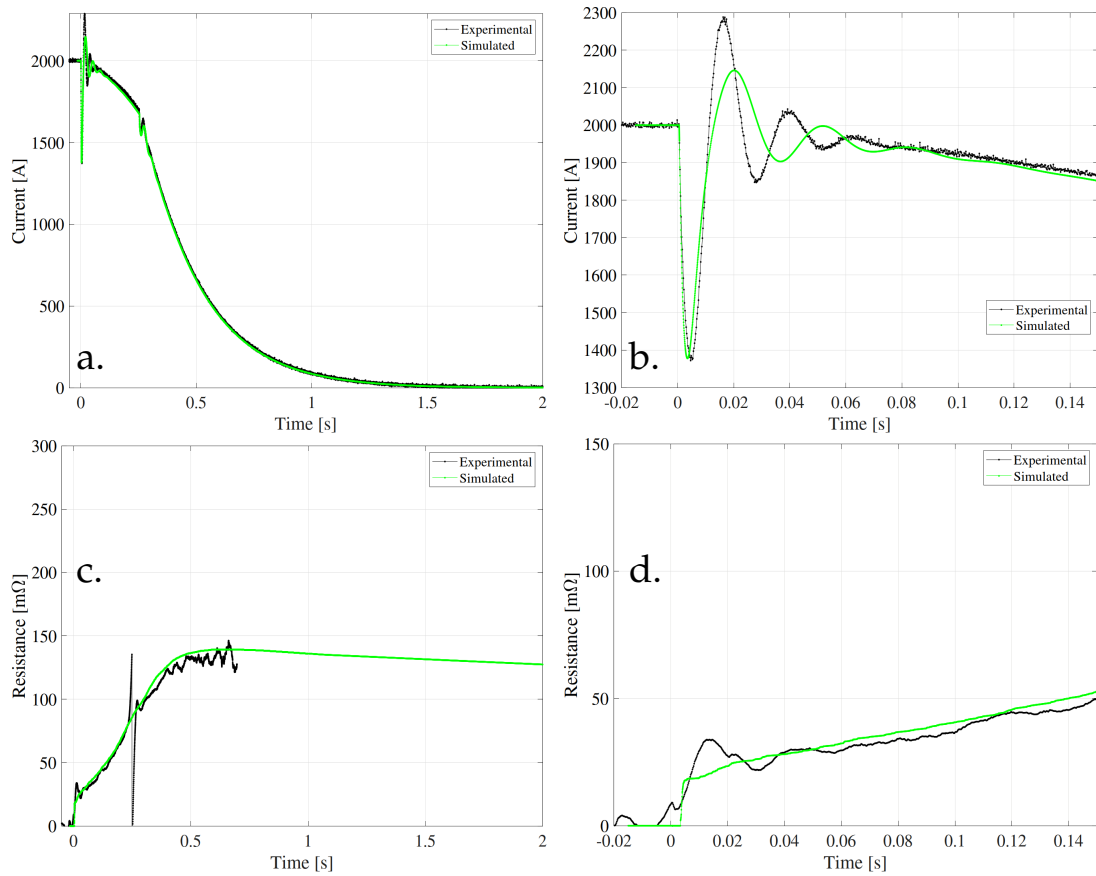
FIGURE 5.19: CLIQ and Delayed Energy Extraction (Test 7, see Tab. 5.1). a. Magnet current versus time. b. Zoom in the magnet current. c. Magnet resistance versus time. d. Zoom in magnet resistance.

TABLE 5.10: Absolute and relative error on the magnet current for Test 6, Test 7, Test 8, and Test 9.

	RMSE [A]	Max $|E|$ [A]	$<E_r>$ [%]	Max E_r [%]
Test 6	54.5	192.7	2.0	7.2
Test 7	6.9	176.8	0.6	1.3
Test 8	39.6	188.6	3.5	18.1
Test 9	32.9	215.9	2.7	22.9
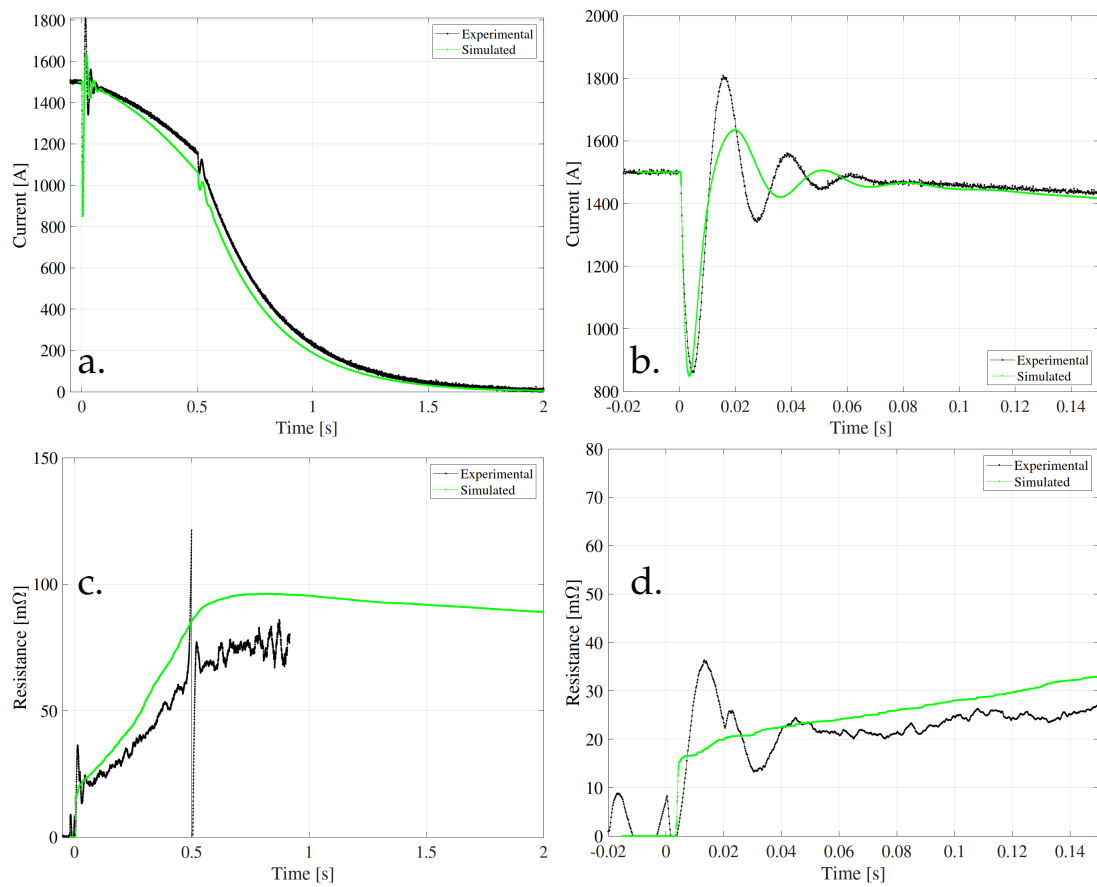
FIGURE 5.20: CLIQ and Delayed Energy Extraction (Test 8, see Tab. 5.1).
a. Magnet current versus time. b. Zoom in the magnet current. c. Magnet
resistance versus time. d. Zoom in magnet resistance.
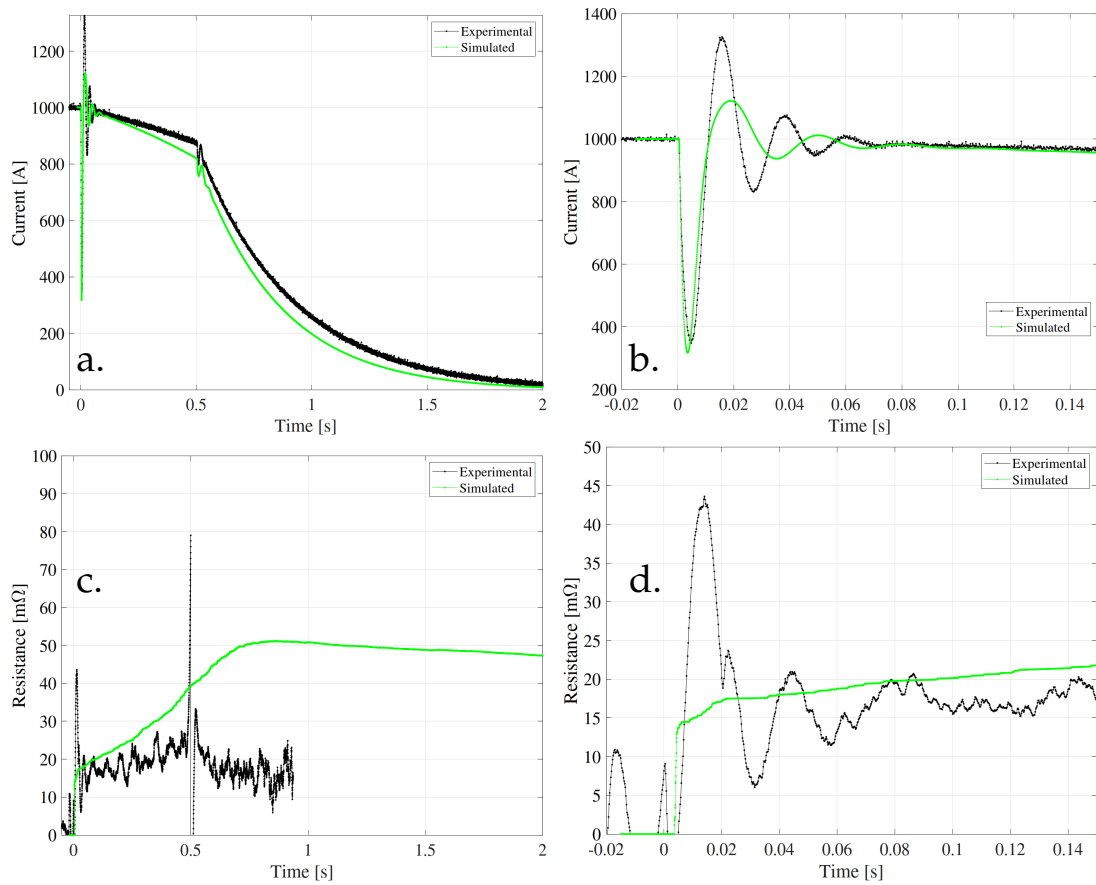
FIGURE 5.21: CLIQ and Delayed Energy Extraction (Test 9, see Tab. 5.1).
a. Magnet current versus time. b. Zoom in the magnet current. c. Magnet
resistance versus time. d. Zoom in magnet resistance.

Test 10, Test 11, Test 12, and, Test 13

Test 10 and *Test 11* were executed at different current level with the unit CLIQ-2 (see Tab. 5.8). The simulations are shown in Fig. 5.22, and Fig. 5.23, respectively. The higher-amplitude oscillations visible during the current discharge are related to the higher capacitance of the CLIQ unit.
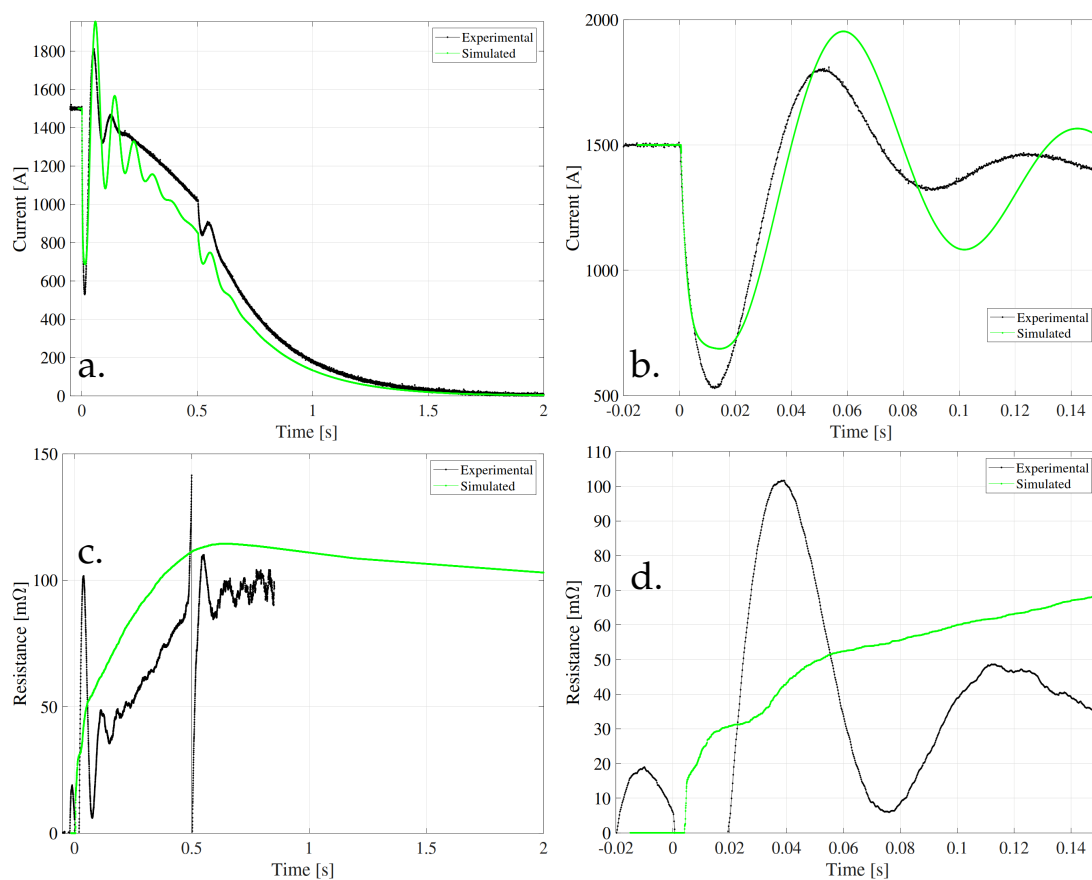
FIGURE 5.22: CLIQ and Delayed Energy Extraction (Test 10, see Tab. 5.1). a. Magnet current versus time. b. Zoom in the magnet current. c. Magnet resistance versus time. d. Zoom in magnet resistance.
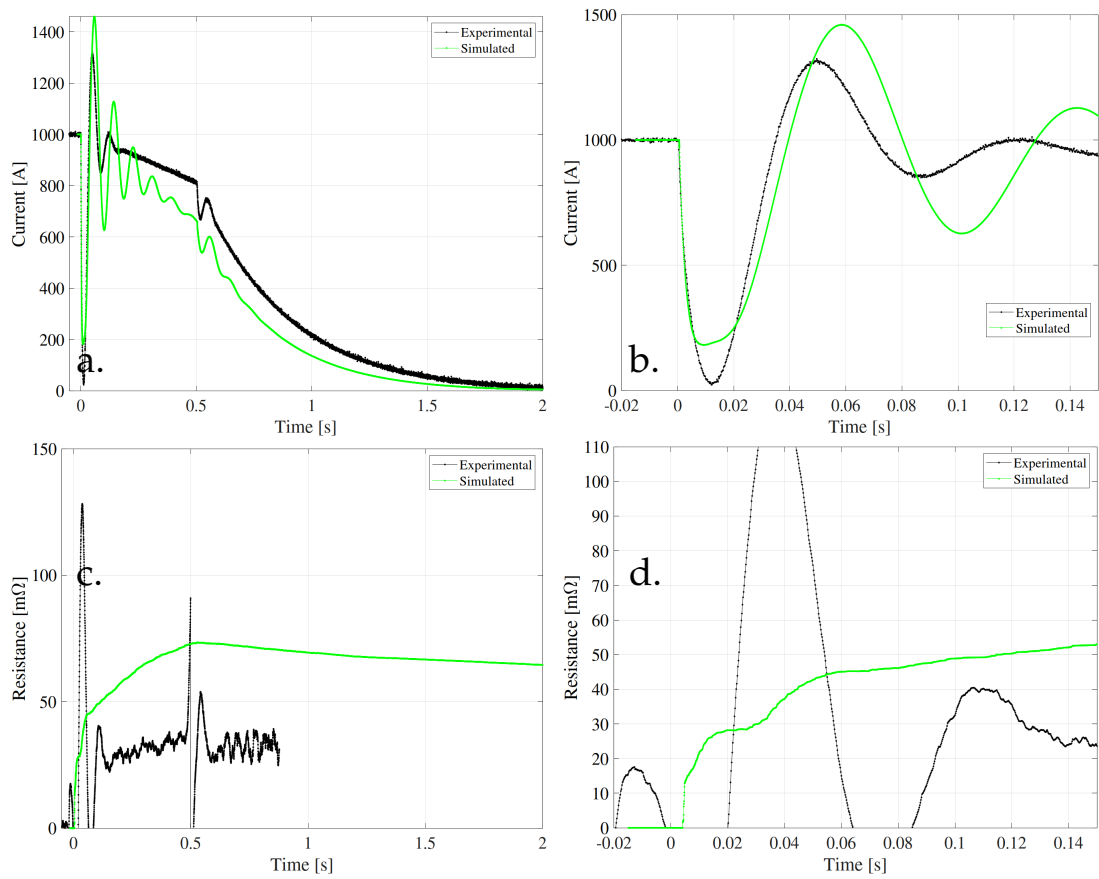
FIGURE 5.23: CLIQ and Delayed Energy Extraction (Test 11, see Tab. 5.1).
a. Magnet current versus time. b. Zoom in the magnet current. c. Magnet
resistance versus time. d. Zoom in magnet resistance.

Test 12 and *Test 13* were executed with the unit CLIQ-1 (see Tab. 5.8) at different voltages. The simulations are shown in Fig. 5.24, and Fig. 5.25 for *Test 12* and *Test 13* respectively.

Absolute and relative errors between tests and simulations executed with different CLIQ unit are reported in Tab. 5.11.
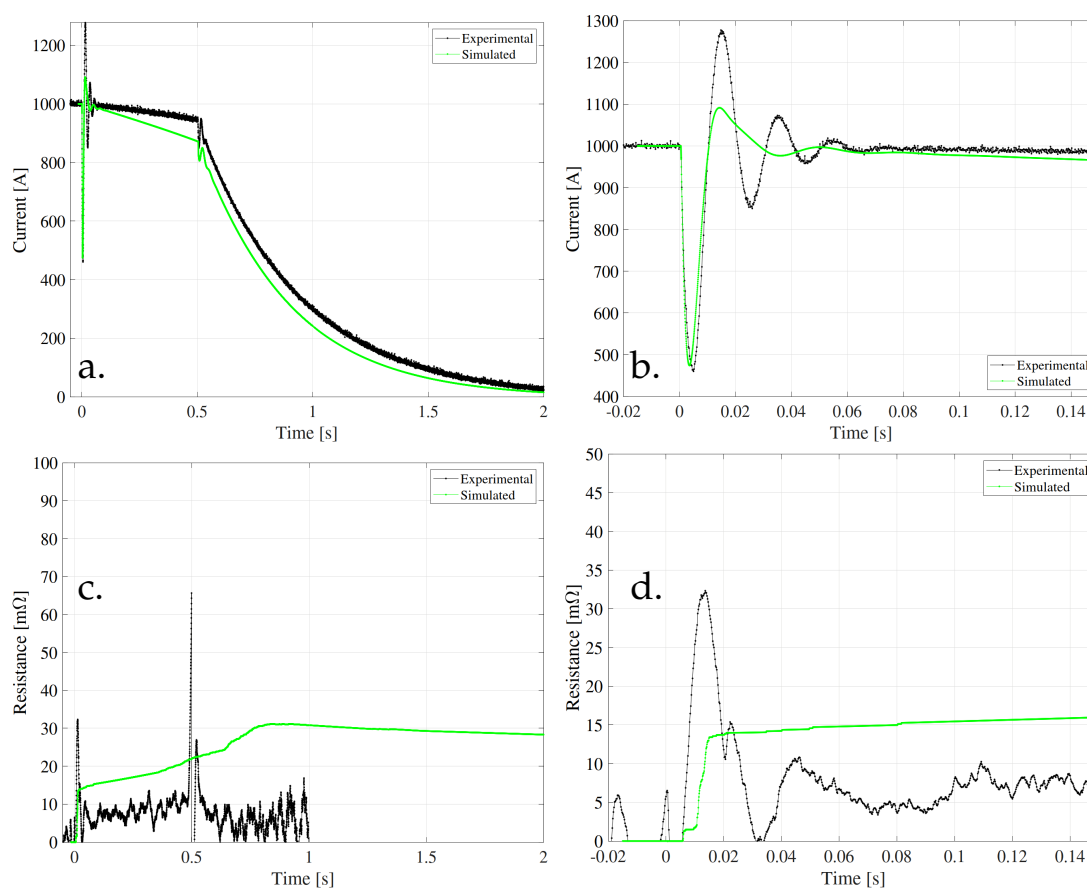
FIGURE 5.24: CLIQ and Delayed Energy Extraction (Test 12, see Tab. 5.1). a. Magnet current versus time. 115 b. Zoom in the magnet current. c. Magnet resistance versus time. d. Zoom in magnet resistance.

TABLE 5.11: Absolute and relative error on the magnet current for Test 10, Test 11, Test 12, and Test 13.

	RMSE [A]	Max ∣E∣ [A]	$<E_r>$ [%]	Max E_r [%]
Test 10	71.4	298.0	10.7	21.5
Test 11	82.6	304.8	13.6	32.4
Test 12	45.0	143.7	4.0	23.2
Test 13	3.6	116.6	0.9	15.3
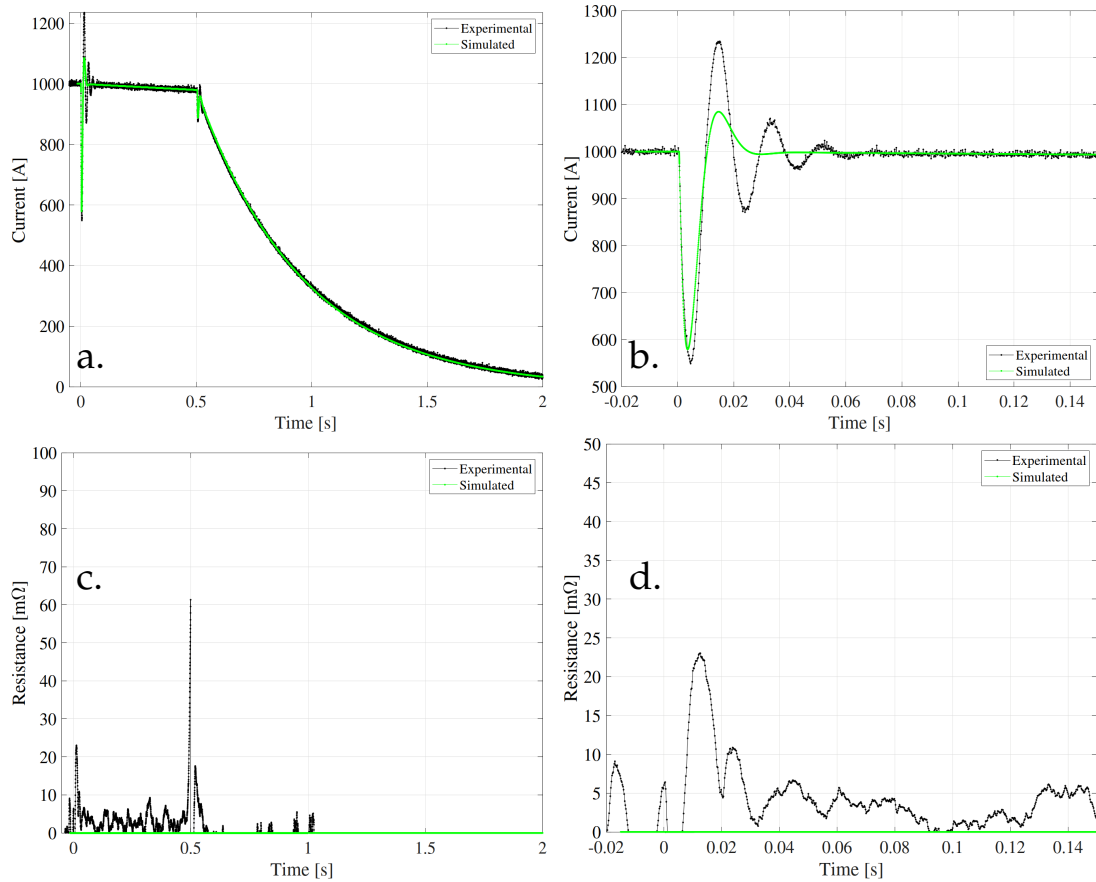
FIGURE 5.25: CLIQ and Delayed Energy Extraction (Test 13, see Tab. 5.1).
a. Magnet current versus time. b. Zoom in the magnet current. c. Magnet
resistance versus time. d. Zoom in magnet resistance.

The validation of the MQY magnet at 1.9 K gives good agreement between simulations and measurements, in particular in case of the transient with QHs and delayed EE, where the relative error (I_{sim}-I_{meas}/I_{meas}) is under 1% also at low current level. For the transient with CLIQ and delayed EE the agreement between simulations and measurements worsens but still remains in an excellent range with the relative error under 4% for the tests performed with the unit CLIQ-1 (see Tab.5.8). While it increases in the simulations performed with the parameters of the unit CLIQ-2 (see Tab.5.8) due to the higher-amplitude oscillations difficult to reproduce on the simulation.

TABLE 5.12: Impact of the parameters on the MQY magnet model

Name	EE	QHs	CLIQ
Warm circuit resistance			
Scaling factor of the contact area on the QH strip		++	
Helium fraction in the cable cross-section		++	++
Quench velocity propagation		+(at low current)	
Residual Resistivity Ratio		+	+
Effective transverse resistivity parameter			++

5.2 MQY Sensitivity Analysis

During the validation of the MQY magnet model, different parameters were analyzed in different ranges to achieve a good validation of the MQY magnet model. Their impact on the simulation results is qualitatively summarized in Tab. 5.12.

The RRR and the circuit parameters ($R\_circuit$, $R\_crowbar$, and $V\_crowbar$) have been obtained during the validation thanks to the comparison between simulations and experimental data; Usually these values are known and, as the case of the RRR, not constant. The assumption of an uniform RRR in all coils of a magnet gives a additional uncertainty in the simulation. In future tests, the value of RRR will be measured to achieve a better agreement between simulations and experiments.

The fraction of helium in the insulated cable cross-section has a strong impact on the simulation results. During the validation of the model, different quantities of helium inside the cable cross-section have been tested. It is possible to achieve the best agreement between simulations and experimental data, also in case of different transients (QHs + delayed EE and CLIQ + delayed EE), for a quantity of helium that fills the 72% of the total voids inside the cable cross-section, i.e. 7% of the total insulated cross-section.

The scaling factor of the contact area between the quench heaters strips and the conductors is another important and no-common feature of the STEAM-LEDET tool. It was tested during the validation and, as the case of the helium quantity inside the cable cross-section, the values chosen during the validation are in a reasonable and acceptable range.

The STEAM-LEDET feature, used to update the 2D model in 2D+1D, was tested on the MQY magnet model during the protection transient generated by the quench heaters. In case of fast transients, as during the transient generated by the CLIQ protection, or in case of high operational current, the effect of this feature is negligible, while it gives interesting results at low current that encourage to implement it and better investigate the scaling factor of the quench velocity propagation. More analysis will be done with the future tests on the MQY magnet in particular at different temperature regime (4.5 K and 1.9 K) and larger current range (from 0.5 kA to 4 kA).

As mentioned in section 5.1 during the validation of the MQY magnet model only the IFCCs were taken into account. An accurate analysis of the simulations shows a faster quench in case of CLIQ and delayed EE protection. Furthermore, during the

model validation, the effective transverse resistivity parameter (a parameter strongly related to the IFCC) has been assumed constant on the magnet coils. The effect of the effective transverse resistivity has a big impact on the simulation, in particular on the simulations with a faster discharge of the magnet current, as the cases of transient generated by the CLIQ and delayed EE.

Thanks to the good agreement obtained during the validation of the MQY quadrupole magnet model with the experimental results is it possible conclude that the MQY model generated with STEAM-LEDET can be used to simulate the complex electro-magnetic and thermal transient occurring during the magnet discharge.

5.3   MQM Validation

For the validation of the MQM quadrupole magnet model (described in section 2.1), different parameters have been changed: RRR, effective transverse resistivity parameter, time constant that define the evolution of the IFCC/ISCC after a quench (τ_{IFCC} and τ_{ISCC}, see section 3.2.1), helium quantity inside the cable cross-section, and the cross-contact resistance. As done for the MQY, before changing the quantity of helium inside the insulated cable cross-section it is necessary to know the space which can by filled by the helium, i.e. the fraction of voids inside the cable cross-section. Knowing all the parameters of the cable bare and the diameter of the strands, it is possible to obtain the area of these voids. For the MQM magnet model, 72.34% of the cable is occupied by the strands, 17.42% by the insulation, and the remaining 10.23% are voids.

To automatize and accelerate the validation process of the magnet model using STEAM-LEDET a new notebook was generated. The Automatic Sweep Parameter Notebook [63] works on the SWAN platform (see section 3.1.2) in Python-3 language. It gives the possibility to choose the parameters to be changed in a predefined range. Once all the parameters are selected and the ranges are fixed the notebook generates a matrix with all the possible combinations of the parameters. The parameters and the ranges selected for the validation of the MQM magnet model are summarized in Tab. 5.13. The total number of simulations was 2880, for a simulation time of 140 hours (about 3 min per simulation). Once all the simulations were performed, the sweep parameter notebook compares all the simulations with the measured current, measuring the deviation, and giving back the 10 simulations with the best fit.

In order to compare simulations and measurements, different Fast Power Abort (FPA) tests were collected using the LHC signal monitor notebook [38].

TABLE 5.13: Parameters and range selected on the Sweep Parameters notebook for the MQM magnet model validation at T=1.9 K.

He quantity inside the cable cross-section [%]	3	4	5	6	
Effective transverse resistivity parameter [-]	1	2	3	4	
Cross-contact resistance [$m\Omega$]	10^{-3}	0.667	0.334	1	
RRR [-]	50	75	100	125	150
τ_{IFCC} [s]	0.001	0.01	0.1		
τ_{ISCC} [s]	0.001	0.01	0.1		

5.3.1 Validation with a bath temperature of 1.9 K

All the tests selected for the validation of the MQM magnet model are in a configuration with two magnets MQM in series, i.e. four apertures. The starting currents of the FPA tests are not exactly the same, for this reason the measured currents levels of the tests were normalized with the simulation current value (5440 A). The four best simulations selected by the notebook thanks to the comparison with the average of the three FPA currents, are shown in Fig. 5.26. In Tab. 5.14 are summarized the values of the parameters, and absolute and relative error for each simulation. The bump, visible at the end of the current discharge in Fig. 5.26 a, is related to the simulation of the voltage. STEAM-LEDET sets the voltage across the diode to $U_{forward}$ when the current is higher than 10 A, and to 0 V if the current is lower than 10 A. This event is not relevant for quench protection as the magnet is almost discharged.

TABLE 5.14: Parameters and absolute and relative error on the magnet current of the best four simulations selected during the validation of the MQM magnet model.

	Sim 1	Sim 2	Sim 3	Sim 4
He quantity inside the cable cross-section [%]	4	4	3	3
Effective transverse resistivity parameter [-]	1	2	2	1
Cross-contact resistance [$m\Omega$]	$1e^{-3}$	$1e^{-3}$	1	1
RRR [-]	100	100	100	75
τ_{IFCC} [s]	0.001	0.001	0.001	0.001
τ_{ISCC} [s]	0.1	0.1	0.1	0.1
RMSE [A]	32.7	36.5	37.1	80.3
Max $|E|$ [A]	64.0	91.5	84.8	326.5
<E_r> [%]	3.9	5.0	5.0	6.1
Max E_r [%]	14.5	17.7	17.6	20.1

Looking at Tab. 5.14, *Sim 1* is the one with the best fit compared to the FPA tests, therefore the final parameters chosen for the validation of the MQM magnet model at T=1.9 K are:

- Residual Resistivity Ratio = 100
- Fraction of helium inside the insulated cable cross-section = 4 %
- Effective transverse resistivity = 1
- Cross-contact resistance = 1 $\mu\Omega$
- τ_{IFCC} = 0.001 s
- τ_{ISCC} = 0.1 s

As can be observed from the simulation's parameters summarized in Tab. 5.13, some parameters did not change, as the τ_{IFCC} and τ_{ISCC}, other, change in a large range, as the cross-contact resistance, it means that the impact of these parameters is different on the magnet simulation. Them will be better analyze in section 5.5
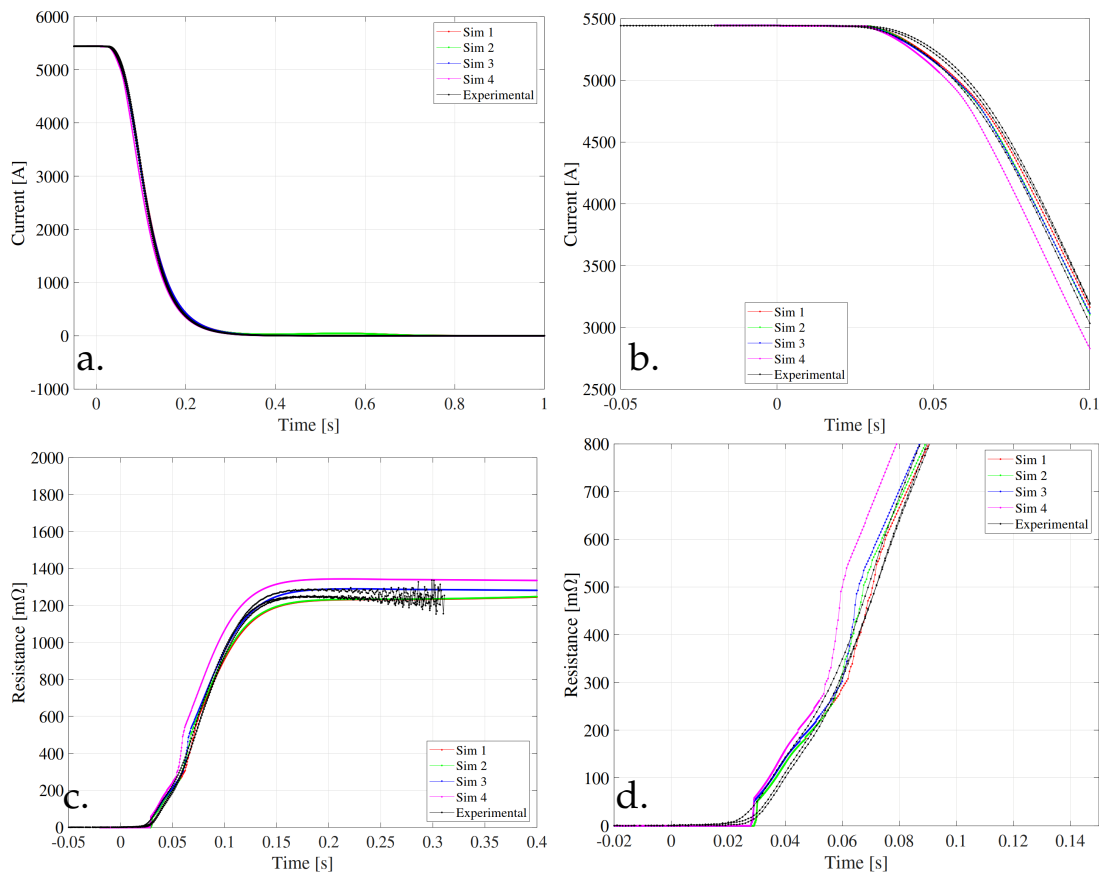
FIGURE 5.26: Best simulations for the MQM magnet model using the Sweep Parameter Notebook. a. Magnet current versus time. b. Zoom in the magnet current. c. Magnet resistance versus time. d. Zoom in magnet resistance.

5.3.2 Validation with a bath temperature of 4.5 K

In 2 of the 78 IPQ circuits are present two magnet MQM in series with an initial temperature of 4.5 K. To be consistent with the validation, the model parameters used during this validation, are the same as those used in case of an initial temperature of 1.9 K.

As for the previous validation, the measured currents levels are normalized with the simulation current value (4200 A). The comparison between the experimental data and the best simulation is shown in Fig. 5.27, while the absolute and relative error are reported in Tab. 5.15. It is easy to observe that at 4.5 K the agreement between the experiment and simulation worsened compared to the case at 1.9 K, this is because the heat capacity of the helium changes more of the 80% between 1.9 K and 4.5 K. Therefore, it is necessary to update the feature in the STEAM-LEDET tool to properly simulate the helium heat capacity when it passes from liquid to gaseous state.
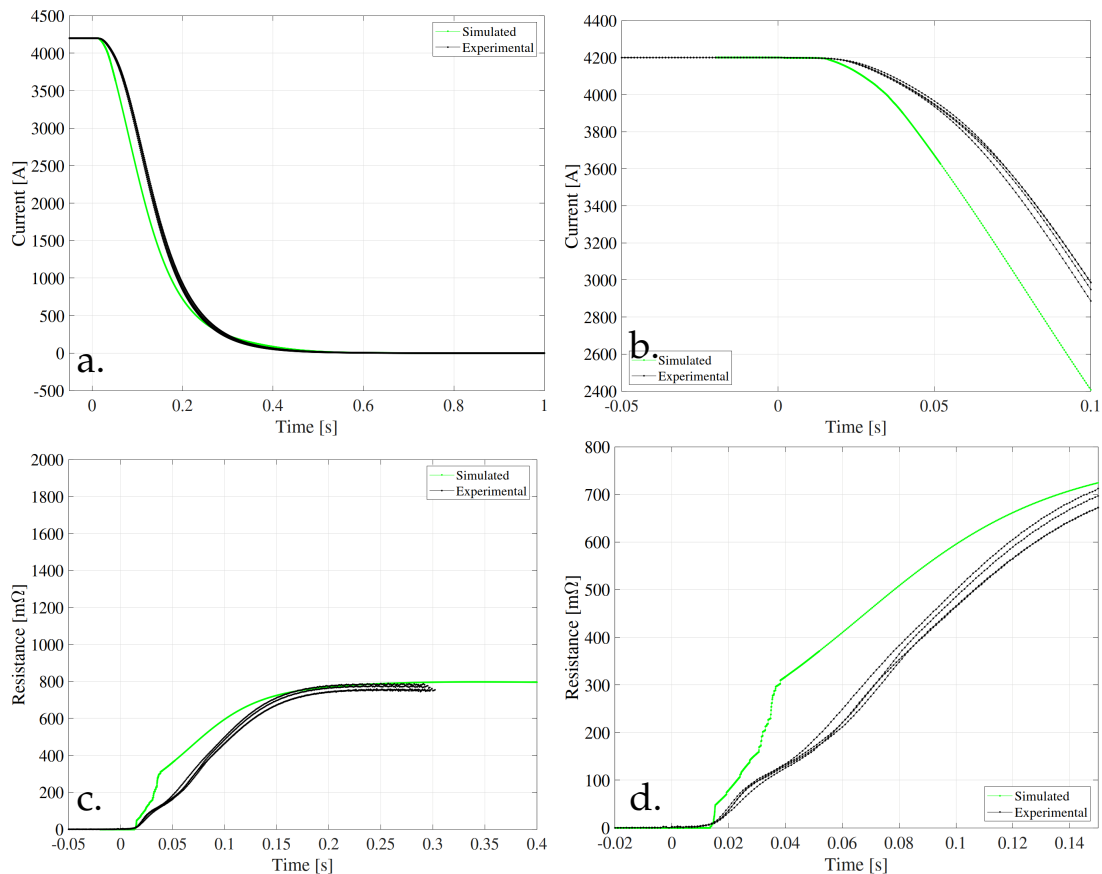
FIGURE 5.27: Simulation vs Experimental data for the validation of the MQM magnet model at 4.5 K. a. Magnet current versus time. b. Zoom in the magnet current. c. Magnet resistance versus time. d. Zoom in magnet resistance.

TABLE 5.15: Absolute and relative error on the magnet current of the best simulation selected during the validation of the MQM magnet model at T=4.5 K.

	Sim
RMSE [A]	213.05
Max $|E|$ [A]	547.50
$<E_r>$ [%]	14.51
Max E_r [%]	22.16

5.4 MQML Validation

As done for the MQM magnet model, also for the MQML the validation was done using the automatic sweep parameter notebook. The main differences between the two magnets models are the magnetic length (3.4 m and 4.8 m for the MQM and MQML, respectively) and the longitudinal fraction of QH strip covered with heating stations (0.41 and 0.29 for the MQM and MQML, respectively). With the same QH unit (same QH C [mF] and U [V]) it is possible to obtain similar power deposition in the heating station also if the QH strips connected have different lengths and different eating-station fractions.

The MQML magnet is present in the IPQ circuit without any other magnet in series, i.e. one magnet, two apertures. An exception occurs in some RQ6 circuits, where one MQML magnet is in series with one MQM magnet (see Appendix A).

5.4.1 Validation with a bath temperature of 1.9 K

The parameters and the ranges used for the validation of the MQML model are the same used for the MQM (see Tab. 5.13). The four best simulations, selected automatically from the sweep parameter notebook, are shown in Fig. 5.28, while the parameters and absolute and relative errors on the magnet current are reported in Tab. 5.16. As a consequence of the different magnetic length and the different heating-station fraction, the parameters that better represent the MQML model in the validation are slightly different from the ones estimated during the MQM model validation. As it is possible to observe in Tab. 5.16 all the simulations selected by the notebook are in good agreement with the experimental data. Taking into account the similarity of the two magnets, for consistency the simulation chosen as a reference (*Sim 4*) has the same quantity of helium inside the cable cross-section used to validate the MQM model. Also the RRR is different between the two magnet models, RRR=100 and RRR=150 for MQM and MQML magnet, respectively. The growth of the RRR is in acceptable range because, also if the magnets are in series, they are different.
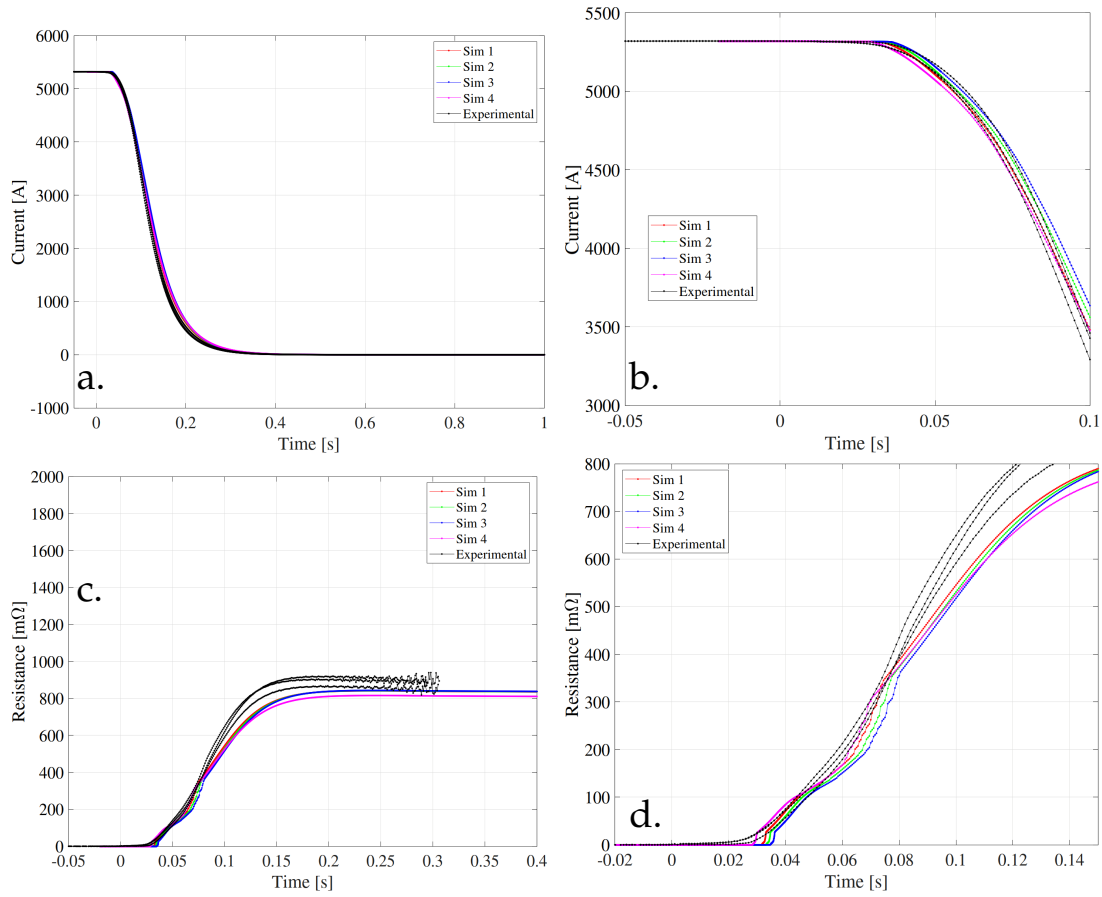
FIGURE 5.28: Best simulations for the MQML magnet model using the Sweep Parameter Notebook. a. Magnet current versus time. b. Zoom in the magnet current. c. Magnet resistance versus time. d. Zoom in magnet resistance.

TABLE 5.16: Parameters and absolute and relative error on the magnet current of the best four simulations selected during the validation of the MQML magnet model at T=1.9 K.

	Sim 1	Sim 2	Sim 3	Sim 4
He quantity inside the cable cross-section [%]	5	5	6	4
Effective transverse resistivity parameter [-]	1	1	1	1
Cross-contact resistance [$m\Omega$]	$1e^{-3}$	$1e^{-3}$	1	$1e^{-3}$
RRR [-]	125	125	125	150
τ_{IFCC} [s]	0.001	0.001	0.001	0.001
τ_{ISCC} [s]	0.1	0.1	0.1	0.1
RMSE [A]	71.2	95.2	121.4	91.5
Max |E| [A]	192.6	261.2	332.0	229.8
<E_r> [%]	3.7	5.0	6.5	4.2
Max E_r [%]	12.4	16.3	20.0	14.9
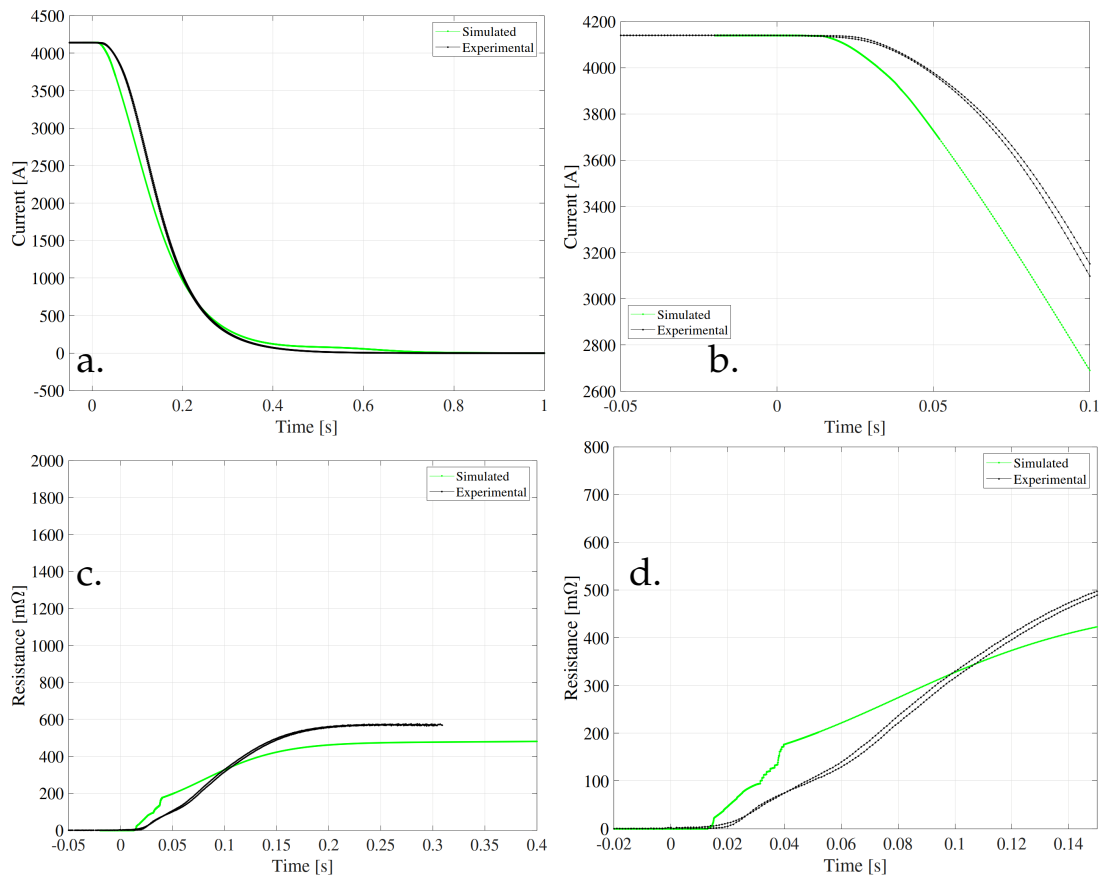
FIGURE 5.29: Simulation vs Experimental data for the validation of the MQML magnet model at 4.5 K. a. Magnet current versus time. b. Zoom in the magnet current. c. Magnet resistance versus time. d. Zoom in magnet resistance.

5.4.2   Validation with a bath temperature of 4.5 K

In some IPQ circuits the MQML magnet operates at 4.5 K in a stand-alone configuration (i.e. two apertures). The validation of the MQML magnet model at 4.5 K against two FPAs is shown in Fig. 5.29. The parameters used for the validation are kept constant (i.e. the same used at 1.9 K) and they are summarized in Tab. 5.17. As explained during the validation of the MQM magnet model, at 4.5 K, the heat capacity of the helium at 4.5 K is different from the one at 1.9 K.

TABLE 5.17: Parameters and errors of the best four simulation selected during the validation of the MQML magnet model at T=4.5 K.

	Sim
He quantity inside the cable cross-section [%]	4
Effective transverse resistivity parameter [-]	1
Cross-contact resistance [$m\Omega$]	$1e^{-3}$
RRR [-]	150
τ_{IFCC} [s]	0.001
τ_{ISCC} [s]	0.1
RMSE [A]	154.4
Max |E| [A]	441.4
<E_r> [%]	9.4
Max E_r [%]	14.3

5.5 MQM and MQML Sensitivity Analysis

During the validation of the MQM and MQML magnet models, different types of parameters were analyzed. The impact of these different parameters is qualitatively summarized in Tab. 5.18.

The circuit parameters of the model (R_*circuit*, R_*crowbar*, and V_*crowbar*) are deduced from the experimental current during powering and slow power abort transients, thus R_*circuit*+R_*crowbar* is equal to the sum between the two warm resistances, and V_*crowbar* is the voltage drop across the diodes.

As already mentioned, the assumption of an uniform RRR in all coils of a magnet gives a additional uncertainty in the simulation. In future tests, the value of RRR will be measured to achieve a better agreement between simulations and experiments. The value used in the model was obtained thanks to a comparison with the experiments. It can give a non-negligible impact on the simulation results.

During the validation of the model, different quantities of helium inside the cable cross-section were tested. A helium quantity around 4% in the cable cross-section gives the better agreement with the experimental data at 1.9 K, while it has lower impact on the results at 4.5 K. The new STEAM-LEDET feature introduced to update the 2D model in the 2D+1D has a negligible effect for the MQM and MQML validation at nominal current, because in this condition the quench propagation velocity is high that is possible to consider the entire length of the half-turn immediately quenched when the half-turn is quenched in the 2D model.

During the MQM/MQML validation the protection is relies on the quench heaters, therefore the effect of the coupling currents (IFCC and ISCC) are limited during the transient. As a consequence, the impact of the cross-contact resistance and the effective transverse resistivity parameter is negligible at both temperatures.

A good agreement during the validation between the magnets models and the experimental data at 1.9 K was obtained, whit a relative error of less than 5%. The models generated with the STEAM-LEDET tool can be used to simulate the complex electro-magnetic and thermal transient occurring during the magnet discharge. In case of temperature around 4.5 K the agreement gives a relative error around 13%, which is not yet satisfactory. Therefore, it is necessary to update the feature to properly simulate the helium heat capacity when it passes from liquid to gaseous state.

TABLE 5.18: Impact of the parameters on the MQM/MQML magnet model on quench-heater protection simulations at nominal current

Name	MQM/MQML at 1.9 K	MQM/MQML at 4.5 K
Warm circuit resistance		
Helium fraction in the cable cross-section	++	+
Quench velocity propagation		
Residual Resistivity Ratio	++	++
Effective transverse resistivity parameter		
Cross-contact resistance		

6 Co-simulation of transients in IPQ circuits

Once the magnets and circuits models have been generated and validated, they are combined within a co-simulation using the STEAM-COSIM tool [51]. In cases where the validation performed with STEAM-LEDET tool is not sufficient , e.g. for two different magnets in series, or for different currents in the magnet apertures, a second validation using STEAM-COSIM is needed.

As mentioned in section 3.3, STEAM-COSIM is a framework based on cooperative simulation developed at CERN. The goal of the co-simulation is to exchange information between several models in order to obtain a consistent solution. The different models are coupled thanks to the port concept. The port is an object composed of a name, type, set of model domains, inputs, and outputs. This information is needed to perform coupling parameter exchange between the models. An example of the ports files for the circuit RQ9.L1, is reported in the Appendix B.

In order to use a reasonable computational time and memory resources, the co-simulation is subdivided into several time-windows characterized by different time stepping. The time stepping was chosen taking into account the events occurring in the respective time windows. In the configuration file the time-window (between t_0 and t_{end}), the maximum time stepping size, the relative and absolute tolerance,and the paths for both models need to be specified. An example of this file for the circuit RQ9.L1, is reported in the Appendix C.

In the reported examples (appendixes C and B), the co-simulation is performed between the PSpice© circuit model (configuration with two magnets in series, see Fig. 2.7) and the two magnet models (MQM and MQMC) that run in parallel using the STEAM-LEDET tool. The ports for the two models (electrical and electro-thermal) are different in name and number. The number of the ports related with the electrical circuit (Appendix B.0.1) depends from the number of magnet apertures in the circuit (inductances), while the number of the ports related with the elector-thermal model (Appendix B.0.2 and B.0.3) depends on the number of coil sections of the magnet. The electrical model is composed of four ports (x from 1 to 4). The *Port_x* takes as inputs the resistance and the induced voltage of the magnet from the electro-thermal model (STEAM-LEDET), and in output returns the value of the current. The *Port_x_x* takes as input the information from the electro-thermal model on the induced voltage and it returns the same quantity but adapted to compensate the voltage across the

inductance (it is a result of consecutive interaction process between the two models). Each electro-thermal model is composed of two ports (y from 1 to 2). The *Port_y* is complementary to the port of the electrical circuit, i.e. it has one input (current) and two outputs (resistance and induced voltage).

To validate the co-simulation model, composed of the electrical circuit and the electro-thermal model, in fast transient, it is necessary to compare the simulations with measurements. The co-simulations are stopped at the time at which the magnet is almost completely discharged (discharged more than 90% with respect to the initial current) to reduce the simulation time. To test the behavior of the circuits, the FPA tests performed during the "LHC Hardware Commissioning" were used. There are two main types of FPAs: with the same current in both magnet apertures and with different currents in the magnet apertures.

6.1   Co-simulation with the same current in both magnet apertures

In this section different types of circuits have been validated. The co-simulated circuits have been selected to represent the whole IPQ circuit family. In particular, were analyzed cases with different operating temperatures (1.9 K and 4.5 K). In particular, the analyzed cases include transients with different type of magnet (MQM and MQY). In the comparison, the simulated curves are reported in red and green (first and second aperture) and the measurements curves in black. Current and voltage signals were acquired during the tests with a different sampling frequency (1000 Hz and 100 Hz, respectively). For this reason, the voltage drop after the switch-off of the power converts, at t=0 s, is different between simulation and measurements. In fact, there are only three measured points between the maximum and the minimum voltage. Moreover, in many different comparisons, the starting point of the voltage drop is different between measurements and simulations. This is due to the ramp-up of the current (1 to 5 A/s) before the switch-off of the power converts during the test. The ramp up is not visible in the current because of the current scale, but it is negligible in the voltage drop. Sometimes, to compensate the lack of experimental data, measurements of different circuit, but with the same configuration and operating conditions, are used to validate the models.   This affects the voltage drop, before the switch-off of the power converters (before t=0 s) because the circuit warm resistances are slightly different between the circuits. These phenomena affect the error on the voltages in the magnet.

6.1.1 RQ4, RQ5, RQ7, and RQ8 circuits

The circuits analyzed in this subsection are the RQ4.L6 (one MQY manget at 4.5 K), RQ4.L8 (two MQY magnets at 4.5 K), RQ5.L5 (one MQML magnet at 4.5 K), RQ7.L1 (two MQM magnets at 1.9 K), and RQ8.L1 (one MQML at 1.9 K) (see Appendix A).

MQML and MQM at T=1.9 K

RQ8.L1 is composed of one 4.8 m long MQML magnet that is operated at 1.9 K. The currents of the circuit versus the time are plotted in Fig. 6.1 a, and the across the power converters versus the time are plotted in Fig. 6.1 b. The inductive voltage during the ramp-up is clearly visible in Fig. 6.1 b, the voltages in the magnet start around 2 V instead of 1.3 V. The simulation results are in good agreement with the experimental results. Other important variables are calculated by the STEAM-LEDET
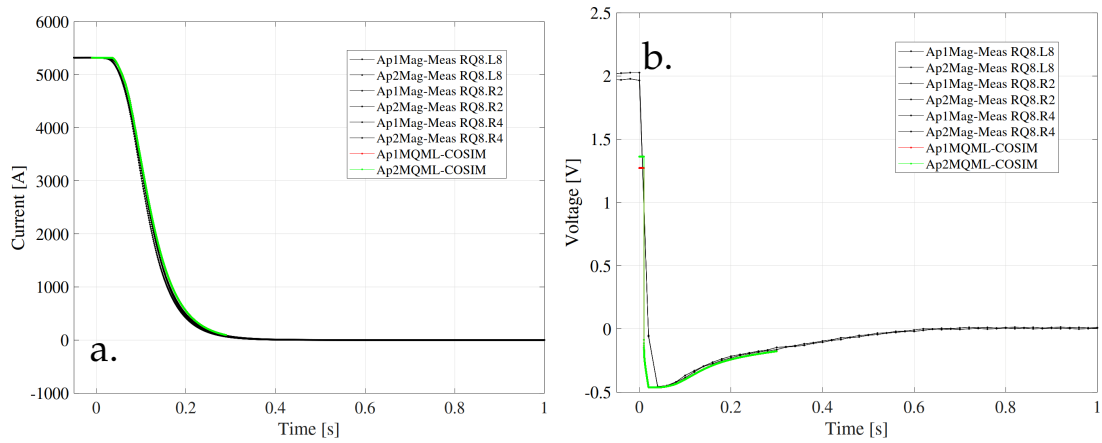
FIGURE 6.1: Simulations and measurements for a co-simulation at 1.9 K with the same current value in both magnet apertures (circuit RQ8.L1). a. DCCT Current versus time. b. Voltage across the power converter versus time.

model within the co-simulation, such as the temperature distribution in the magnet cross-section, the voltage to ground versus time, voltage to ground of each magnet turns at selected times, the coupling currents deposited in the magnet, etc. As an example, the temperature distribution for the MQML magnet is shown in Fig. 6.2. The temperature is higher in the turns of the outer layer which are in contact with the QHs strips. While, the inner-layer turns are quenched later due to thermal diffusion from the previously quenched outer-layer turns, and due to coupling loss developed during the current discharge. The temperature is symmetrical in the two apertures due to the same current and magnetic field that flows through them. In Fig. 6.2 inter-filament losses deposited in the magnet coil cross-section can be observed. They are mainly deposited in the inner-layer turns because on the outer-layer the turns are quenched due to the QHs, and the coupling loss do not develop in turns already in the normal state. Therefore the coupling current does not have a big impact on them.
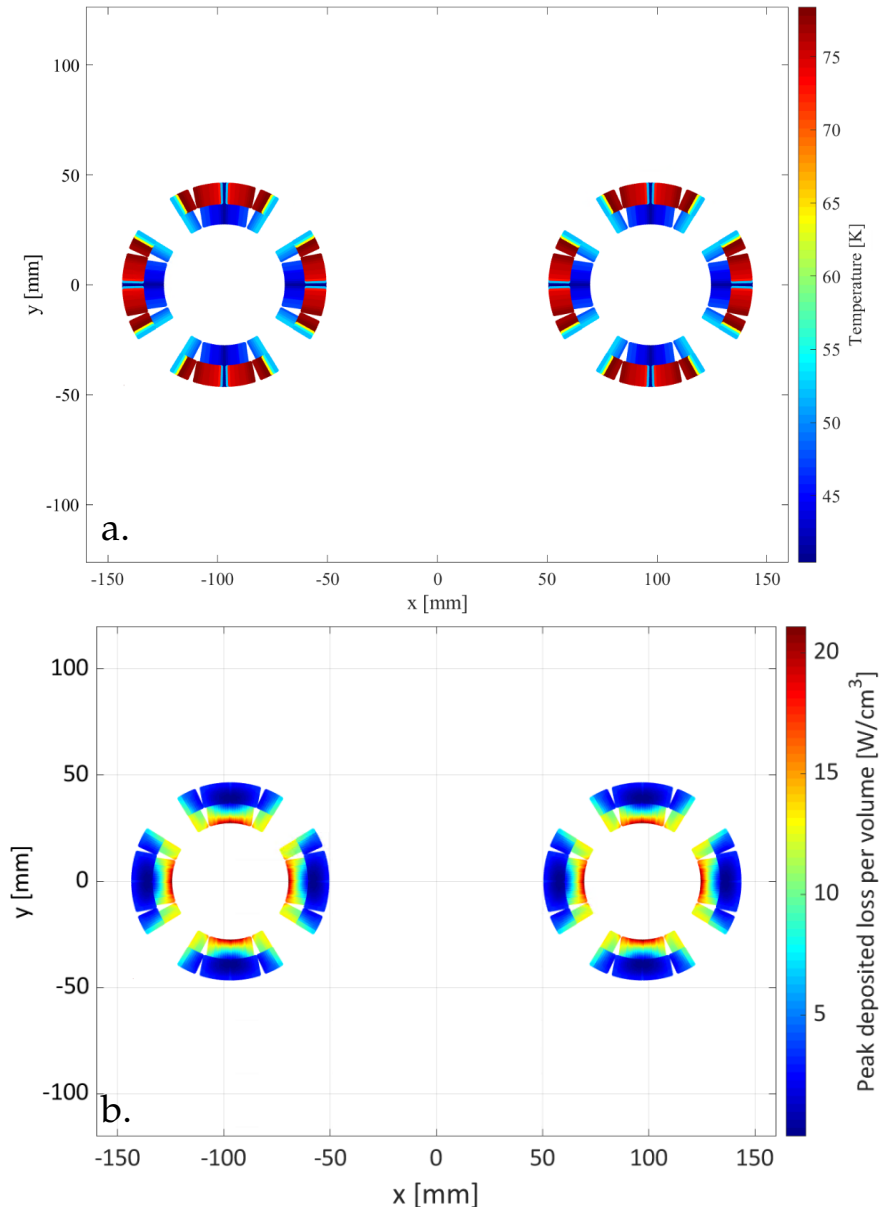
FIGURE 6.2: Temperature in the magnet model cross-section and peak inter-filament coupling loss for a co-simulation at 1.9 K with the same current value in both magnet apertures (circuit RQ8.L1). a. Peak temperature in the MQML magnet model cross-section. b. Peak inter-filament coupling loss per unit volume in the magnet cross-section.

After the co-simulation, the voltage to ground (Fig. 6.3 a and Fig. 6.3 b) is calculated taking into account the magnet internal voltage to ground and the voltage to ground in the electrical circuit at one side of the magnet (few volts compared to the total). In Fig. 6.3 a the voltage to ground of all turns versus time is shown (each line represents a turn). During the simulation, the voltage is constant for the first millisecond after the switch-off of the power converters, later it increases with the spread of the quench. Around 7 ms a large negative voltage peak is visible, which arrives when the QHs
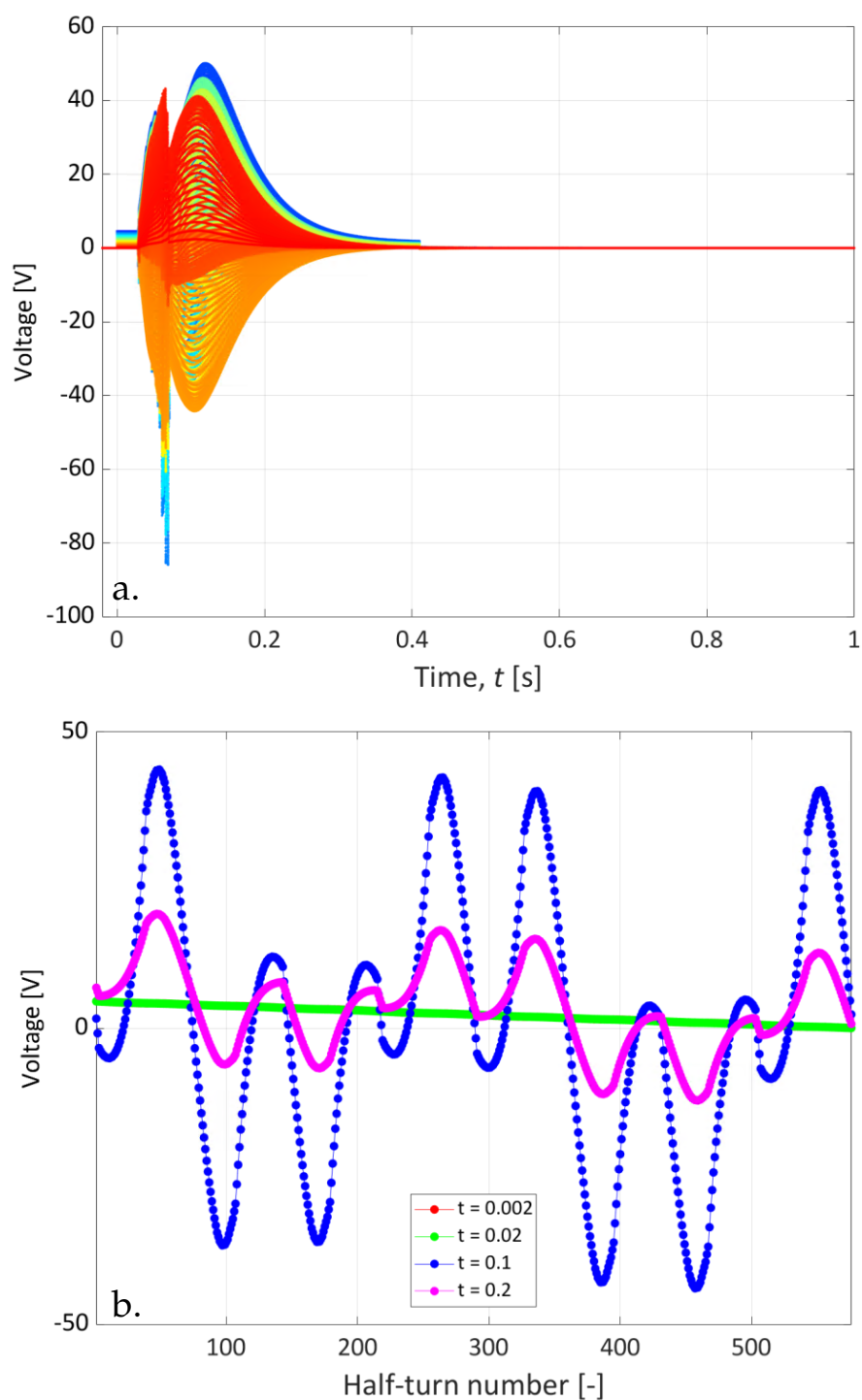
FIGURE 6.3: Voltage to ground of the co-simulation at 1.9 K (circuit RQ8.L1). a. Voltage to ground of the magnet turns versus time. b. Voltage to ground after each magnet half-turns at different selected time.

force the quench in a big part of the coil causing instability in the model. This peak is due to the numerical issues, but it does not affect a lot the simulation results because the energy in the coil is almost discharged (i.e. a big part of the coil is passed to the

normal conducting state). In Fig. 6.3 b the voltage to ground of all the 576 half turns is shown at different times (represented by different colors). From t=0.002 s to t=0.02 s the voltage is linearly distributed and close to zero (i.e. the green and red curves perfectly overlap), while it starts to grow when a big part of the magnet coil passes from the superconducting state to the normal one. At t=0.1 s the voltage distribution shows symmetric patterns that repeat for each of the eight coils in the circuit (i.e. four per aperture). Some turns have higher resistive voltage component (positive slope), and some turns have higher inductive voltage component (negative slope). At t=0.2 s the discharge of the magnet is almost completed, for this reason the voltage in each half-turns is decreasing.

To deduce the quenching time of each magnet turn it is possible to analyze the temperature versus time shown in Fig. 6.4. For the MQML magnet three main groups of half-turns are distinguishable. The first group (i.e. blue lines) starts to heat up around 10 ms, these half-turns are the ones in direct contact with QHs strips. Around 25 ms a few half-turns (i.e. magenta lines) (the ones on the outer-layer but not in contact with the QHs strips) start to heat up and quench due to the heat propagation, and after 40 ms the remaining half-turns quench (i.e. green lines) due to the heat diffusion and the coupling loss.

Another interesting result is obtained comparing the measurements and the simulations of the QHs voltage as shown in Fig. 6.5. This result is useful because the QHs voltage is a parameter commonly monitored during the experimental measurements and it is possible to see that the operative conditions of the QHs protection are correctly reproduced by the simulation. The time constant of the voltage decay across the QH strip is:

$$\tau_{QH} = R_{QH} \cdot C_{QH}$$

where C_{QH} is the capacitance [F] of the capacitor bank connected with the terminals of each quench-heater strip and R_{QH} [Ω] is the resistance of the QH strip.
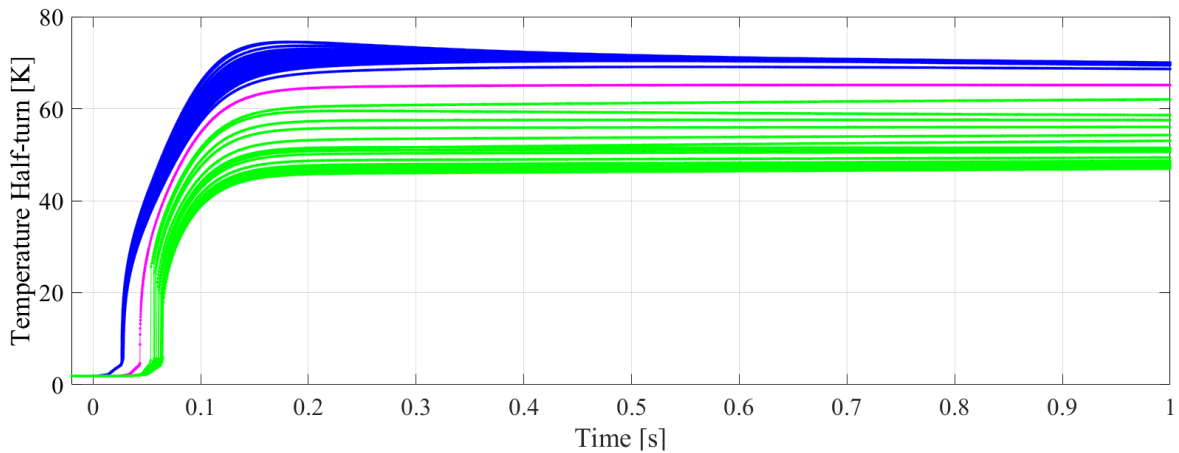
FIGURE 6.4: Temperature of each half-turn in the MQML magnet model versus time at 1.9 K (circuit RQ8.L1).
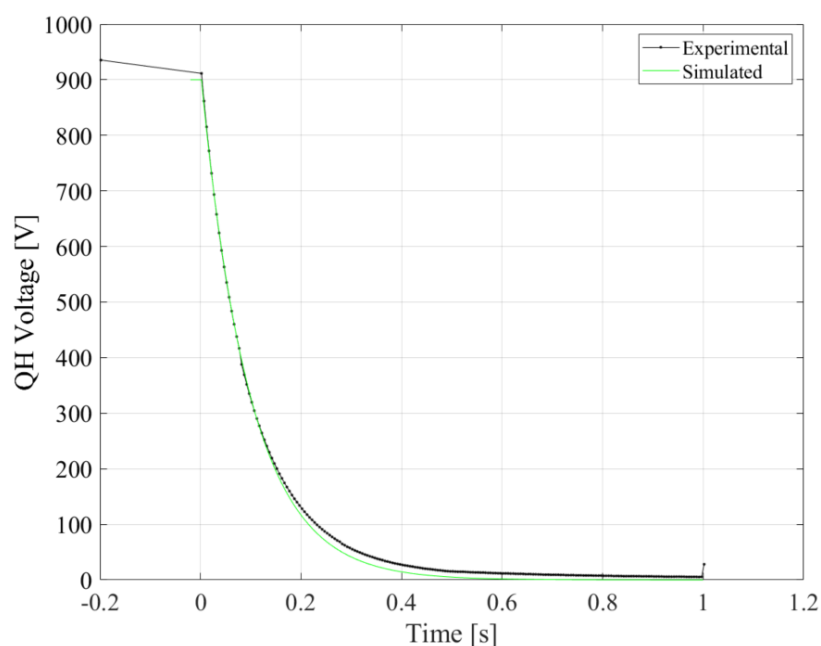
FIGURE 6.5: Voltage across the eight quench heaters versus time.

The second analyzed circuit is the RQ7.L1 is composed by two magnets, 3.4 m long, MQM in series, i.e. four apertures. Both apertures of the magnet, left-hand side and right-hand side are powered in series. The currents of the circuit versus the time are plotted in Fig. 6.6 a, and the across the power converters versus the time are plotted in Fig. 6.6 b. The co-simulation of the circuit RQ7.L1 at a temperature of 1.9 K is in good agreement with the experimental results. The co-simulation was stopped at 0.29 s because at that time the magnet current was almost fully discharged.
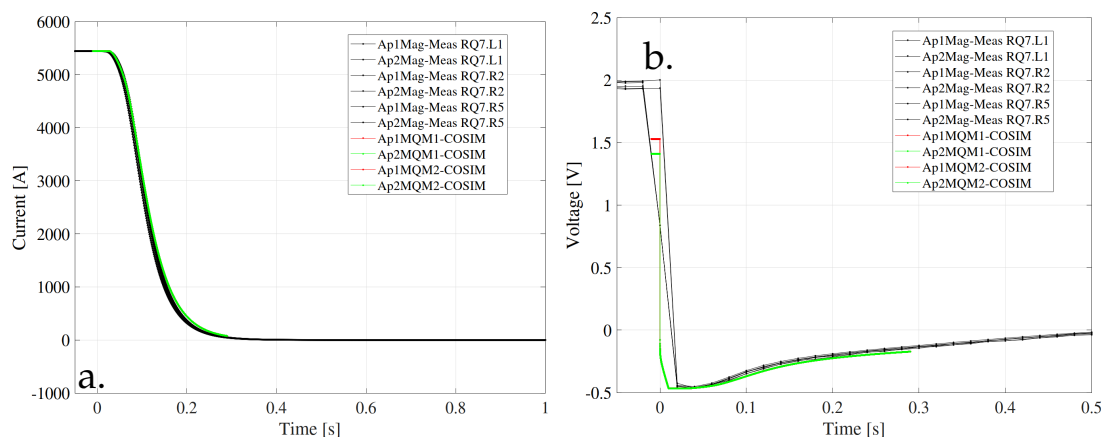
FIGURE 6.6: Simulations and measurements for a co-simulation at 1.9 K with the same current value in both magnets apertures (circuit RQ7.L1). a. DCCT Current versus time. b. Voltage across the power converters versus time.

MQY at 4.5 K

Some of the IPQ circuits in the LHC, as the circuits with the MQY magnets are operated at 4.5 K.

In the case with one MQY magnet (circuit RQ4.L6, see Appendix A), the current decay and the voltage across the power converters are shown in Fig. 6.7. As the previous cases, the current in the two magnet apertures is the same and it comes from a ramp-up (this explains the different voltage values between simulation and measurements at t=0 s). This circuit is operated at 3610 A, hence the magnet current is completely discharged in about 0.6 s, ans as a consequence the simulation was stopped at 0.8 s. For all the circuits simulated it is possible to observe the evolution of different physical properties in the STEAM-LEDET electro-thermal model. In Fig. 6.8 the temperature distribution and the deposited loss in the magnet coil cross-section are shown. In Fig. 6.8 a, is possible observe that the first, second, and third layers have a higher temperature. This is due to the magnet QHs strips, that are located on the outer layer, between the first and second layers, and between the second and third layers (see section 2.1). The fourth layer is the one with the lowest temperature and it is the most affected by the coupling current as shown in Fig. 6.8 b. The agreement between simulation and experimental result is good with an average relative error around 8%.
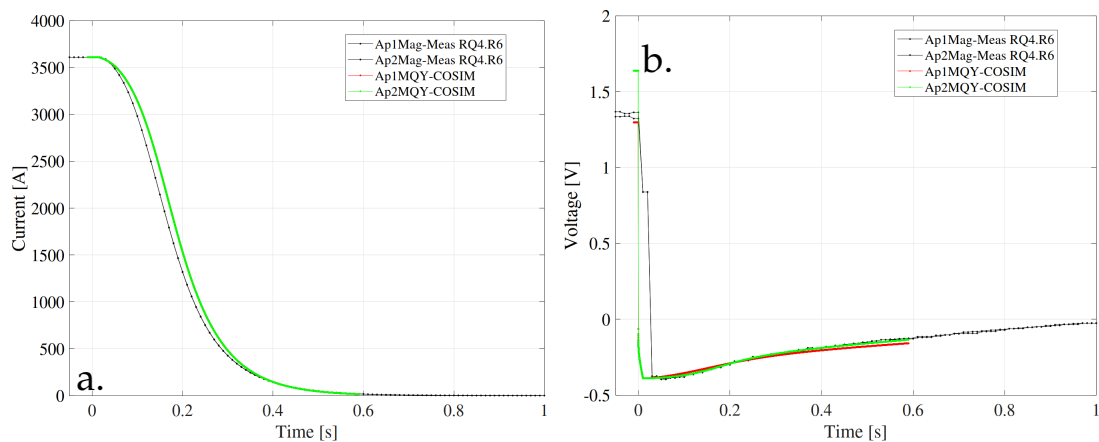
FIGURE 6.7: Simulations and measurements for a co-simulation at 4.5 K with the same current value in both magnet apertures (circuit RQ4.L6). a. DCCT Current versus time. b. Voltage across the power converter versus time.
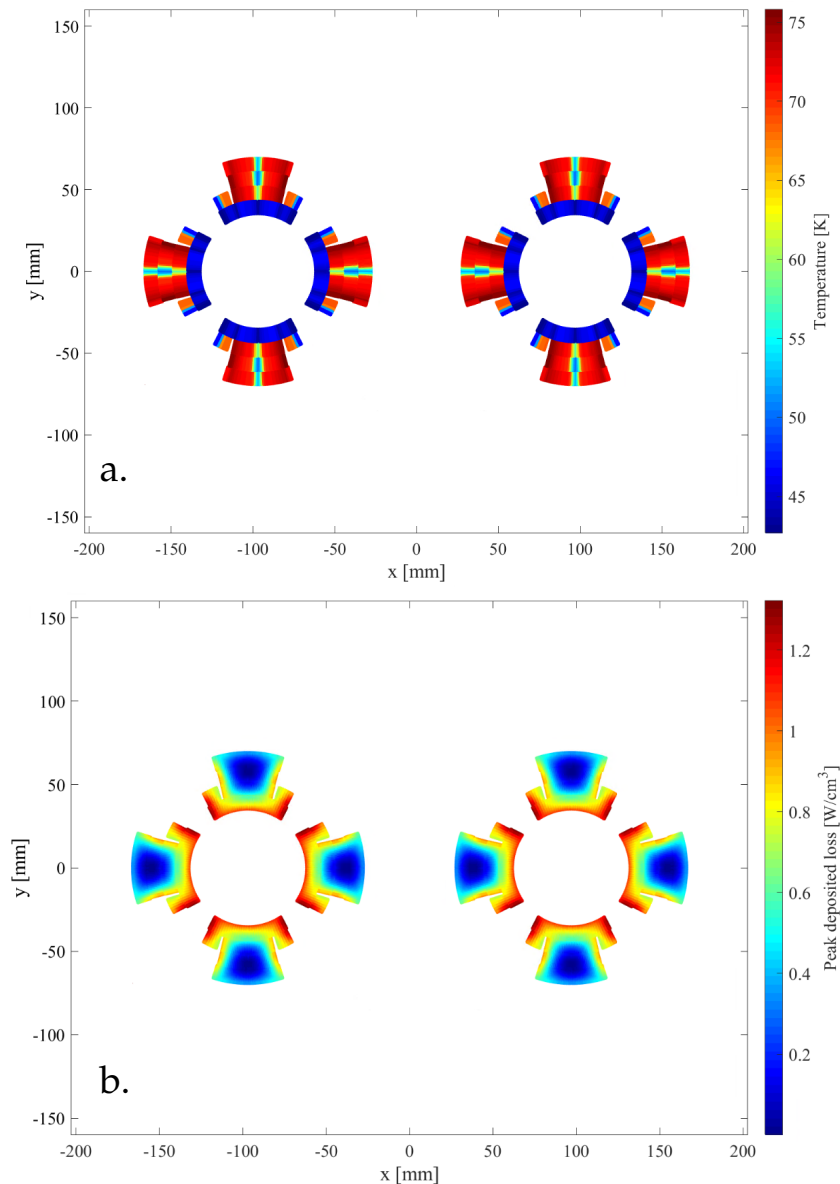
FIGURE 6.8: Temperature (a.) and deposited loss (b.) on the MQY magnet cross-section after a co-simulation at 4.5 K (circuit RQ4.L6).

The model of the circuits composed by two MQY magnets works correctly but it suffers due to the large amount of data related to the size of the MQY magnet, therefore the time-stepping during the simulation was increased (50 μs) to avoid issues linked to lack of memory. The simulation results compared to the measurements for the circuit RQ4.L8 are shown in Fig. 6.9. As for the circuits with one MQY, the co-simulation is in good agreement until 0.2 s, then the discrepancy between simulation and experimental results increases, and this is due to the helium heat capacity at 4.5 K. In Fig. 6.10 the temperature distribution and the voltage to ground are shown. The temperature distribution in the four apertures of the MQY magnets cross-section is the same because the same current passes through their conductor. The temperature distribution in the layers is higher in the first, second,
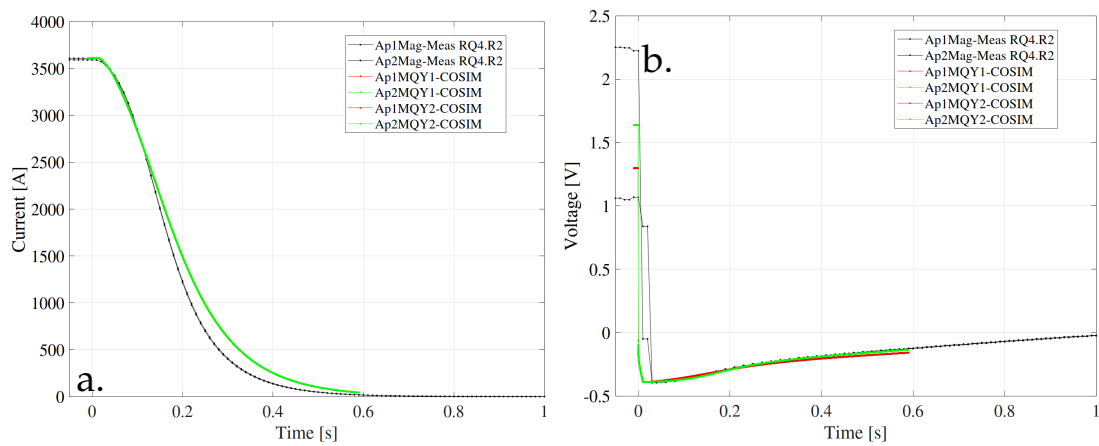
FIGURE 6.9: Simulations and measurements for a co-simulation at 4.5 K
with the same current value in both magnets apertures (circuit RQ4.L8).
a. DCCT Current versus time. b. Voltage across the power converter
versus time.

and third layers, while the fourth layer is most affected by the coupling current. In
Fig. 6.10 the voltage to ground of all the 1184 turns is shown (each turn is a line). As
for the previous co-simulation the peak is reached around 0.2 s once the majority of
the coil is passed to normal conducting state.
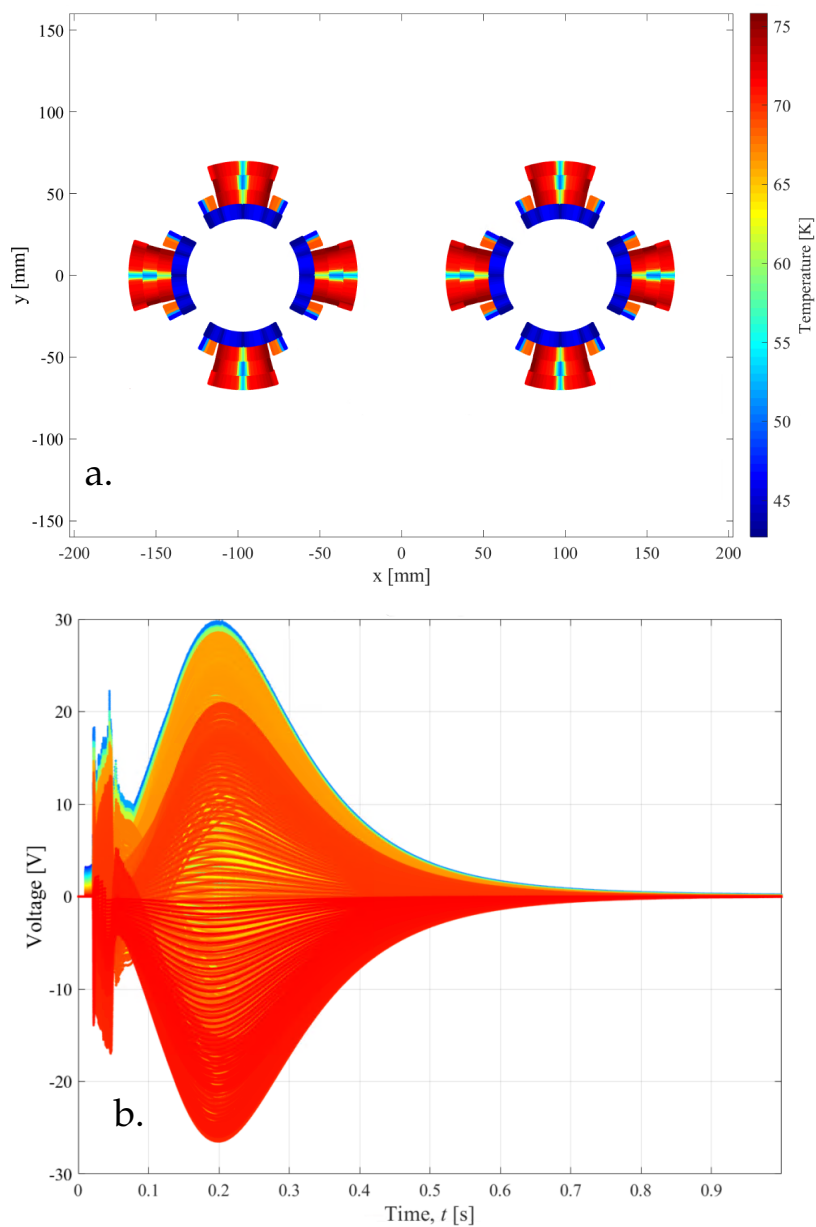
FIGURE 6.10: Temperature (a.) and Voltage to ground versus time (b.) on the MQY magnet cross-section after a co-simulation at 4.5 K (circuit RQ4.L8).
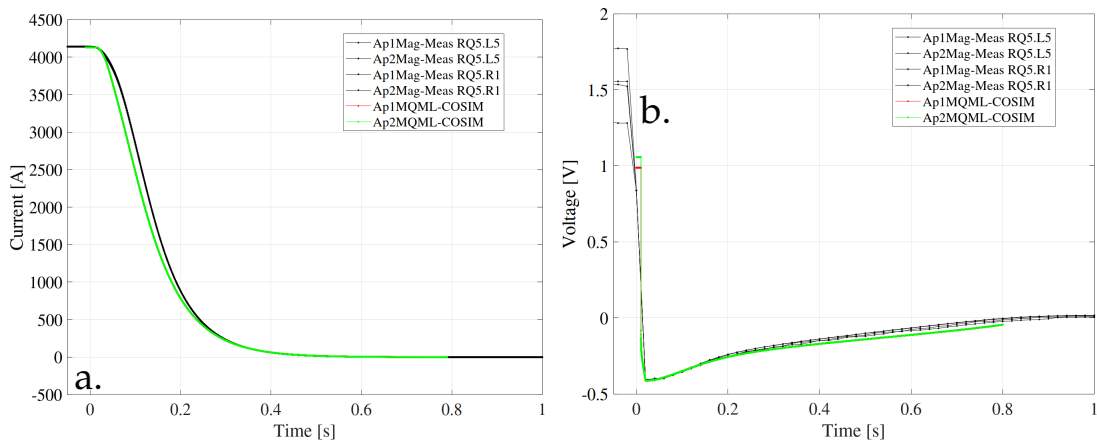
FIGURE 6.11: Simulations and measurements for a co-simulation at 4.5 K
with the same current value in both magnet apertures (circuit RQ5.L5).
a. DCCT Current versus time. b. Voltage across the power converter
versus time.
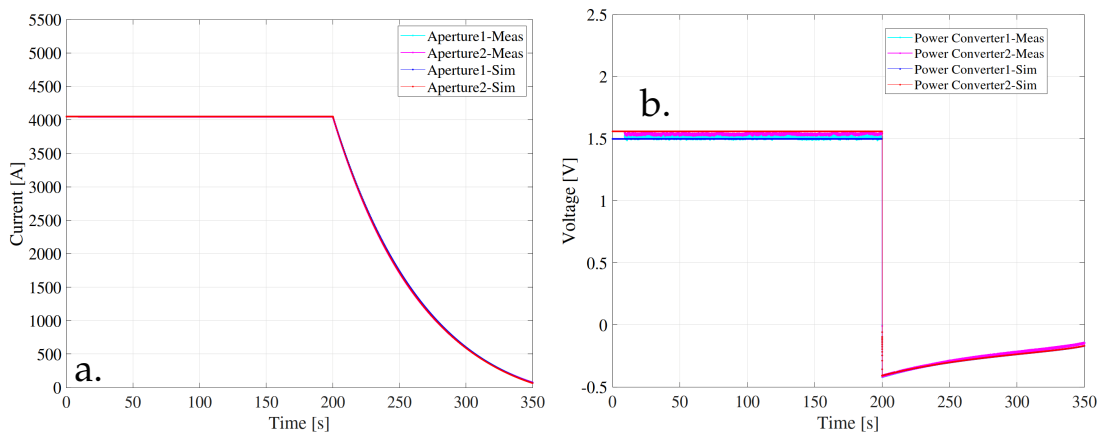
FIGURE 6.12: Simulations and measurements for a co-simulation at 4.5 K
with the same current value in both magnet apertures (circuit RQ5.L8).
a. DCCT Current versus time. b. Voltage across the power converter
versus time.

MQM and MQML at 4.5 K

Other circuits that operate at 4.5 K are composed of one MQML magnet and two
MQM magnets in series. The results of the co-simulations of circuit RQ5.L5 (one
MQML magnet) and RQ5.L8 (two MQM magnets) are shown in Fig. 6.12 and Fig. 6.11,
respectively. As in the previous cases, the current in the magnets apertures is the
same and it comes from a ramp-up (this explains the different voltage values between
simulation and measurements at t=0 s). The configuration of these circuits is as the
one analyzed in the previous subsection (RQ8.L1 and RQ7.L1), but in this case, both
circuits operate at 4.5 K, as a consequence the nominal current is around 4100 A. The
complete discharge of the circuits arrived around 0.4 s hence the simulations were
stopped at 0.7 s.   As it possible to observe in Fig. 6.13, at 4.5 K the impact of the
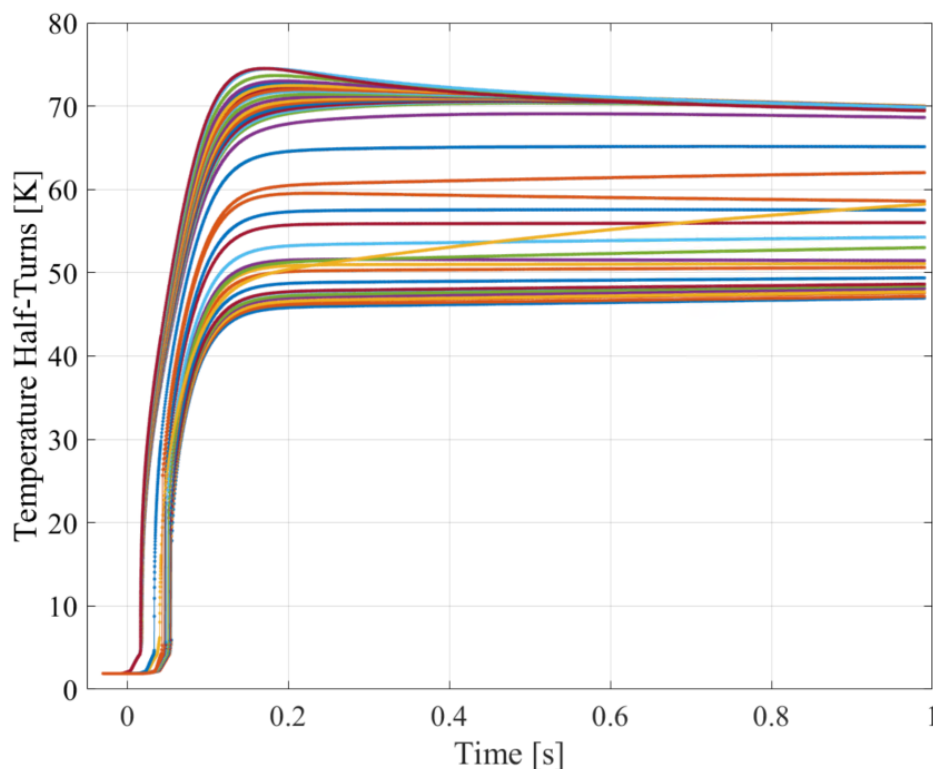
FIGURE 6.13: Temperature of each half-turn in the MQML magnet model versus time at 4.5 K (circuit RQ5.L5).

helium in the model is reduced due to the different heat capacitance of it, and the heating of the magnet turns is more homogeneous than the case at 1.9 K (see Fig. 6.4).

6.2 Co-simulation with unbalanced currents in the magnets apertures

Particular tests, using different current values in the two magnet apertures were performed at the end of 2013 to test the apertures individually powered. Simulate this particular scenario it is possible only using STEAM-COSIM, indeed the STEAM-LEDET tool does not permit to set up two different values of current in the magnet model, while it is possible on the PSpice© model setting two different stimulus on the power converters.

6.2.1   RQ4 and RQ7 circuits

In this section different co-simulation, of different circuits (RQ4.L5, RQ4.L8, and RQ7.L1) at different operating temperature, are shown in case of unbalanced currents.

MQY at 4.5 K

Circuits RQ4.L5 and RQ4.L8 are composed of 2 and 4 apertures, respectively. A fast power abort with unbalanced currents in the two circuit branches was simulated for both circuits. The simulated results for circuit RQ4.L5 and RQ4.L8 are compared to measurements in Fig. 6.14 and Fig. 6.15, respectively. The plots of the two simulations (Fig. 6.14 and Fig. 6.15) result very similar to each other.   For the circuit RQ4.L5 (i.e. one MQY magnet) the temperature in the magnet coil cross-section and the voltages to ground are shown in Fig. 6.16 a and Fig. 6.16 b, respectively. In Fig. 6.16 a the distribution of the temperature in the coils of the two apertures are not the same, this is due to the different currents through the apertures. In the first aperture of the magnet (on the left side of Fig. 6.16 a) the temperature is lower than in the second aperture (on the right side of Fig. 6.16 a) this is due to the current level flowing through the apertures, 2000 A and 3610 A for aperture one and two, respectively. The distribution of the temperature in the single aperture is the same as the one analyzed in the case of identical currents in both magnet aperture (see subsection 6.1.1). The effect of the unbalance current is visible also in Fig. 6.16 b, where it is possible to subdivide the plot of the voltage to ground in two main parts: one including the aperture with the lower current (red and orange curves), and another including the aperture with the higher current (green and blue curves).
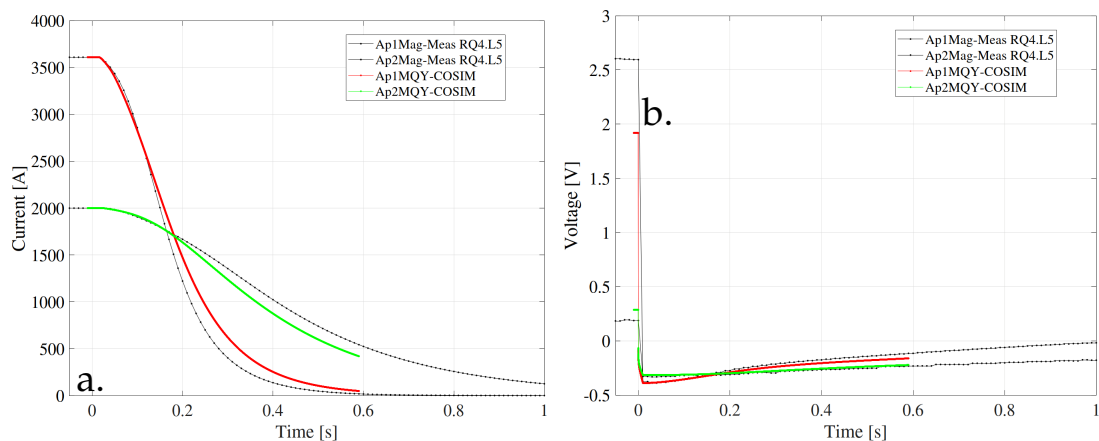
FIGURE 6.14: Simulations and measurements for a co-simulation at 4.5 K
with different current values in the magnet apertures (circuit RQ4.L5).
a. DCCT Current versus time. b. Voltage across the power converter
versus time.
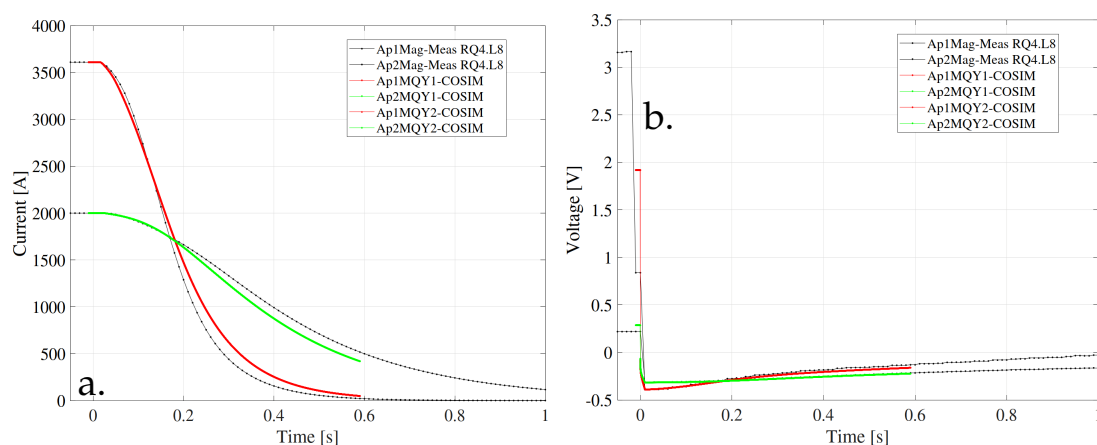
FIGURE 6.15: Simulations and measurements for a co-simulation at 4.5 K with different current values in the magnet apertures (circuit RQ4.L8). a. DCCT Current versus time. b. Voltage across the power converter versus time.

MQM at 1.9 K

In Fig. 6.17 the co-simulation at 1.9 K, of the circuit with two magnets MQM in series (RQ7.L1) is shown. In this validation the co-simulation is ended around 0.5 s to see also the discharge at low current that takes longer than the discharge at high current. The agreement on this co-simulation is good at both current levels with a maximum relative error around 10 %.
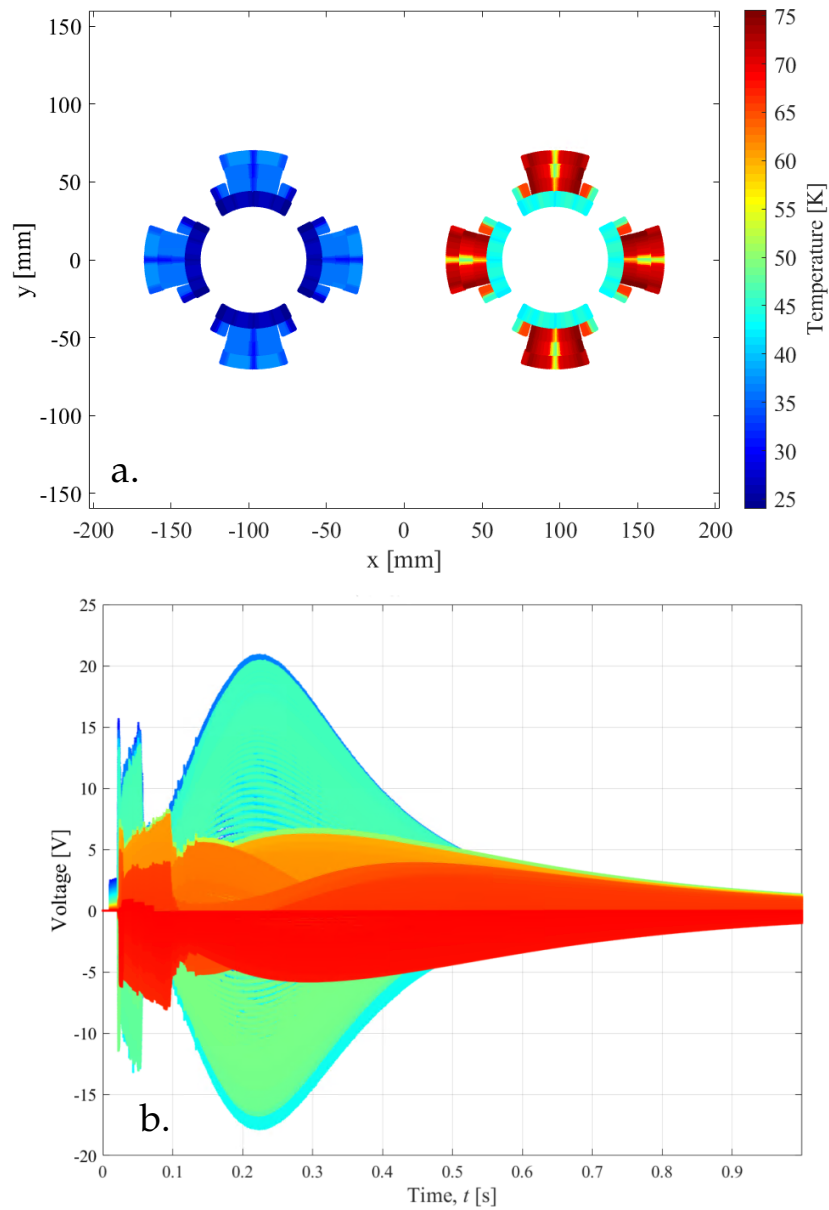
FIGURE 6.16: Simulations and measurements for a co-simulation at
4.5 K with unbalanced current in the magnet apertures (circuit RQ4.L5).
a. Temperature distribution in the MQY magnet cross-section. b. Voltage
to ground versus time of all the magnet turns.
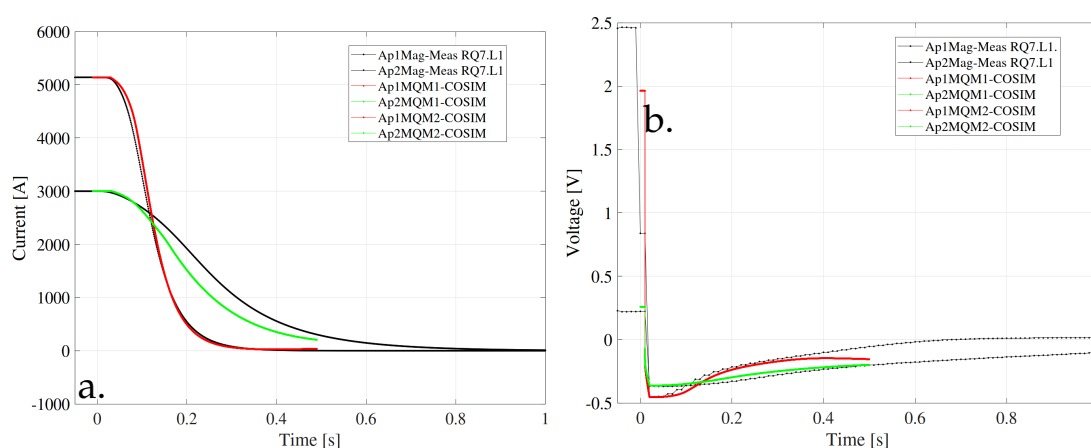
FIGURE 6.17: Simulations and measurements for a co-simulation at 1.9 K with different current values in the magnet apertures (circuit RQ7.L1). a. DCCT Current versus time. b. Voltage across the power converter versus time.

6.3 Co-simulation with different magnets in series

Other circuits where the co-simulation using STEAM-COSIM is needed are the ones with magnets of different types connected in series. Among the IPQ circuits, just two combinations with different magnets in series are present: MQM+MQMC (at 1.9 K) and MQM+MQML (at 4.5 K).

6.3.1 RQ9 circuits

All the RQ9 circuits, that operated at 1.9 K, are composed of one MQM magnet and one MQMC magnet (see Appendix 3.1). As explained in chapter 2.1 the 2D cross-section of these magnets is the same, the only differences between MQM and MQMC are the magnetic length (3.4 m and 2.4 m for MQM and MQMC, respectively) and the fraction of heating stations in the QH strips (0.41 and 0.56 for MQM and MQMC, respectively).

MQM+MQMC at 1.9 K

The results of a transient for the circuit with MQM+MQMC magnets in series at 1.9 K is shown in Fig. 6.18 (circuit RQ9.L8). The comparison between measurement and simulation shows good agreement. The simulation ended around 0.3 s when the magnets are almost discharged. The temperature distribution of the two magnets is shown in Fig. 6.19. The temperature is symmetric between the apertures of the two
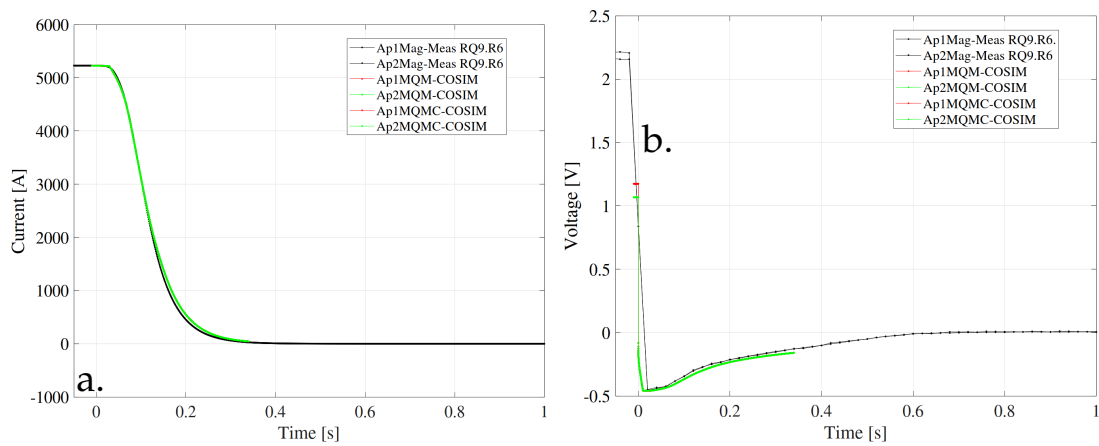
FIGURE 6.18: Simulations and measurements for a co-simulation at 1.9 K with different current values in the magnet apertures (circuit RQ9.L8). a. DCCT Current versus time. b. Voltage across the power converter versus time.

magnets, but it is different between MQM (Fig. 6.19 a) and MQMC (Fig. 6.19 b). This is due to the different quantity of Cu/SS in the QHs strips of the two magnet (170/120 for the MQM magnet and 100/125 for the MQMC magnet).
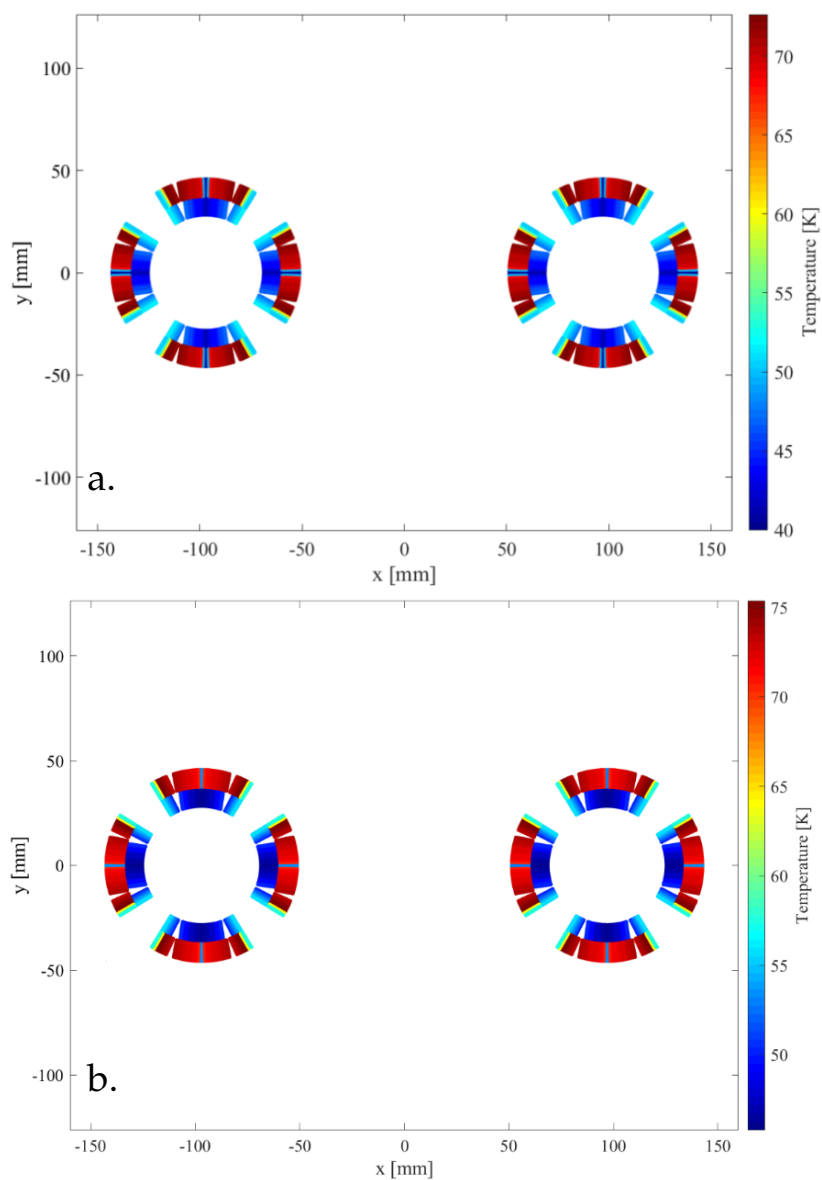
FIGURE 6.19: Temperature distribution in the magnet cross-section for a co-simultation at 1.9 K (circuit RQ9.L8). a. Temperature distribution in the MQM magnet cross-section. b. Temperature distribution in the MQMC magnet cross-section.

6.3.2   RQ6 circuits

Some circuits of the RQ6 family, that operated at 4.5 K, are composed of one MQM magnet and one MQML magnet (see Appendix 3.1). As explained in chapter 2.1 the 2D cross-section of these magnets is the same, the only differences between MQM and MQML are the magnetic length (3.4 m and 4.8 m for MQM and MQML, respectively) and the fraction of heating stations in the QH strips (0.41 and 0.29 for MQM and MQML, respectively).

MQM+MQML at 4.5 K

In Fig. 6.20 the co-simulation versus time of the circuit with MQM+MQML magnets is shown. The co-simulation is compared with one FPA test performed during the HWC before 2014. As can be observed, the comparison between simulation and measurement is in good agreement for the aperture at high current (red curve), but not for the one at low current (green curve). The simulation at low current will be better investigated in the future. The temperature distribution of the two magnets coil cross-section is shown in Fig. 6.21. As can be observed, the temperature is not symmetric in the apertures (this is due to the different current on the two) but it is also different between MQM (Fig. 6.21 a) and MQML (Fig. 6.21 b) and this is caused to the different quantity of Cu/SS in the QHs strips of the two magnet (170/120 for the MQM magnet and 350/140 for the MQML magnet).
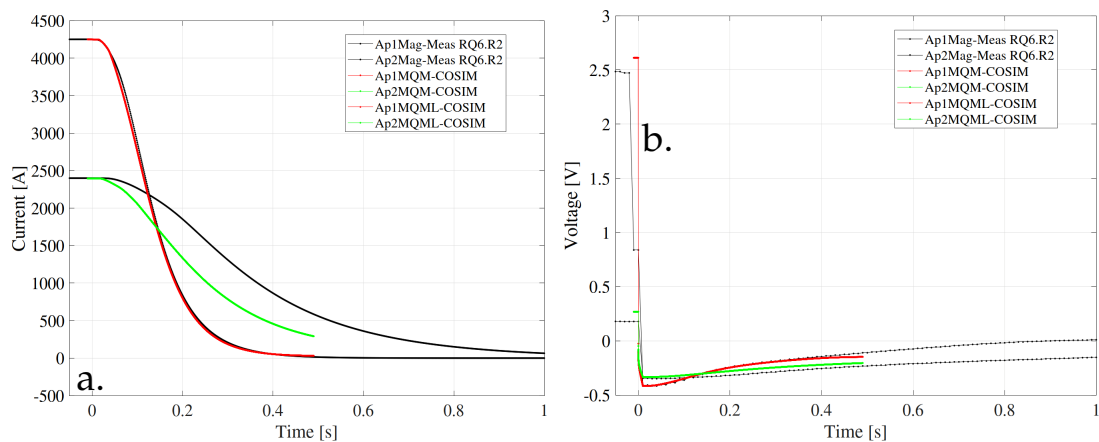
FIGURE 6.20: Simulations and measurements for a co-simulation at 4.5 K with different current values in the magnet apertures (circuit RQ6.R2). a. DCCT Current versus time. b. Voltage across the power converter versus time.
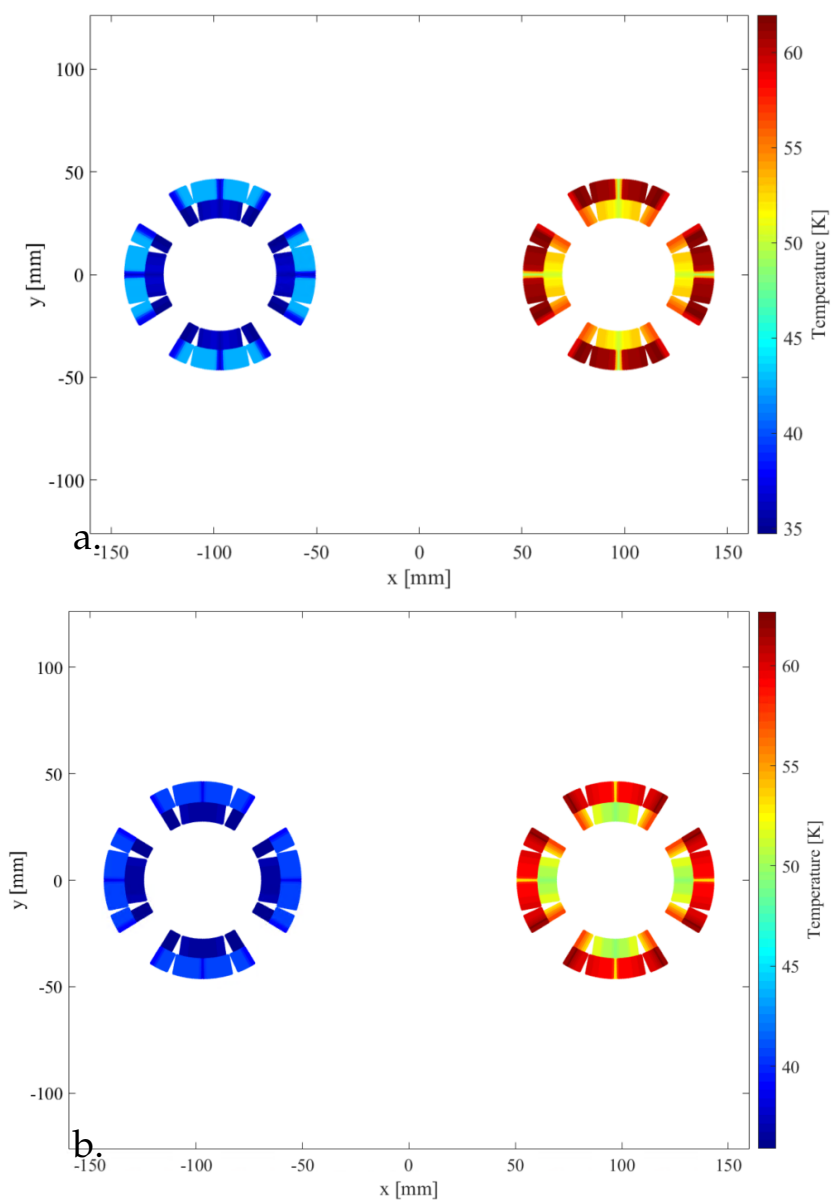
FIGURE 6.21: Temperature distribution in the magnet cross-section for a co-simultation at 4.5 K (circuit RQ6.R2). a. Temperature distribution in the MQM magnet cross-section. b. Temperature distribution in the MQML magnet cross-section.

7 Conclusions

The scope of this thesis was to develop, validate, and characterize the models of the individually powered quadrupole (IPQ) superconducting circuits of the LHC (Large Hadron Collider) using the STEAM (Simulation of Transient Effect in Accelerator Magnets) framework. As introduced in chapter 3, to simulate the complex events that occur after a quench, models specialized in different physical domains are required. For this reason, to accomplish such challenging task, the STEAM framework was developed in the Machine Protection and Electrical Integrity Group (MPE) at CERN. STEAM contains a suite of in-house developed programs used to simulate transients in superconducting circuit. The main programs used during this thesis were: STEAM-LEDET (used to simulate the electro-thermal magnet model), Pspice$^{©}$ (commercial software, not part of STEAM, used to simulate the electrical circuit model), and STEAM-COSIM (used to combine electro-thermal and electric models). The reason to generate and validate these models is driven by the necessity to realize an efficient and reliable multi-physics library of all the LHC superconducting circuits to simulate transients during normal operation of the machine, failure cases, and unexpected events.

The function of the IPQ circuits is the matching section in the LHC accelerator, to do that, a non-symmetric magnet layout to compensate the shift of the collision point, is required.

The LHC matching sections are built with individually powered superconducting Nb-Ti quadrupoles of the types MQM and MQY. A few circuits are cooled to a temperature of 1.9 K, and other to 4.5 K. No additional correctors are required when these types of magnets are used, but the number of the magnets and their parameters are specific for each insertion. The protection of these magnets is guaranteed by quench heaters.

In order to realize a more flexible model, adaptable to different current and design conditions, it is possible to spread it in two different models to analyze separately: the electrical circuit model and the electro-thermal magnet model.

The electrical circuit model includes electrical components and it is simulated using PSpice$^{©}$, as explained in chapter 4. In this model, the magnets are represented as inductances and the events that occur during a quench are not take into account. For this reason, once all the electrical IPQ circuits models have been generated, it

is necessary to validate them using the Slow Power Abort (SPA) tests realized during the Hardware Commissioning (HWC). The HWC tests consist of carrying out several powering cycles at different current levels for each superconducting circuit.

The main components on the electrical circuits are the power converters, the diodes, the inductances, and the warm resistances. The warm resistances are different in each IPQ circuit. For this reason, a Python notebook was realized from the STEAM team to calculate them automatically, using the circuit signals recorded during the normal operation. The agreement between simulations and measurements is good, with an average of relative error less then 5%.

As reported in chapter 5 to simulate the electro-thermal behaviour of the magnets, the tool STEAM-LEDET was used. As explained in chapter 2, the IPQ circuits are composed of two main types of magnets: MQM and MQY. After the generation of the magnet models, their validation was performed comparing the simulation results to measurements of fast transient (Fast Power Abort) performed at CERN during the HWC powering tests.

To realize a more accurate electro-thermal model, a new feature of this tool was characterized during this thesis. This feature permits to represent the quench propagation phenomena more realistically, adding a 1D resistance of each turn in the longitudinal direction, upgrading the model from 2D to 2D+1D.

For the validation of the MQY magnet model, dedicated tests performed in the CERN test facility were used. This test campaign was performed with the aim of better understanding the effect of different quench protection systems, and their parameters, on a full-scale magnet. Three protection systems were used: (i) Coupling-Loss Induced Quench (CLIQ), (ii) Quench Heater (QH), and (iii) Energy Extraction (EE).

During the validation process, the measured current during the discharge and the experimental coil resistance, calculated using the measured current and coil voltage, were compared to simulated signals. Comparison between simulations and measurements shows good agreement. At 1.9 K, the average relative error is between 0.5 and 5%. While at 4.5 K the agreement between simulations and measurements gives an average relative error around 10% for the majority of the cases. The electro-thermal model at 4.5 K will be better investigated in the future, in particular, to improve the helium heat capacity.

Once both models (the electrical circuit model and electro-thermal magnet model) are successfully validated,co-simulations were performed with the STEAM-COSIM program, as described in chapter 6. The STEAM-COSIM software combines both models in a cooperative-simulation exchanging information between the models. The importance of the co-simulation is given for particular cases, as two different currents in the magnet apertures or two different types of magnets in series, that cannot be simulated using the STEAM-LEDET tool in a stand-alone configuration. The co-simulation runs in different time-windows and they are characterized by different time stepping. For each time window, iterations are repeated until the convergence level, in terms of the set relative and absolute error, is achieved.

The measurements used to validate the co-simulation come from training quenches performed before 2014 (in case of two different currents in the magnet apertures) and from HWC powering tests (in case of test with the same current in both apertures of the magnet). During the validation process, the measured currents and the measured

coil voltages were compared to simulated signals. Comparison between simulations and measurements shows good agreement. During the validation other interesting plots generated by the tool STEAM-LEDET, were analyzed to better understand the complex behavior of the magnet transient, as the temperature in the magnets turns, the distribution of the coupling currents,and the voltage to ground.

During this thesis work, most of the models were generated using the SWAN notebook (Service for Web based ANalysis). The advantages of the notebook are the possibility of generating models with different magnets/circuit in a semi-automatic mode, and composing a repository of data, queried to provide relevant information with eventually rapidly update of the models,hence saving time. Furthermore, the use of notebooks reduces the probability of mistakes thanks to the visualization of the parameters in the plots.

The main goal during this thesis is the generation and validation of the 78 superconducting IPQ circuits of the LHC. This was achieved developing and updating the notebooks to automatize the generation of the superconducting electrical circuit models and the superconducting magnet models. The approach shown within this thesis for the automatic model generation and validation can be extended to the superconducting circuits of any accelerator.

A Appendix: IPQ parameters

TABLE A.1: Main parameters of the branches of the IPQ circuits I.

Circuit	PC	Magnet	R_Warm_1R	R_Warm_2R	R_Warm_3	L_Ap1Mag1	L_Ap2Mag1	M_Ap12Mag1	L_Ap1Mag2	L_Ap2Mag2	M_Ap12Mag2
RQ4.L1	RPHH	MQY	0.000466	0.000435	0.000385	0.067419	0.067419	0.001799	-	-	-
RQ4.L2	RPHH	2xMQY	0.000410	0.000423	0.000406	0.067419	0.067419	0.001799	0.067419	0.067419	0.001799
RQ4.L5	RPHH	MQY	0.000359	0.000454	0.000386	0.067419	0.067419	0.001799	-	-	-
RQ4.L6	RPHH	MQY	0.000373	0.000371	0.000355	0.067413	0.067419	0.001799	-	-	-
RQ4.L8	RPHH	2xMQY	0.000343	0.000339	0.000319	0.067419	0.067419	0.001799	0.067419	0.067419	0.001799
RQ4.R1	RPHH	MQY	0.000208	0.000207	0.000206	0.067419	0.067419	0.001799	-	-	-
RQ4.R2	RPHH	2xMQY	0.000300	0.000288	0.000271	0.067419	0.067419	0.001799	0.067419	0.067419	0.001799
RQ4.R5	RPHH	MQY	0.000185	0.000228	0.000198	0.067419	0.067419	0.001799	-	-	-
RQ4.R6	RPHH	MQY	0.000362	0.000383	0.000350	0.067419	0.067419	0.001799	-	-	-
RQ4.R8	RPHH	2xMQY	0.000505	0.000496	0.000484	0.067419	0.067419	0.001799	0.067419	0.067419	0.001799
RQ5.L1	RPHGB	MQML	0.000333	0.000219	0.000185	0.021063	0.021063	0.000125	-	-	-
RQ5.L2	RPHH	2xMQY	0.000367	0.000315	0.000294	0.067419	0.067419	0.001799	0.067419	0.067419	0.001799
RQ5.L4	RPHH	MQY	0.000341	0.000330	0.000326	0.067419	0.067419	0.001799	-	-	-
RQ5.L5	RPHGB	MQML	0.000292	0.000270	0.000303	0.021063	0.021063	0.000125	-	-	-
RQ5.L6	RPHH	MQY	0.000395	0.000397	0.000386	0.067419	0.067419	0.001799	-	-	-
RQ5.L8	RPHGB	2XMQM	0.000370	0.000385	0.000372	0.014919	0.014919	0.000088	0.014919	0.014919	0.000088
RQ5.R1	RPHGB	MQML	0.000307	0.000359	0.000284	0.021063	0.021063	0.000125	-	-	-
RQ5.R2	RPHGB	2XMQM	0.000367	0.000315	0.000294	0.014919	0.014919	0.000088	0.014919	0.014919	0.000088
RQ5.R4	RPHH	MQY	0.000322	0.000360	0.000324	0.067419	0.067419	0.001799	-	-	-
RQ5.R5	RPHGB	MQML	0.000286	0.000364	0.000295	0.021063	0.021063	0.000125	-	-	-
RQ5.R6	RPHH	MQY	0.000374	0.000430	0.000431	0.067419	0.067419	0.001799	-	-	-
RQ5.R8	RPHH	2XMQY	0.000370	0.000385	0.000372	0.067419	0.067419	0.001799	0.067419	0.067419	0.001799
RQ6.L1	RPHGB	MQML	0.000227	0.000224	0.000204	0.021063	0.021063	0.000125	-	-	-
RQ6.L2	RPHGB	MQM+MQML	0.000380	0.000331	0.000313	0.014919	0.014919	0.000088	0.021063	0.021063	0.000125
RQ6.L4	RPHGB	MQY	0.000379	0.000409	0.000409	0.021063	0.021063	0.000125	-	-	-
RQ6.L5	RPHGB	MQML	0.000234	0.000214	0.000213	0.021063	0.021063	0.000125	-	-	-
RQ6.L8	RPHGB	MQM+MQML	0.000351	0.000348	0.000335	0.014919	0.014919	0.000088	0.021063	0.021063	0.000125
RQ6.R1	RPHGB	MQML	0.000311	0.000234	0.000217	0.021063	0.021063	0.000125	-	-	-
RQ6.R2	RPHGB	MQM+MQML	0.000364	0.000288	0.000272	0.014919	0.014919	0.000088	0.021063	0.021063	0.000125
RQ6.R4	RPHGB	MQY	0.000380	0.000392	0.000372	0.021063	0.021063	0.000125	-	-	-
RQ6.R5	RPHGB	MQML	0.000322	0.000237	0.000206	0.021063	0.021063	0.000125	-	-	-
RQ6.R8	RPHGB	MQM+MQML	0.000440	0.000422	0.000400	0.014919	0.014919	0.000088	0.021063	0.021063	0.000125

TABLE A.2: Main parameters of the branches of the IPQ circuits II.

Circuit	PC	Magnet	R_Warm_1R	R_Warm_2R	R_Warm_3L	L_Ap1Mag1	L_Ap2Mag1	M_Ap12Mag1	L_Ap1Mag2	L_Ap2Mag2	M_Ap12Mag2
RQ7.L1	RPHGA	2XMQM	0.000281	0.000259	0.000242	0.014919	0.014919	0.000088	0.014919	0.014919	0.000088
RQ7.L2	RPHGA	2XMQM	0.000287	0.000320	0.000264	0.014919	0.014919	0.000088	0.014919	0.014919	0.000088
RQ7.L4	RPHGA	MQM	0.000258	0.000218	0.000212	0.014919	0.014919	0.000088	-	-	-
RQ7.L5	RPHGA	2XMQM	0.000280	0.000256	0.000238	0.014919	0.014919	0.000088	0.014919	0.014919	0.000088
RQ7.L8	RPHGA	2XMQM	0.000241	0.000278	0.000244	0.014919	0.014919	0.000088	0.014919	0.014919	0.000088
RQ7.R1	RPHGA	2XMQM	0.000287	0.000252	0.000245	0.014919	0.014919	0.000088	0.014919	0.014919	0.000088
RQ7.R2	RPHGA	2xMQM	0.000230	0.000274	0.000243	0.014919	0.014919	0.000088	0.014919	0.014919	0.000088
RQ7.R4	RPHGA	MQM	0.000235	0.000237	0.000196	0.014919	0.014919	0.000088	-	-	-
RQ7.R5	RPHGA	2XMQM	0.000270	0.000275	0.000270	0.014919	0.014919	0.000088	0.014919	0.014919	0.000088
RQ7.R8	RPHGA	2XMQM	0.000236	0.000277	0.000235	0.014919	0.014919	0.000088	0.014919	0.014919	0.000088
RQ8.L1	RPHGA	MQML	0.000239	0.000256	0.000237	0.021063	0.021063	0.000125	-	-	-
RQ8.L2	RPHGA	MQML	0.000361	0.000306	0.000298	0.021063	0.021063	0.000125	-	-	-
RQ8.L4	RPHGA	MQML	0.000234	0.000281	0.000277	0.021063	0.021063	0.000125	-	-	-
RQ8.L5	RPHGA	MQML	0.000246	0.000246	0.000225	0.021063	0.021063	0.000125	-	-	-
RQ8.L6	RPHGA	MQML	0.000499	0.000586	0.000596	0.021063	0.021063	0.000125	-	-	-
RQ8.L8	RPHGA	MQML	0.000327	0.000293	0.000284	0.021063	0.021063	0.000125	-	-	-
RQ8.R1	RPHGA	MQML	0.000246	0.000244	0.000234	0.021063	0.021063	0.000125	-	-	-
RQ8.R2	RPHGA	MQML	0.000305	0.000263	0.000262	0.021063	0.021063	0.000125	-	-	-
RQ8.R4	RPHGA	MQML	0.000303	0.000229	0.000220	0.021063	0.021063	0.000125	-	-	-
RQ8.R5	RPHGA	MQML	0.000218	0.000247	0.000240	0.021063	0.021063	0.000125	-	-	-
RQ8.R6	RPHGA	MQML	0.000330	0.000350	0.000338	0.021063	0.021063	0.000125	-	-	-
RQ8.R8	RPHGA	MQML	0.000314	0.000265	0.000262	0.021063	0.021063	0.000125	-	-	-

TABLE A.3: Main parameters of the branches of the IPQ circuits III.

Circuit	PC	Magnet	R_Warm_1R	R_Warm_2R	R_Warm_3L	L_Ap1Mag1	L_Ap2Mag1	M_Ap12Mag1	L_Ap1Mag2	L_Ap2Mag2	M_Ap12Mag2
RQ9.L1	RPHGA	MQM+MQMC	0.000224	0.000204	0.000170	0.014919	0.014919	0.000088	0.010531	0.010531	0.000062
RQ9.L2	RPHGA	MQM+MQMC	0.000354	0.000416	0.000362	0.014919	0.014919	0.000088	0.010531	0.010531	0.000062
RQ9.L4	RPHGA	MQM+MQMC	0.000306	0.000281	0.000279	0.014919	0.014919	0.000088	0.010531	0.010531	0.000062
RQ9.L5	RPHGA	MQM+MQMC	0.000223	0.000206	0.000159	0.014919	0.014919	0.000088	0.010531	0.010531	0.000062
RQ9.L6	RPHGA	MQM+MQMC	0.000502	0.000620	0.000640	0.014919	0.014919	0.000088	0.010531	0.010531	0.000062
RQ9.L8	RPHGA	MQM+MQMC	0.000340	0.000326	0.000315	0.014919	0.014919	0.000088	0.010531	0.010531	0.000062
RQ9.R1	RPHGA	MQM+MQMC	0.000214	0.000196	0.000189	0.014919	0.014919	0.000088	0.010531	0.010531	0.000062
RQ9.R2	RPHGA	MQM+MQMC	0.000308	0.000340	0.000294	0.014919	0.014919	0.000088	0.010531	0.010531	0.000062
RQ9.R4	RPHGA	MQM+MQMC	0.000284	0.000344	0.000303	0.014919	0.014919	0.000088	0.010531	0.010531	0.000062
RQ9.R5	RPHGA	MQM+MQMC	0.000203	0.000206	0.000199	0.014919	0.014919	0.000088	0.010531	0.010531	0.000062
RQ9.R6	RPHGA	MQM+MQMC	0.000363	0.000393	0.000391	0.014919	0.014919	0.000088	0.010531	0.010531	0.000062
RQ9.R8	RPHGA	MQM+MQMC	0.000331	0.000328	0.000273	0.014919	0.014919	0.000088	0.010531	0.010531	0.000062
RQ10.L1	RPHGA	MQML	0.000207	0.000183	0.000171	0.021063	0.021063	0.000125	-	-	-
RQ10.L2	RPHGA	MQML	0.000437	0.000399	0.000383	0.021063	0.021063	0.000125	-	-	-
RQ10.L4	RPHGA	MQML	0.000336	0.000325	0.000319	0.021063	0.021063	0.000125	-	-	-
RQ10.L5	RPHGA	MQML	0.000214	0.000167	0.000148	0.021063	0.021063	0.000125	-	-	-
RQ10.L6	RPHGA	MQML	0.000583	0.000651	0.000665	0.021063	0.021063	0.000125	-	-	-
RQ10.L8	RPHGA	MQML	0.000356	0.000362	0.000354	0.021063	0.021063	0.000125	-	-	-
RQ10.R1	RPHGA	MQML	0.000191	0.000187	0.000174	0.021063	0.021063	0.000125	-	-	-
RQ10.R2	RPHGA	MQML	0.000372	0.000341	0.000333	0.021063	0.021063	0.000125	-	-	-
RQ10.R4	RPHGA	MQML	0.000365	0.000323	0.000327	0.021063	0.021063	0.000125	-	-	-
RQ10.R5	RPHGA	MQML	0.000204	0.000174	0.000163	0.021063	0.021063	0.000125	-	-	-
RQ10.R6	RPHGA	MQML	0.000431	0.000390	0.000378	0.021063	0.021063	0.000125	-	-	-
RQ10.R8	RPHGA	MQML	0.000394	0.0003409	0.000328	0.021063	0.021063	0.000125	-	-	-

B Appendix: STEAM-COSIM port files

This appendix shown the port files for an IPQ circuit composed of two magnet in series. The ports for the two models (electrical and electro-thermal) are different in name and number. The number of the ports related with the electrical circuit (Appendix B.0.1) depends from the number of magnet apertures in the circuit (inductances), while the number of the ports related with the elector-thermal model (Appendix B.0.2 and B.0.3) depends on the number of coil sections of the magnet.

B.0.1 PSpice Port Definition

"name": "Port_1",
"components": "L_1",
"inputs":"couplingParameter": R, "labels": ["R_field_1_stim"],"types": [TH],
"couplingParameter": U,"labels":["V_field_1_stim"],"types":[EM],
"outputs":"couplingParameter": I, "labels": ["I(x_mag.L_1)"],"types": [TH, EM]

"name": "Port_1_1",
"components": "L_1",
"inputs":"couplingParameter": U, "labels": ["V_circuit_1_stim"],"types": [EM],
"outputs":"couplingParameter": U, "labels": ["V(x_mag.1_v_l_diff)"],"types": [EM]

"name": "Port_2",
"components": "L_2",
"inputs":"couplingParameter": R, "labels": ["R_field_2_stim"],"types": [TH],
"couplingParameter": U, "labels": ["V_field_2_stim"],"types": [EM],
"outputs":"couplingParameter": I, "labels": ["I(x_mag.L_2)"],"types": [TH, EM]

"name": "Port_2_1",
"components":"L_2",

"inputs":"couplingParameter": U, "labels": ["V_circuit_2_stim"],"types": [EM],
"outputs":"couplingParameter": U, "labels": ["V(x_mag.2_v_l_diff)"],"types": [EM]

"name": "Port_3",
"components": "L_3",
"inputs":"couplingParameter": R, "labels": ["R_field_3_stim"],"types": [TH],
"couplingParameter": U, "labels": ["V_field_3_stim"],"types": [EM],
"outputs":"couplingParameter": I, "labels": ["I(x_mag.L_3)"],"types": [TH, EM]

"name": "Port_3_1",
"components": ["L_3"],
"inputs":"couplingParameter": U, "labels": ["V_circuit_3_stim"],"types": [EM],
"outputs":"couplingParameter": U, "labels": ["V(x_mag.3_v_l_diff)"],"types": [EM]

"name": "Port_4",
"components": ["L_4"],
"inputs":"couplingParameter": R, "labels": ["R_field_4_stim"],"types": [TH],
"couplingParameter": U, "labels": ["V_field_4_stim"],"types": [EM],
"outputs":"couplingParameter": I, "labels": ["I(x_mag.L_4)"],"types": [TH, EM]

"name": "Port_4_1",
"components": ["L_4"],
"inputs":"couplingParameter": U, "labels": ["V_circuit_4_stim"],"types": [EM],
"outputs":"couplingParameter": U, "labels": ["V(x_mag.4_v_l_diff)"],"types": [EM]

B.0.2 LEDET1 Port Definition

"name": "Port_1",
"components": ["CoilSections_1"],
"inputs":"couplingParameter":I,"labels": ["I_CoilSections_1"],"types":[TH, EM],
"outputs":"couplingParameter":R, labels":["R_CoilSections_1"],"types":[TH],
"couplingParameter":U,"labels":["U_inductive_dynamic_CoilSections_1"],"types":[TH]

"name":"Port_2",
"components":"CoilSections_2",
"inputs":"couplingParameter":I,"labels":["I_CoilSections_2"],"types":[TH, EM],
"outputs":"couplingParameter":R,"labels":["R_CoilSections_2"],"types":[TH],
"couplingParameter":U,"labels":["U_inductive_dynamic_CoilSections_2"],"types":[TH]

B.0.3 LEDET2 Port Definition

"name": "Port_3",
"components":["CoilSections_1"],
"inputs":"couplingParameter":I,"labels":["I_CoilSections_1"],"types":[TH, EM],
"outputs":"couplingParameter":R,"labels":["R_CoilSections_1"],"types":[TH],
"couplingParameter":U,"labels":["U_inductive_dynamic_CoilSections_1"],"types":[TH]

"name": "Port_4",
"components":["CoilSections_2"],
"inputs":"couplingParameter":I,"labels":["I_CoilSections_2"],"types":[TH, EM],
"outputs":"couplingParameter":R,"labels":["R_CoilSections_2"],"types":[TH],
"couplingParameter":U,"labels":["U_inductive_dynamic_CoilSections_2"],"types":[TH]

C Appendix: STEAM-COSIM Configuration file

In appendix is shown the configuration file for the circuit RQ9.L1. It reports the paths of the models (electrical and electro-thermal). In the configuration file is defined the time-windows (between t_0 and t_{end}), the time-stepping, and the relative and absolute tolerance to achieved in the simulation. The time-stepping was chosen taking into account the events occurring in the respective time windows.

```
    "coSimulationDir": "C:/COSIM/IPQ/Output/Tes/",
"coSimulationModelSolvers": [ "PSPICE", "LEDET", "LEDET" ],
"coSimulationModelDirs": [ "C:/COSIM/IPQ/Input/cosim_model_RQ9_L1/PSpice/",
"C:/COSIM/IPQ/Input/cosim_model_RQ9_L1/LEDET1/",
"C:/COSIM/IPQ/Input/cosim_model_RQ9_L1/LEDET2/" ],
"coSimulationModelConfigs": [ "PSpiceConfig.json",
"LedetConfig.json",
"LedetConfig.json" ],
"coSimulationPortDefinitions": [ "PSpiceInputOutputPortDefinition.json",
"LedetInputOutputPortDefinition.json",
"LedetInputOutputPortDefinition.json" ],
"convergenceVariables":  [ "I(x_mag.L_1)", "U_inductive_dynamic_CoilSections_1",
"U_inductive_dynamic_CoilSections_1" ],
"t_0": [ 0,0.08,0.04,0.1 ],
"t_end": [ 0.08,0.04,0.1,0.35 ],
"t_step_max": [ [ 5e-5,1e-6,5e-5,1e-4 ], [5e-5,1e-6,5e-5,1e-4], [5e-5,1e-6,5e-5,1e-4]],
"relTolerance": [ 0.0001, null, null],
"absTolerance": [ 1, null, null ],
"executionOrder": [ 1, 2, 3 ],
"executeCleanRun": [ true, true, true ]
```

Bibliography

[1] *Simulation of Transient Effects in Accelerator Magnets*. URL: `https://espace.cern.ch/steam/_layouts/15/start.aspx#/SitePages/Home.aspx`.

[2] URL: `http://home.cern`.

[3] URL: `https://home.cern/science/accelerators/accelerator-complex`.

[4] H.K. Onnes. *Private Notes*. Phys.Lab.Univ.Leiden, 1911.

[5] W. Meissner and R. Ochsenfeld. *Ein neuer Effekt bei Eintritt der Supraleitfähigkeit.* Naturwissenschaften, 1933.

[6] Fritz London and Heinz London. "The electromagnetic equations of the supraconductor". In: *Proceedings of the Royal Society of London. Series A-Mathematical and Physical Sciences* 149.866 (1935), pp. 71–88.

[7] Heike Kamerlingh Onnes. *Through measurement to knowledge: The selected papers of Heike Kamerlingh Onnes 1853–1926*. Vol. 124. Springer Science & Business Media, 2012.

[8] L. N. Bardeen J. Cooper and J. R. Schrieffer. *Theory of Superconductivity.* 1957.

[9] J. G. Bednorz and K. A. Müller. *Possible high Tc superconductivity in the BaLaCuO system.* Zeitschrift für Physik B Condensed Matter, June 1986.

[10] M. K. Wu and et al. *Superconductivity at 93 K in a New Mixed Phase YBaCuO Compound System at Ambient Pressure.* 1987.

[11] SL Bud'Ko et al. "Boron isotope effect in superconducting MgB 2". In: *Physical Review Letters* 86.9 (2001), p. 1877.

[12] *The London equations*. URL: `https://en.wikipedia.org/wiki/Meissner_effect`.

[13] M. Breschi. *Study material*. 2016.

[14] M. Haleeda N. Awang Kechik and R. Abd-Shukor. "PJSRR (2016) 2(1): Effect of Yb2O3 Nanoparticle Addition on Superconducting Properties of BSCCO (2223)/Ag Tapes by Acetate Precipitation Method". In: *Pertanika Journal of Science and Technology* 2 (Jan. 2016).

[15] Emmanuele Ravaioli. *CLIQ. A new quench protection technology for superconducting magnets*. CERN-THESIS-2015-091. Twente U., Enschede, 2015.

[16] Martin N Wilson. "Superconducting magnets". In: (1983).

[17] David Larbalestier et al. "High-Tc superconducting materials for electric power applications". In: *Materials For Sustainable Energy: A Collection of Peer-Reviewed Research and Review Articles from Nature Publishing Group*. World Scientific, 2011, pp. 311–320.

[18] TEVATRON SSC. "Superconductivity and the LHC: The early days". In: *CERN Courier* (2011).

[19] Arjan P Verweij. "Electrodynamics of superconducting cables in accelerator magnets." In: (1997).

[20] Luca Bottura. *Cable Stability*. CERN Yellow Report CERN-2014-005, pp.401-451, 2014.

[21] L Coull et al. "LHC magnet quench protection system". In: *IEEE transactions on magnetics* 30.4 (1994), pp. 1742–1745.

[22] F Rodriguez-Mateos and F Sonnemann. "Quench heater studies for the LHC magnets". In: *PACS2001. Proceedings of the 2001 Particle Accelerator Conference (Cat. No. 01CH37268)*. Vol. 5. IEEE. 2001, pp. 3451–3453.

[23] C Scheuerlein, L Grand-Clement, and B Katzer. *HL-LHC quench heater quality control 11 T dipole prototype quench heater characterisation*. 2019.

[24] E. Todesco. "Quench limits in the next generation of magnets". In: *CERN Yellow Report* pp.10-16 (2013).

[25] Emanuele Ravaioli et al. "New, coupling loss induced, quench protection system for superconducting accelerator magnets". In: *IEEE transactions on applied superconductivity* 24.3 (2013), pp. 1–5.

[26] O. Brüning et al. "LHC Design Report, volume I, The LHC main ring". In: *CERN, Geneva* (2004).

[27] L Rossi. "The LHC superconducting magnets". In: *Proceedings of the 2003 Particle Accelerator Conference*. Vol. 1. IEEE. 2003, pp. 141–145.

[28] Lyndon Evans and Philip Bryant. *LHC Machine*. PUBLISHED BY INSTITUTE OF PHYSICS PUBLISHING and SISSA, 2014.

[29] Vittorio Parma, H Prin, and F Lutton. "Short straight sections in the LHC matching sections (MS SSS): An extension of the arc cryostats to fulfill specific machine functionalities". In: *Proceedings of the 2005 Particle Accelerator Conference*. IEEE. 2005, pp. 1724–1726.

[30] *EDMS5 site*. URL: https://edms5.cern.ch/cdd/plsql/c4w_guided.equipment_hierarchy?cookie=2243400&p_cat_id=M.

[31] M Zerlauth et al. "The electrical circuit description for the LHC". In: *Proceedings of the EPAC*. 2002.

[32] Vincent Barbet. *LHC 4-6-8kA 08V, LHC Power Convertr Guide*. Tech. rep. CERN. URL: http://te-epc-lpc.web.cern.ch/te-epc-lpc/converters/lhc4-6-8ka-08v/general.stm#machine_installation.

[33] E Ravaioli et al. "Lumped-element dynamic electro-thermal model of a superconducting magnet". In: *Cryogenics* 80 (2016), pp. 346–356.

[34] L. Ravaioli E. Brouwer. *SMIC Documentation*. 2018. URL: `https://gitlab.cern.ch/steam/steam-smic`.

[35] Stephan Russenschuck. *Roxie: the routine for the optimization of magnet x-sections, inverse field computation and coil end design*. Tech. rep. CERN, 1993.

[36] *CERN Layout Circuit*. URL: `hhttps://layout.web.cern.ch/default.aspx?file=navigators.aspx&topid=186394&version=STUDY&navigator=electrical`.

[37] M. Janitschke and F. Murgia. *Automatic calculation of R_{WARM} for a class of LHC circuits*. 2020 Apr 02. URL: `https://indico.cern.ch/event/904043/`.

[38] M. Maciejewski. *SignalMonitoringProject (EDMS note number: 2374710)*. 2020. URL: `https://edms.cern.ch/document/2374710/1`.

[39] D. Piparo et al. "SWAN: A service for interactive analysis in the cloud". In: *Future Generation Computer Systems* 78 (2018), pp. 1071–1078.

[40] *GitLab steam-sing*. URL: `https://gitlab.cern.ch/steam/steam-sing`.

[41] *GitLab steam-notebooks, $sing_I PQ$ and $sing_c osim_I PQ$*. URL: `https://gitlab.cern.ch/steam/steam-notebooks/-/tree/master/steam-sing-input/IPQ`.

[42] *GitLab steam-notebooks*. URL: `https://gitlab.cern.ch/steam/steam-notebooks/-/tags/1.0.0`.

[43] *GitLab steam-pspice-library*. URL: `https://gitlab.cern.ch/steam/steam-pspice-library/-/tree/master/power_supply/Items/IPQ_power_converters.lib`.

[44] URL: `https://universe-review.ca/F13-atom06.htm`.

[45] Giulio Manfreda et al. "Review of ROXIE's material properties database for quench simulation." In: *TE Technology department internal note* 35 (2011).

[46] Dimitri Pracht. *Multiphysics modelling of the LHC main quadrupole superconducting circuit*. CERN-THESIS-2019-071. Hannover U., 2019.

[47] *NIST WEBBOOK*. URL: `https://webbook.nist.gov/chemistry/`.

[48] H Ten Kate, H Boschman, and L Van De Klundert. "Longitudinal propagation velocity of the normal zone in superconducting wires". In: *IEEE transactions on magnetics* 23.2 (1987), pp. 1557–1560.

[49] Herman ten Kate. *Superconducting Magnets Quench Propagation and Protection*. URL: `https://indico.cern.ch/event/194284/contributions/1472819/attachments/281522/393603/TenKate_-_CAS_-Handout-Quench-Erice-2103.pdf`.

[50] *GitLab steam-ledet-input, MQM and MQY*. URL: `https://gitlab.cern.ch/steam/steam-notebooks/-/tree/master/steam-ledet-input`.

[51] Michal Maciejewski. "Co-simulation of transient effects in superconducting accelerator magnets". PhD thesis. CERN, 2019. URL: https://cds.cern.ch/record/2675039.

[52] STEAM team. *STEAM Co-sim user manual (EDMS note number: 2047054)*. 2018.

[53] *GitLab steam-pspice-library*. URL: https://gitlab.cern.ch/steam/steam-pspice-library/-/blob/master/magnet/Items/magnets_cosimulation.lib.

[54] Boris Bellesia et al. "Optimisation of the Powering Tests of the LHC Superconducting Circuits". In: (2010).

[55] Christoph Obermair. *Signal monitoring for the LHC-Development of an application for analyzing the main quadrupole busbar resistance*. Tech. rep. 2018.

[56] *245NQ015PbF datasheets*. URL: https://www.vishay.com/docs/94464/vs-245nq015pbf.pdf.

[57] *D4457N datasheets*. URL: https://www.alldatasheet.net/datasheet-pdf/pdf/416726/INFINEON/D4457N.html.

[58] *Test Procedure for the Individually Powered 4-6 kA Quadrupole-Circuits in the LHC Insertions (EDMS note number: 874884)*. 2016.

[59] E. Ravaioli et al. "First implementation of the CLIQ quench protection system on a full-scale Accelerator quadrupole magnet". In: *IEEE Transactions on Applied Superconductivity* 26.3 (2016), pp. 1–5.

[60] Marta Bajko et al. "Upgrade of the CERN Superconducting Magnet Test Facility". In: *IEEE Transactions on Applied Superconductivity* 27.4 (2016), pp. 1–7.

[61] Scheuerlein Christian. *HL-LHC quench heaters*. 2019. URL: https://indico.cern.ch/event/798403/contributions/3317813/attachments/1794597/2925603/HL-LHC_quench-heater-12Feb2019.pdf.

[62] M. Mentink. *Development of the STEAM Comsol Magnet Simulation Tool (EDMS note number: 2054126)*. 2018.

[63] M. Janitschke. *SWAN notebook to run an automatic LEDET parametric sweep*. 2020. URL: https://indico.cern.ch/event/913508/contributions/3841536/.